Origin of a classical space in quantum inhomogeneous models

A. A. Kirillov[a)]
Institute for Applied Mathematics and Cybernetics, 603005 Nizhny Novgorod, Russia

G. Montani
ICRA Dipartimento di Fisica Universitá di Roma, I–00185 Roma, Italy

(Submitted 28 August 1997)
Pis'ma Zh. Éksp. Teor. Fiz. **66**, No. 7, 449–453 (10 October 1997)

The origin of a classical background geometry in the quantum vacuum inhomogeneous master model is investigated. It is shown that the background appears at the moment when the horizon size has the order of the characteristic scale of the inhomogeneity of the universe and that the local anisotropy can be described by small perturbations. © *1997 American Institute of Physics.* [S0021-3640(97)00119-9]

PACS numbers: 98.80.Cq, 04.60.−m, 02.40.−k

It is widely recognized that the most realistic models of the early universe have to contain an inflationary epoch.[1,2] Such an epoch is known to have energy scales $H=\dot{a}/a\sim 10^{-5}m_{pl}$ much below the Planck energy, and at these scales the space–time is believed to have a classical nature. In particular, this is the main basis for the semiclassical description of the early universe (e.g., see Ref. 3 and references therein). However, the quantum boundary (the moment of origin of a stable classical background geometry) is not so well defined as is commonly believed now. In general the moment when the space–time acquires a semiclassical nature has to depend on the initial conditions and is a free parameter in quantum cosmology.

We note that the problem of the origin of a classical background does not coincide with the problem of the quasi-classical limit in quantum gravity and cosmology. Indeed, quantum nonlinear inhomogeneous gravitational fields near the singularity has been shown to be described by stationary states[4] (see also the multidimensional case in Ref. 5). Therefore, there is no difficulty in constructing high-frequency wave packets and considering the quasi-classical limit, regardless of how close to the singularity the universe is. However, the background geometry was shown to be absent near the singularity (it turns out to be hidden under pure quantum fluctuations[4]). In fact the moment of origin of a background depends upon the particular choice of an initial quantum state and therefore appears as a free parameter. In the present paper we study the origin of a classical background in vacuum long-wavelength asymptotic models[6] $L_i \gg L_h$, where L_i and L_h are, respectively, the characteristic scale of the inhomogeneity of the gravitational field and the horizon size (we note that in quantum gravity the horizon size and the scale of inhomogeneity should be understood to mean the corresponding mean values) and show that the stable background appears at the moment when the horizon size reaches the scale of the inhomogeneity $L_i\sim L_h$. Such an estimate remains also valid in the quasi-classical limit. In chaotic inflationary scenarios[2,7] this means that the inflationary epoch starts when the semiclassical approximation is not valid. We consider the ADM (Arnowitt–Deser–Misner) scheme of quantization,[8] since in this case we avoid the problem of the probabilistic interpretation when considering the matter sources and, besides, this scheme represents the only rigorous way to treat the case when a part of the universe can recollapse.[3]

Near the singularity the behavior of the long-wavelength inhomogeneous gravitational field can be described in the approximation of deep oscillations[4,6] as follows. The metric tensor has the representation in the Kasner-like form

$$ds^2=N^2dt^2-R^2\sum_{a=1}^{3}\exp\{q^a\}(\ell^a_\alpha dx^\alpha+N^a dt)^2, \tag{1}$$

where $\ell^a_\alpha(x)$ are Kasner vectors ($\det \ell^a_\alpha=1$) and we have separated out a slow function of time, R, which characterizes the absolute value of the metric functions[9,10] and is specified by initial conditions (see below). Near the singularity it is convenient to make use of the following parametrization of the scale functions:[6]

$$q^a=Q_a\ln g;\quad \sum Q_a=1\,, \tag{2}$$

where the anisotropy parameters Q_q and $\ln g=\Sigma q^a$ can be expressed in terms of a new set of variables τ, y^i $(i=1,2)$ as follows:

$$Q_a(y)=\frac{1}{3}\left(1+\frac{2y^iA^a_i}{1+y^2}\right),\quad \ln g=-3e^{-\tau}\frac{1+y^2}{1-y^2}, \tag{3}$$

where A^a_i is a constant matrix (see, e.g., Ref. 6). The parametrization (3) has the range $y^2<1$ and $-\infty<\tau<\infty$ $(0\leqslant g\leqslant 1)$, and an appropriate choice of the function R allows one to cover by this parametrization all of the classically allowed region of the configuration space.

The evolution (rotation) of Kasner vectors is completely determined by the momentum constraints,[11] while the evolution of scale functions is described by the action (we use Planckian units $m_{pl}=16\pi$ (see Refs. 4,6) and fix the gauge $N^a=0$)

$$I=\int\left\{\left(\mathbf{P}\frac{\partial\mathbf{y}}{\partial t}+h\frac{\partial\tau}{\partial t}\right)-\frac{N}{6R^3\sqrt{g}}e^{2\tau}\left[\varepsilon^2-h^2+6e^{-2\tau}V(\tau,\mathbf{y})\right]\right\}d^3x\,dt, \tag{4}$$

where $\varepsilon^2=(\frac{1}{4})(1-y^2)^2\mathbf{P}^2$ and the potential term $V=R^6g(-{}^3\mathrm{R})$ (${}^3\mathrm{R}$ is the scalar curvature with the metric (1)) has the following decomposition

$$V=R^4\sum_{A=1}^{k}\lambda_A g^{\sigma_A}, \tag{5}$$

where the coefficients λ_A are functions of all the dynamical variables (and slow functions of $\ln g$) and characterize the initial degree of inhomogeneity of the gravitational field, and $\sigma_{abc}=1+Q_a-Q_b-Q_c$, $b\neq c$. In the approximation of deep oscillations $g\ll 1$ this potential can be modeled by a set of potential walls

$$g^{\sigma_A}\to\theta_\infty[\sigma_A(Q)]=\begin{cases}+\infty, & \sigma_A<0,\\ 0, & \sigma_A>0,\end{cases} \tag{6}$$

and is independent of the Kasner vectors $V_\infty=\Sigma\,\theta_\infty(Q_a)$.

By solving the Hamiltonian constraint $H=0$ in (4) we define the ADM action reduced to the physical sector as follows:

$$I=\int\left(\mathbf{P}_{\mathbf{y}}\cdot\frac{d\mathbf{y}}{d\tau}-H_{\mathrm{ADM}}\right)d^3x\,d\tau, \tag{7}$$

where $H_{\mathrm{ADM}}\equiv -h=\pm\sqrt{\varepsilon^2+6\,e^{-2\tau}V}$ is the ADM energy density and τ plays the role of time ($\dot{\tau}=1$) which corresponds to the gauge $N_{\mathrm{ADM}}=(3R^3\sqrt{g}/H_{\mathrm{ADM}})e^{-2\tau}$. The sign of H_{ADM} depends on the initial conditions and is determined from the requirement that H_{ADM} is a differentiable function of the coordinates (the positive sign of H_{ADM} corresponds to expanding regions of the space).

The condition of applicability of the approximation (6) can be written as follows

$$\varepsilon^2\gg 6e^{-2\tau}V \tag{8}$$

as $Q_a>\delta>0$ ($\delta\ll 1$). Thus, from the condition that the approximation of deep oscillations (6) breaks down at the moment $g\sim 1$, one finds that the function R should be chosen as follows: $R^4=(\varepsilon^2/6\lambda)e^{2\tau}$ (where $\lambda=|\Sigma\lambda_A|$), and the inequality (8) reads $g\ll 1$.

The synchronous cosmological time is related to τ by the equation $dt=N_{\mathrm{ADM}}d\tau$, from which we find the estimate $\sqrt{g}\sim t/t_0$, where $t_0=cL_i\sqrt{\varepsilon L_i}$, $L_i^2\sim 1/\lambda$ is a characteristic scale of the inhomogeneity, ε is the ADM energy density ($\varepsilon=$ const), and c is a slow (logarithmic) function of time ($c\sim 1$ as $g\to 1$). Thus, in the synchronous time the upper limit of the approximation (6) is $t\sim t_0$. We note that from the physical viewpoint t_0 corresponds to the moment when the horizon size reaches the characteristic scale of inhomogeneity, and both terms in the Hamiltonian constraint (the kinetic and potential terms) have the same order.

The physical sector of the configuration space (variables $\mathbf{y}$) is a realization of the Lobachevsky plane and the potential V_∞ limits the part $K=\{Q_a\geqslant 0\}$. Quantization of this system can be carried out as follows. The ADM density of energy represents a constant of motion and, therefore, we can define stationary states as solutions to the eigenvalue problem for the set of Laplace–Beltrami operators $\varepsilon^2(x)=\Delta(x)+(\frac{1}{4})P(x)$ (see Refs. 4 and 5)

$$\left(\Delta+k_n^2+\frac{1}{4}P\right)\varphi_n(y)=0,\qquad \varphi_n|_{\partial K}=0, \tag{9}$$

where the Laplacian operator Δ is constructed via the metric $\delta l^2=h_{ij}\delta y^i\delta y^j=r^2(4(\delta y)^2/(1-y^2)^2)$, r and P are determined through a renormalization procedure (in the discrete approximation one can define $r=(\Delta x)^3$, $P=1/r^2+4k_0^2$, so that in the ground state $\varepsilon_0=0$). The eigenstates φ_n are classified by the integer-valued function $n(x)$ and obey the orthogonality and normalization relations

$$(\varphi_n,\varphi_m)=\int_K \varphi_n^*(y)\varphi_m(y)D\mu(y)=\delta_{nm}, \tag{10}$$

where

$$D\mu(y)=\prod_x \frac{1}{\pi}\sqrt{h}d^2y(x), \quad K=\prod_x K(x),$$

and π is the volume of $K(x)$. Thus, an arbitrary solution Ψ to the Schrödinger equation $i\partial_\tau\Psi=H_{\mathrm{ADM}}\Psi$ takes the form

$$\Psi=\sum_n A_n \exp(-iH_n\tau)\varphi_n(y), \tag{11}$$

where $H_n=\int k_n d^3x$, and the A_n are arbitrary constants $(\Sigma_n|A_n|^2=1)$ which are to be specified by initial conditions. The probability distribution for the variables y has the standard form $P(y,\tau)=|\Psi(y,\tau)|^2$, which coincides with that in Ref. 5, derived on the basis of the Newton–Wigner states. The function $n(x)$ plays the role of filling numbers for frozen nonlinear gravitational waves whose wavelengths exceed the horizon size (the density of excitations for the local anisotropy[4,12]). The eigenstates φ_n define stationary (in terms of the anisotropy parameters $Q(y)$) quantum states and, in the case $H_n>0$, describe an expanding universe with a fixed energy density of the anisotropy.

For an arbitrary quantum state Ψ one can determine the background metric $\langle ds^2\rangle$. However, such a background is stable and has meaning only when the quantum fluctuations around it are small. In the case $g\ll 1$ the fluctuations well exceed the average metric, and the background is hidden.[4] Indeed, in this case for the moments of scale functions one can find the estimate (in the same way as in Ref. 5)

$$\langle a_i^m\rangle=\langle R^m g^{\frac{m}{2}Q_i}\rangle\sim D_i(m,\tau)\exp\left(\frac{m+5}{2}\tau\right), \tag{12}$$

where the function $D_i(m,\tau)$ depends upon the choice of the initial quantum state.

Consider now an arbitrary stationary state φ_n which gives the stationary probability distribution $P(y)=|\varphi_n|^2$. In this case $D=bk_n^{m/2}(L_i^{m/2})_n$ is a constant, where the characteristic scale of inhomogeneity $(L_i^{m/2})_n$ derives from the momentum constraints and b comes from the uncertainty in the operator ordering. Thus for the intensity of quantum fluctuations one obtains the expression $\langle\delta^2\rangle=(\langle a^2\rangle/\langle a\rangle^2-1)\sim e^{-5/2\tau}$, which is divergent in the limit $g\to 0$ $(\tau\to-\infty)$ and explicitly shows the instability of the average geometry for $g\ll 1$. The intensity of quantum fluctuations reaches the order $\delta\sim 1$ at the moment $t\sim(L_i^{3/2})_n\sqrt{k_n}$ $(g\sim 1)$ when the anisotropy functions can be described by small perturbations $a_i^2=R^2(1+Q_i\ln g+\dots)$ and the universe acquires a quasi-isotropic character. This moment can be considered as the moment of origin of a stable classical background.

Consider now the case of quasi-classical states. Classical trajectories of this system have been shown to have a chaotic behavior,[6] which leads to an additional rapid spreading of an arbitrary initial wave packet (e.g., see Ref. 13 and references therein). An arbitrary initial quantum uncertainty increases as $\Delta\Gamma\sim\Delta\Gamma_0 e^S$, where $S=(\tau-\tau_0)$ is the geodesic path, and quickly reaches the maximum value $\Gamma_{\max}\sim 2\pi^2\langle H\rangle$ (where $\Gamma_{\max}$ is the phase volume).[b] Thus the picture in which the center of the wave packet traces a classical trajectory remains valid during the period $\Delta\tau = \ln(\Gamma_{\max}/\Delta\Gamma_0)$. In quantum theory the minimum value $\Delta\Gamma_0 \sim 1$, and hence one finds $\Delta\tau_{\max} \sim \ln \overline{n}$ where $\overline{n}$ is the average density of excitations corresponding to the energy $\langle H\rangle$. After the period $\Delta\tau_{\max}$ the function $D_i(m,\tau)$ in (12) becomes almost constant and we have the situation described earlier.

We point out that the period $\Delta\tau_{\max}$ can be arbitrary large (depending upon a particular choice of initial conditions). This means that in the problem of a cosmological collapse the picture in which the universe is a classical object can be valid up to arbitrarily small times $t \ll t_{pl}$. However, in the cosmological expansion problem the universe spends an infinite period of time τ starting from the singularity, and therefore an arbitrary initial wave packet will spread over the whole configuration space, and the classical picture is invalid.

In conclusion we stress that in the presence of matter the quantum evolution of the inhomogeneous universe requires a separate analysis; however, it is a general fact that the stable background appears at the moment when the local anisotropy can be regarded as perturbations.

This research was supported in part (for A. A. K) by the Russian Fund for Fundamental Research under Grant 95-02-04935 and the Russian research project ''Cosmomicrophysics.''

[a] e-mail: kirillov@focus.nnov.su

[b] When $\Delta\Gamma \sim \Gamma_{\max}$ the exponential behavior is replaced by a power law,[13] but this does not significantly alter all the subsequent estimates.

---

[1] A. A. Starobinsky, Phys. Lett. B **91**, 100 (1980); A. H. Guth, Phys. Rev. D **23**, 347 (1981); A. A. Linde, Phys. Lett. B **108**, 389 (1982).
[2] A. D. Linde, *Particle Physics and Inflationary Cosmology*, Harwood Academic, 1990.
[3] A. O. Barvinsky, Phys. Rep. **230**, 237 (1993); B. L. Al'tshuler and A. O. Barvinsky, Usp. Fiz. Nauk **166**, 459 (1996).
[4] A. A. Kirillov, Phys. Lett. B **399**, 201 (1997); Int. J. Mod. Phys. D **3**, 431 (1994).
[5] A. A. Kirillov, JETP Lett. **62**, 89 (1995); A. A. Kirillov and V. N. Melnikov, Phys. Lett. B **389**, 221 (1996).
[6] A. A. Kirillov, Zh. Éksp. Teor. Fiz. **103**, 721 (1993) [JETP **76**, 355 (1993)]; A. A. Kirillov and V. N. Melnikov, Phys. Rev. D **51**, 723 (1995); A. A. Kirillov and G. Montani, Phys. Rev. D (1997), in press.
[7] A. D. Linde, Phys. Lett. B **129,** 177 (1983); A. A. Starobinsky, in *Current Topics in Field Theory, Quantum Gravity and Strings*, Lecture Notes in Physics, Vol. 246, edited by H. J. de Vega and N. Sanchez, Heidelberg: Springer-Verlag, 1986, p. 107.
[8] R. Arnowitt, S. Deser, and C. W. Misner, in *Gravitation: An Introduction to Current Research*, edited by L. Witten, New York: Wiley, 1962, p. 227.
[9] C. W. Misner, Phys. Rev. Lett. **22**, 1071 (1969).
[10] C. W. Misner, K. S. Thorne and J. A. Wheeler, *Gravitation*, San Francisco: Freeman, 1973, Vol. 2.
[11] V. A. Belinskii, E. M. Lifshitz, and I. M. Khalatnikov, Adv. Phys. **31**, 639 (1982); Zh. Éksp. Teor. Fiz. **62**, 1606 (1972) [Sov. Phys. JETP **35**, 838 (1972)].
[12] C. W. Misner, Phys. Rev. **186**, 1319 (1969); J. A. Wheeler, in *Magic Without Magic*, edited by J. Klander, San Francisco: Freeman, 1972.
[13] P. V. Elyutin, Usp. Fiz. Nauk **155**, 397 (1988) [Sov. Phys. Usp. **31**, 597 (1988)].

Published in English in the original Russian journal. Edited by Steve Torstveit.

Observation of laser satellites in a plasma produced by a femtosecond laser pulse

S. A. Pikuz
P. N. Lebedev Physical Institute Russian Academy of Sciences, 118927 Moscow, Russia; Center for Ultrafast Optical Science, Ann Arbor, Michigan, USA

A. Maksimchuk, D. Umstadter, and M. Nantel
Center for Ultrafast Optical Science, Ann Arbor, Michigan, USA

I. Yu. Skobelev and A. Ya. Faenov
Atomic Spectroscopy Data Center, All-Russia Scientific-Research Institute of Physicotechnical and Radio Electronic Measurements, 141570 Mendeleevo, Moscow Region, Russia

A. Osterheld
Lawrence Livermore National Laboratory, University of California, Livermore, CA 94550, USA

(Submitted 2 September 1997)
Pis'ma Zh. Éksp. Teor. Fiz. **66**, No. 7, 454–459 (10 October 1997)

Laser satellites are detected in the emission spectra of magnesium and aluminum plasmas produced by femtosecond laser pulses. This is made possible by the realization of picosecond time resolution in a high-luminosity x-ray spectrograph with a spherically curved mica crystal. The temporal characteristics of these newly recorded spectral lines show unequivocally that they are formed as a result of nonlinear processes. © *1997 American Institute of Physics.*
[S0021-3640(97)00219-3]

PACS numbers: 52.50.Jm, 52.25.Nr

Strong oscillating electric and magnetic fields can greatly influence the emission characteristics of ions. Vinogradov and Yukov[1] have shown theoretically that new spectral lines, which they called laser satellites, should appear in the emission spectrum of an ion placed in a strong laser field. The laser satellites are due to a nonlinear interaction of the radiation with the excited states B^* of the ions, as a result of which the laser photons $\hbar\omega_{\rm las}$ are converted into photons $\hbar\omega'$ and $\hbar\omega''$ with the frequencies $\omega'=\omega_{B*B}+\omega_{\rm las}$ and $\omega''=\omega_{B*B}-\omega_{\rm las}$, where $\hbar\omega_{B*B}$ is the difference of the energies of the ion in the states B^* and B (see Fig. 1). These nonlinear processes are possible if the states B^* and B of the ion possess the same parity. This means that the transition $B^*\rightarrow B$ itself is optically forbidden.

Thus a laser field with frequency $\omega_{\rm las}$ should produce two new spectral lines around each parity-forbidden transition $B^*\rightarrow B$ of the ion. These lines have frequencies $\omega_{B*B}\pm\omega_{\rm las}$ and virtually the same intensities.[1] It should be noted that if the ion B is multiply charged, then, first, the wavelengths of the emitted laser satellites can lie in the

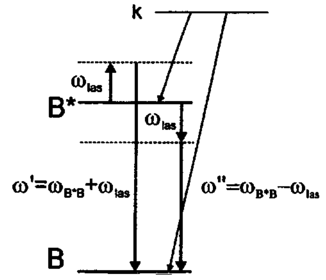

FIG. 1. Scheme of the nonlinear interaction of laser photons with multiply charged ions.

x-ray region of the spectrum and, second, the probabilities of the nonlinear processes become quite high only in ultrahigh laser fields (see below).

Despite the fact that the laser x-ray satellites were predicted more than 20 years ago, they had not been observed until very recently. This is because their experimental detection requires: 1) an intense laser pulse with flux density $\geqslant 10^{16}$ W/cm^2, 2) an x-ray spectrograph with a very good spectral resolution $\lambda/\Delta\lambda \geqslant 5000$, and 3) the capability of recording the emission spectrum of a plasma only during the interaction with the laser pulse. It is very difficult to satisfy these conditions in the same experiment. For example, it is quite easy to achieve high laser radiation flux densities $q > 10^{17}$ W/cm^2 with a subpicosecond pulse, but in this case it is very difficult (even now) to obtain subpicosecond time resolution of the x-ray spectrograph. In the opposite case of a quite long laser pulse, laser satellites can be detected even without time resolution (time resolution can actually be replaced by good spatial resolution, since in this case there is enough time during the laser pulse for the plasma to leave the observation region), but this requires quite unique laser setups. We note that recently we were the first to observe[2,3] laser satellites in the spectra of a titanium plasma by using one such setup — ''Janus'' — at the Lawrence Livermore National Laboratory (USA). This setup made it possible to obtain a laser radiation flux density $\approx 10^{17}$ W/cm^2 with pulse duration ≈ 120 ps. Somewhat later, laser satellites were also observed in the VUV range.[4]

In the present work we recorded laser satellites in the emission spectra of magnesium and aluminum plasmas produced by femtosecond laser pulses. This was made possible by the realization of picosecond time resolution in a high-luminosity x-ray spectrograph with a spherically curved mica crystal. The temporal characteristics of the new spectral lines show unequivocally that the lines are formed as a result of the nonlinear processes discussed above.

EXPERIMENTAL ARRANGEMENT

The experiments were performed at the Center for Ultrafast Optical Science at the University of Michigan.

The x-ray spectra were excited by irradiating solid targets with a 400 fs laser pulse[5] with energy up to 2 J at the fundamental frequency ($\lambda = 1.053$ μm). A spherically curved mica crystal ($R = 186$ mm) focused the plasma radiation onto the photocathode of a

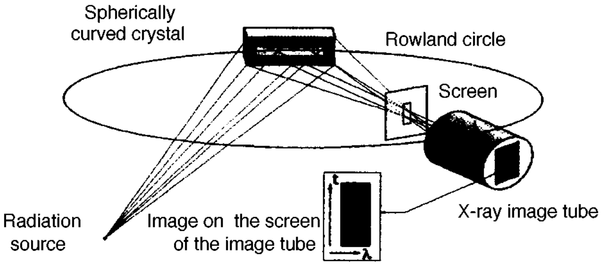

FIG. 2. Experimental arrangement for recording time-resolved x-ray spectra of a plasma.

Kentec x-ray camera in a slitless arrangement of a FSSR-1D spectrograph (see Fig. 2).[6] The spectral resolution of the system in the dynamic regime was not worse than $\lambda/\Delta\lambda \approx 5000$. The time resolution at the maximum scan rate was equal to 5–7 ps. The image from the camera screen was intensified with a multichannel plate light amplifier and recorded with a 12-bit CCD camera; this made possible wavelength referencing of the images obtained in different shots.

RESULTS AND DISCUSSION

In the present experiment the relative arrangement of the plasma, the spherical crystal, and the detection system was chosen so as to record the emission spectrum in the ranges 9.15–9.35 Å (in second-order reflection from the mica crystal) and 6.1–6.23 Å (in third-order reflection). In the case of a magnesium plasma this made it possible to observe the resonance and intercombination lines of the He-like ion Mg XI and their dielectronic satellites and, in the case of an aluminum plasma, the $1s5p\ ^1P_1 - 1s^2\ ^1S_0$ line of the He-like ion Al XII. Laser satellites due to the interaction of laser photons with the $1s2s\ ^1S_0$ state of the Mg XI ion and the $1s5s\ ^1S_0$ and $1s5d\ ^1D_2$ states of the Al XII ion should also fall into the indicated detection ranges.

In Ref. 1 it was shown that the intensity P of laser satellites can be estimated according to the equation

$$P(\mathrm{W/cm^3}) = \omega'/\omega_{\mathrm{las}}\, N_{B*} q_{\mathrm{las}} \sigma, \tag{1}$$

where $q_{\mathrm{las}}(\mathrm{W/cm^2})$ is the laser radiation flux density, $N_{B*}(\mathrm{cm^{-3}})$ is the population of the excited state B^* of the ion, the frequencies are $\omega' = \omega_{B*B*} \pm \omega_{\mathrm{las}}$, and σ is the Raman scattering cross section, which can be estimated in the approximation of one virtual level according to the formula

$$\sigma = \sigma_T [\omega_{\mathrm{las}} \omega'^3 (\omega_{kB*} + \omega_{kB})^2 f_{Bk} f_{B*k}] / \{4(\omega_{kB*} - \omega_{\mathrm{las}})^2 (\omega_{kB} + \omega_{\mathrm{las}})^2 \omega_{kB} \omega_{kB*}\}, \tag{2}$$

where $\sigma_T = (8\pi/3)(e^2/mc^2)^2$ is the Thomson cross section and f_{ij} is the oscillator strength for the transition $i \rightarrow j$.

Equation (1) can be rewritten, introducing the probability $A_{\mathrm{las}}(\omega')$ of induced transitions, as

$$P = \hbar \omega' N_{B*} A_{\mathrm{las}}(\omega'), \tag{3}$$

where $A_{\rm las}(\omega')=q_{\rm las}\sigma/\hbar\omega_{\rm las}$. When the energy $\hbar\omega'$ of the emitted photon falls in the x-ray range, the probabilities $A_{\rm las}(\omega_{B*B}+\omega_{\rm las})$ and $A_{\rm las}(\omega_{B*B}-\omega_{\rm las})$ are practically identical and therefore both laser satellites should have approximately equal intensities. One can see from Eqs. (2) and (3) that the most intense laser satellites are obtained if the state B^* possesses the same multiplicity as the lower level B of the transition, since then the oscillator strengths f_{Bk} and f_{B*k} will correspond to optically allowed transitions.

The interaction of a laser photon $\hbar\omega_{\rm las}=9524\ {\rm cm}^{-1}$ with the $1s2s\ ^1S_0$ state of a Mg XI ion should give two satellite lines with wavelengths $\lambda_{s1}\approx 9.2178$ Å and $\lambda_{s2}\approx 9.2341$ Å, since according to the calculations performed in Ref. 7, the energy of the $1s2s\ ^1S_0$ level equals $1.0839\times 10^7\ {\rm cm}^{-1}$. The probabilities $A_{\rm las}(\omega')$ of induced transitions can be estimated from Eqs. (2) and (3), taking the $1s2p\ ^1P_1$ state as the level k (see Fig. 1). Using the data given in Ref. 7 for the energies of the levels and oscillator strengths, we obtain $A_{\rm las}(\lambda_{S1,S2})\approx 1.5\times 10^{13}(q_{\rm las}/10^{17}\ {\rm W/cm^2})\ {\rm s}^{-1}$. For $q_{\rm las}>10^{16}\ {\rm W/cm^2}$ the probabilities $A_{\rm las}(\lambda_{S1,S2})$ are higher than the probabilities of collisional de-excitation of the $1s2s\ ^1S_0$ level and the intensities of the laser satellites can be estimated on the basis of a coronal model. Using the excitation rates of the $1s2p\ ^1P_1$ and $1s2s\ ^1S_0$ levels calculated in Ref. 8, we obtain for the ratio of the intensities of the laser satellites to the intensity of the resonance line

$$I(\lambda_{S1,S2})/I_R=1/2[\langle\nu\sigma(1s^2-1s2s\ ^1S_0)\rangle\langle\nu\sigma(1s^2-1s2p\ ^1P_1)\rangle]\approx 0.15, \tag{4}$$

where I_R is the intensity of the resonance line of the Mg XI ion and $\langle\nu\sigma\rangle$ are the rates of excitation of the $1s2s\ ^1S_0$ and $1s2p\ ^1P_1$ levels by electron impact from the $1s2s\ ^1S_0$ ground state. It is clear from Eq. (4) that the laser satellites are sufficiently intense to be detected experimentally. However, it should be underscored that if the laser satellites are emitted only during the time $\tau_{\rm las}$ of the interaction with the laser pulse, then the standard spectral lines are emitted during the plasma lifetime $\tau_{\rm plasma}$, which is determined by gasdynamic processes and, as a rule, is much longer (by 10–100 times) than the laser pulse. In consequence, when spectra are recorded without time resolution the average intensity of the laser satellites will be determined by the expression

$$\langle I_{s2}/I_R\rangle=\langle I_{s1}/I_R\rangle=1/2[\langle\nu\sigma(1s^2-1s2s\ ^1S_0)\rangle/\langle\nu\sigma(1s^2-1s2p\ ^1P_1)\rangle\tau_{\rm las}/\tau_{\rm plasma}] \tag{5}$$

which for the case of the present experiment gives ≈ 0.01, which does not exceed the noise level of the spectrograms.

The experimental results presented in Fig. 3 illustrate what we have said above. The time-integrated emission spectrum of a magnesium plasma in the range 9.15–9.35 Å is displayed in Fig. 3a, and the region of the spectrum near the intercombination line $1s2p\ ^3P_1$–$1s^2\ ^1S_0$ corresponding to two different times — during the laser pulse (curve *1*) and immediately after the pulse (curve *2*) — is shown in Fig. 3b. Figure 3b also shows a model spectrum (curve *3*) constructed in accordance with expression (6). It is seen from Fig. 3a that in the time-integrated spectrum the laser satellites are indeed indistinguishable against the background noise in the spectrogram. The laser satellites are similarly absent after the heating pulse ends (see curve *2* in Fig. 3b), while during the laser pulse (curve *1* in Fig. 3b) their position and intensity agree very well with the theoretical estimates (curve *3* in Fig. 3b).

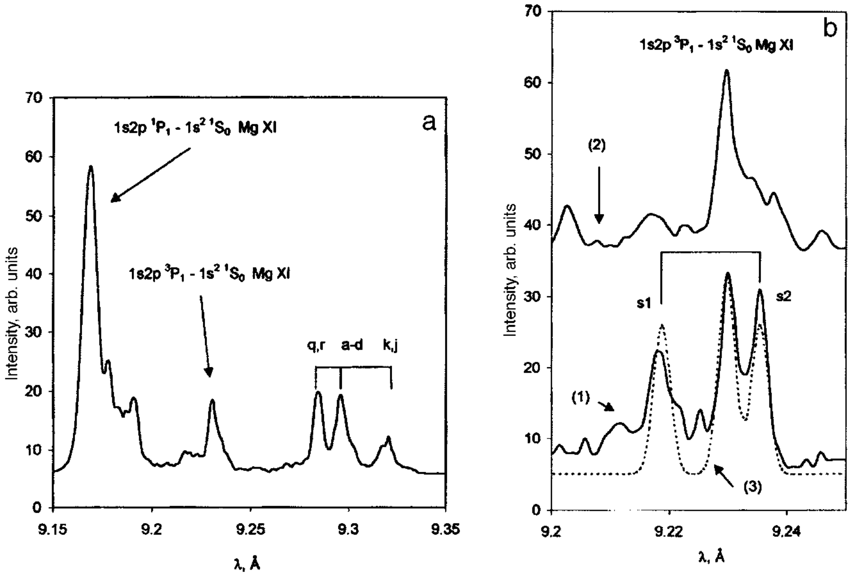

FIG. 3. a) Time-integrated emission spectrum of a femtosecond magnesium laser plasma; b) radiation from a magnesium plasma during the laser pulse (*1*) and immediately after the pulse (*2*). Curve *3* is the result of a theoretical modeling.

Similar results are also obtained for the laser satellites of the $1s5p\ ^1P_1 – 1s^2\ ^1S_0$ line of the He-like ion Al XII (see Fig. 4). In this case it is possible to observe four laser satellites, which are due to the interaction of the laser photons with the $1s5d\ ^1D_2$ state (lines a,c in Fig. 4) and the $1s5s\ ^1S_0$ state (lines b,d in Fig. 4). Using once again the coronal model and the estimates given in Ref. 9 for the excitation rates of the transitions $1s^2 \rightarrow 1s5l\ ^1L$ $(l = s,p,d)$, we find that at the plasma temperature $T_e \approx 200$ eV the intensities of these laser satellites should be ≈ 0.37 times the intensity of the allowed transition $1s5p\ ^1P_1 – 1s^2\ ^1S_0$. The model spectrum constructed in this manner (curve *3* in Fig. 4) corresponds to the experimental spectrum emitted during the laser pulse (curve *1* in Fig. 4). We underscore also that no lines are observed at the locations of the laser satellites in the spectrum emitted by the plasma immediately after the laser pulse (curve *2* in Fig. 4).

Since $E_{B*}[\text{cm}^{-1}] = 10^8(1/\lambda_{s1}[\text{Å}] + 1/\lambda_{s2}[\text{Å}]/2$, the detection of laser satellites provides a direct method for measuring the excitation energies of the metastable levels of ions (see Table I). It should be underscored, however, that in the presence of a strong laser field the levels will be shifted with respect to the levels of an isolated ion on account of the quadratic Stark effect. For example, for the $1s2s\ ^1S_0$ level of the ion Mg XI a simple estimate[10] gives $\Delta E = -6.6 \times 10^4 (q_{\text{las}}/10^{17}[\text{W/cm}^2])\ \text{cm}^{-1}$. For $q_{\text{las}} > 10^6$ W/cm^2 the shift is appreciably larger than the measurement error, and if the position of the level of an isolated ion is known, then it can be used to estimate the laser radiation flux density in the plasma. In our case, as follows from a comparison of the experimental results with the calculation performed in Ref. 7 for an isolated ion by the relativistic perturbation method allowing for QED corrections, the flux density did not exceed $q_{\text{las}} = 10^{16}$ W/cm^2.

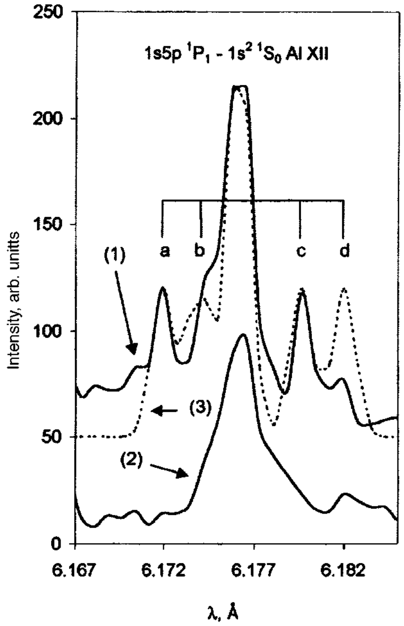

FIG. 4. a) Emission from an aluminum plasma during the laser pulse (*1*) and immediately after the pulse (*2*). Curve *3* is the result of a theoretical modeling.

In summary, the detection of x-ray emission from a plasma with picosecond time resolution achieved in the present work made it possible to observe laser satellites excited in a femtosecond laser plasma. The fact that the radiation in the observed spectral lines is emitted only during the interaction with the heating laser pulse indicates unequivocally that the lines are produced by the nonlinear interaction of laser photons with the excited states of multiply charged manganese and aluminum ions. Improvement of the time

TABLE I. Energies of metastable states of the He-like ions Mg XI and Al XII.

		Laser satellites		Energy, cm^{-1}	
Ion	Level	Transition	λ_{exp}, Å	experiment	theory[7]
Mg XI	$1s2s\ ^1S_0$	$(1s2s\ ^1S_0-1s^2\ ^1S_0+\omega_{\mathrm{las}}$ $1s2s\ ^1S_0-1s^2\ ^1S_0-\omega_{\mathrm{las}}$	9.2199(11) 9.2366(11)	$1.0836(3)\times 10^7$	1.0839×10^7
Al XII	$1s5s\ ^1S_0$	$1s5s\ ^1S_0-1s^2\ ^1S_0+\omega_{\mathrm{las}}$ $1s5s\ ^1S_0-1s^2\ ^1S_0-\omega_{\mathrm{las}}$	6.1732(8) 6.1813(8)	$1.6188(3)\times 10^7$	1.6188×10^7
Al XII	$1s5d\ ^1D_2$	$(1s5d\ ^1D_2-1s^2\ ^1S_0+\omega_{\mathrm{las}}$ $1s5d\ ^1D_2-1s^2\ ^1S_0-\omega_{\mathrm{las}}$	6.1712(8) 6.1789(8)	$1.6194(3)\times 10^7$	1.6192×10^7

Note. The experimental value for an ion in a laser field was determined from the equation $E[\mathrm{cm}^{-1}]=10^8(1/\lambda_{s1}[\text{Å}]+1/\lambda_{s2}[\text{Å}])/2$; the calculation in Ref. 7 was performed for an isolated ion.

resolution of the x-ray spectrograph and especially increasing the dynamic range of the detection system will make it possible in the future to investigate weaker, higher-order nonlinear processes.[11]

The investigation of laser satellites is important for a number of reasons. First, the observation of laser satellites makes it possible to perform direct measurements of the excitation energies of the metastable states of ions and it can also be used to measure the intensities of laser fields in a plasma. Second, since the laser satellites are emitted only during the interaction with the heating laser pulse, they can be used to produce a source of ultrashort x-ray pulses. Finally, in analyzing x-ray laser schemes in which the upper level of the laser transition is metastable (for example, lasers based on Ne- and Ni-like ions), one must allow for processes that lead to the generation of laser satellites.[3]

We thank I. L. Beĭgman for helpful discussions. This work was supported in part by the Russian Fund for Fundamental Research, Grant No. 96-02-16111.

[1] A. V. Vinogradov and E. A. Yukov, Kvantovaya Élektron. (Moscow), No. 2, 105 (1973) [Sov. J. Quantum Electron. **3**, 163 (1973)].

[2] I. Yu. Skobelev, A. Ya. Faenov, A. I. Magunov *et al.*, *Seventh International Conference on Multiphoton Processes*, Garmisch-Partenkirchen, Germany, September 30–October 4, 1996; publ. Institute of Physics Conference Proceedings 154, edited by P. Lambropoulos and H. Walther.

[3] A. Osterheld, B. K. F. Young, J. Dunn *et al.*, J. Quant. Spectrosc. Radiat. Transf. (1997), in press.

[4] H. R. Griem, R. C. Elton, and B. L. Welc, *Seventh International Workshop on Radiative Properties of Hot Dense Matter*, Santa Barbara, California, November 4–8, 1996.

[5] D. Strickland and G. Mourou, Opt. Commun. **56**, 219 (1985); P. Maine, D. Strickland, P. Bado *et al.*, IEEE J. Quantum Electron. **QE-24**, 398 (1988).

[6] I. Yu. Skobelev, A. Ya. Faenov, B. A. Bryunetkin *et al.*, Zh. Éksp. Teor. Fiz. **108**, 1263 (1995) [JETP **81**, 692 (1995)].

[7] V. A. Boĭko, V. G. Pal'chikov, I. Yu. Skobelev, and A. Ya. Faenov, *Spectroscopic Reference Data for Atoms and Ions* [in Russian], Izd. Standartov, Moscow, 1988.

[8] L. A. Vaĭnshteĭn, I. I. Sobel'man, and E. A. Yukov, *Excitation of Atoms and Spectral Line Broadening* [in Russian], Nauka, Moscow, 1979.

[9] R. A. Mewe, Astron. Astrophys. **136**, 906 (1962).

[10] H. Griem, *Spectral Line Broadening by Plasmas,* Academic Press, New York, 1974 [Russian translation, Mir, Moscow, 1978, p. 52].

[11] V. P. Gavrilenko and E. A. Oks, Kvantovaya Élektron. (Moscow) **10**, 1910 (1983) [Sov. J. Quantum Electron. **13**, 1269 (1983)].

Translated by M. E. Alferieff

Crystalline fields in systems with exchange and magnetoelastic interaction

A. S. Mishchenko
Kurchatov Institute Russian Science Center, 123182 Moscow, Russia

(Submitted 13 August 1997)
Pis'ma Zh. Éksp. Teor. Fiz. **66**, No. 7, 460–465 (10 October 1997)

The influence of the Kondo effect on the state of the crystalline field in the localized-moment regime is studied. It is shown that the exchange interaction leads to an anomalous temperature dependence of the intensity of the inelastic magnetic scattering of neutrons. An unconventional theory is constructed for the magnetoelastic interaction induced by Kondo scattering. The proposed model is in quantitative agreement with the results of neutron and thermodynamic investigations of the compound $CeAl_3$. © *1997 American Institute of Physics.* [S0021-3640(97)00319-8]

PACS numbers: 75.10.Dg, 75.20.Hr, 75.80.+q, 75.30.Et

1. The results of investigations[1,2] of the crystalline fields (CFs) at rare-earth ions (REIs) in cerium-based Kondo systems with almost-integral valence show an anomalous temperature dependence of the CF splittings Δ_{CF}. Even more puzzling is the result that the temperature dependence of the intensities of inelastic magnetic scattering of neutrons (IMSN) on transitions between the CF levels deviates from the function dictated by the statistical filling of the CF states ($Ce_{0.5}La_{0.5}Ni$ (Ref. 2) and $CeAl_3$ (Ref. 1)). The anomalies of the temperature dependence of the IMSN intensity cannot be attributed to a change in the degree of delocalization of the f electrons, since the relative change in valence is much lower than the relative deviation of the IMSN intensity from the standard dependence.

In the standard approaches, the CF Hamiltonian[3] and the magnetoelastic interaction Hamilton[4] are determined by sets of temperature-independent CF parameters $\{B_n^m\}$ and magnetoelastic interaction parameters $\{\widetilde{\mathcal{B}}^{\Gamma}_{\zeta\zeta'}\}$. However, when the CF states are formed under Kondo interaction conditions, an indirect ion–ion exchange interaction[5] leads to a temperature-dependent renormalization of the effective CF parameters.[6,7] It is obvious that the exchange interaction can give rise to characteristic features in the temperature dependence of the IMSN intensity and to nonstandard forms of the magnetoelastic interaction. In this letter we examine a number of higherto unstudied mechanisms which, as a result of the exchange interaction and nonstandard types of magnetoelastic interactions together with the exchange interation in Kondo systems, give rise to anomalies in the temperature dependence of the IMSN intensity in systems with almost-integral valence.

2. In a crystal the sixfold degenerate ${}^2F_{5/2}$ state of the Ce^{3+} ion $\{|\lambda\rangle \equiv |(2\lambda-7)/2\rangle;\ \lambda=1,\ldots,6\}$ splits into levels $\{\Gamma\nu\}$ with energies $E_{\Gamma}^{(0)}$ whose wave functions $|\Gamma\nu\rangle=\Sigma_{\lambda=1}^{6}a_{\Gamma\nu}^{\lambda}|\lambda\rangle$ transform according to the νth row of the irreducible representation

Γ of the point group $\mathcal{G}^{\,0}$ of the position of the REI. The IMSN intensity corresponding to the transition $|\Gamma_i\rangle \rightarrow |\Gamma_f\rangle$ in a polycrystalline material is proportional to the product of the filling factor $P_{\Gamma_i}(T)=\exp(-E^{(0)}_{\Gamma_i}/T)/\Sigma_{\Gamma\nu}\exp(-E^{(0)}_{\Gamma}/T)$ of the initial state and the matrix element

$$\Xi^{\alpha\beta}_{\Gamma_i\Gamma_f}=\sum_{\nu_i\nu_f}\sum_{\varepsilon\sigma\lambda\rho}[a^{\varepsilon}_{\Gamma_i\nu_i}a^{\lambda}_{\Gamma_f\nu_f}]^{*}a^{\sigma}_{\Gamma_f\nu_f}a^{\rho}_{\Gamma_i\nu_i}\langle\varepsilon|\hat{J}^{\alpha}|\sigma\rangle\langle\lambda|\hat{J}^{\beta}|\rho\rangle, \tag{1}$$

averaged over the Cartesian coordinates $\{\alpha,\beta\}=x,y,z$ ($\hat{J}^{\alpha}$ is the projection of the magnetic moment operator). The deviation of the temperature dependence of the IMSN intensity from the law dictated by the statistical filling of the CF levels could be due to a change in the coefficients $\{a^{\lambda}_{\Gamma\nu}\}$ of the wave functions of the states $|\Gamma_i\nu_i\rangle$ and $|\Gamma_f\nu_f\rangle$. It should be noted that a change in the coefficients $\{a^{\lambda}_{\Gamma\nu}\}$ should also lead to anomalies in the temperature dependence of the Raman scattering intensities.

3. In a Kondo system with an ideal lattice the state of the REI at the **0**th site is described by the sum of the CF Hamiltonian $\mathcal{H}_{\mathrm{CF}}(\mathbf{0})$

$$\mathcal{H}_{\mathrm{CF}}(\mathbf{0})=\sum_{\lambda\rho}\langle\lambda|\sum_{mn}^{\mathcal{G}^0}B^m_n\hat{O}^m_n|\rho\rangle\hat{L}_{\lambda\rho}(\mathbf{0}) \tag{2}$$

(where $\hat{O}^m_n$ are the Stevens operators, $\hat{L}_{\lambda\rho}(\mathbf{j})$ are operators describing the transformation $|\rho\rangle\rightarrow|\lambda\rangle$ of the state of the ion, and the summation in Eq. (2) extends over the operators $\hat{O}^m_n$ of the point group $\mathcal{G}^0$ of the position of the REI in an ideal lattice) and the exchange Hamiltonian $\mathcal{H}_{\mathrm{ex}}(\mathbf{0})$. The exchange interaction Hamiltonian is[6,7] the sum of the interactions with the nearest REIs at the sites $\mathbf{R}_j$; these interactions are characterized by the constants $I(\tau,\varsigma,|\mathbf{R}_j|)$, the exchange enhancement factor $\widetilde{f}(T/T_K,|\mathbf{R}_j|)\approx(\ln(T/T_K))^{n(|\mathbf{R}_j|)}$ ($n\leqslant 2$, T_K is the Kondo temperature) due to single-site Kondo scattering,[8] and the geometric anisotropy factor $D^{\lambda\rho}_{\varepsilon\sigma}(\tau,\varsigma,\theta_j,\varphi_j)$ (θ_j and φ_j are the angles of the spherical coordinate system relative to the quantization axis):

$$\mathcal{H}_{\mathrm{ex}}(\mathbf{0})=-\sum_{\lambda\rho}\hat{L}_{\lambda\rho}(\mathbf{0})\hat{\Upsilon}^{\lambda\rho}(T), \tag{3}$$

$$\hat{\Upsilon}^{\lambda\rho}(T)=\sum_{\mathbf{j}}\widetilde{f}(T/T_K,|\mathbf{R}_j|)\sum_{\varepsilon\sigma}\sum_{\tau\varsigma}I(\tau,\varsigma,|\mathbf{R}_j|)\mathcal{D}^{\lambda\rho}_{\varepsilon\sigma}(\tau,\varsigma,\theta_j,\varphi_j)\hat{L}_{\varepsilon\sigma}(\mathbf{j}) \tag{4}$$

($\lambda_{\rho\varepsilon\sigma\tau\varsigma}$ are the states of the ‘‘bare’’ (unrenormalized) basis $\{|\lambda\rangle\}$). In the mean field approximation the operator $\hat{\Upsilon}^{\lambda\rho}(T)$ is replaced by the number $\langle\hat{\Upsilon}^{\lambda\rho}(T)\rangle$ obtained from expression (4) by switching from the operator $\hat{L}_{\varepsilon\sigma}(\mathbf{j})$ to the mean value $\Sigma_{\Gamma'\nu'}\langle\Gamma'\nu'|\hat{L}_{\varepsilon\sigma}(\mathbf{j})|\Gamma'\nu'\rangle P_{\Gamma'}(T)$.

In the paramagnetic phase the exchange interaction (3) and the CF (2) have the same symmetry.[6,7] Therefore the exchange interaction in the mean field approximation can be expressed in terms of a renormalization of the CF parameters B^m_n (2): $\widetilde{B}^m_n(T)=B^m_n+[B^m_n]'(T)$.

The anomalous temperature dependence of the IMSN intensity has a simple explanation in the case of low symmetry, for which the coefficients $\{a^{\lambda}_{\Gamma\nu}\}$ of the wave functions of the CF states depend on the values of the CF parameters (trigonal, orthorhombic, and so on). The second trivial mechanism is realized in systems with defects. In such systems the symmetry of the environment of the REI at the **j**th state is lower than that of the ideal lattice. Since the CF at the REI is produced by the nearest-neighbor ions of all the sublattices and the exchange interaction is produced only by the nearest REIs, strictly speaking, the lowering of the CF symmetry to the group $\mathcal{G}^{\mathrm{imp}}_{\mathrm{CF}}(\mathbf{j})$ as a result of the imperfection of the lattice near the **j**th site must be distinguished from the lowering of the symmetry to the group $\mathcal{G}^{\mathrm{imp}}_{\mathrm{ex}}(\mathbf{j})$ generated at the REI by the exchange interaction. The first contribution δB^m_n is temperature-independent and the second one $[\delta B^m_n]'(T)$ is temperature-dependent. The final expression for the IMSN intensity must be averaged over the REI positions **j**, the local Hamiltonians of which are described by the site-independent parameters $\widetilde{B}^m_n(T)$ and the contributions $\Sigma^{\mathcal{G}^{\mathrm{imp}}_{\mathrm{CF}}(\mathbf{j})}_{mn}\delta B^m_n \hat{O}^m_n$ and $\Sigma^{\mathcal{G}^{\mathrm{imp}}_{\mathrm{ex}}(\mathbf{j})}_{mn}$ $\times[\delta B^m_n]'(T)\hat{O}^m_n$ that depend on the environment surrounding a given position.

It is possible[2] that the mechanisms considered above are responsible for the IMSN anomalies in $\mathrm{Ce_{0.5}La_{0.5}Ni}$. The role of the contributions from an ideal lattice and defects can be distinguished experimentally, for example, by studying samples with different degrees of imperfection.

4. The above-discussed mechanisms leading to a temperature dependence of the IMSN intensity are not applicable to perfect crystals of high symmetry, where the wave functions of the CF states do not depend on the CF parameters. An example of such a system is $\mathrm{CeAl_3}$, whose symmetry is described by the hexagonal point group $\overline{6}m2$. This system exhibits an anomalous temperature dependence of the IMSN intensity, even though the polycrystalline sample investigated in Ref. 1 was characterized by a high degree of perfection of the crystallites.

A possible mechanism of the IMSN anomalies is a lowering of the lattice symmetry on account of the dynamic distortion of the environment of the REIs by elastic modes. The characteristic time τ_{ac} of slow, low-energy acoustic modes $\{\epsilon^{\Gamma\zeta}_{\iota}\}$ is much longer than the time $\tau_{\exp}\sim\hbar/\Delta_{\mathrm{CF}}$ required for measurement of the inelastic transition between the CF states. Therefore the maximum of the IMSN peak is determined by the matrix element $\langle\Xi^{\alpha\beta}_{\Gamma_i\Gamma_f}\rangle_{\exp}$, which is an average (over the distribution function $\psi(\{\epsilon^{\Gamma\zeta}_{\iota}\})$ of the elastic distortions) value of the matrix element $\Xi^{\alpha\beta}_{\Gamma_i\Gamma_f}(\{\epsilon^{\Gamma\zeta}_{\iota}\})$ calculated in the distorted $\{\epsilon^{\Gamma\zeta}_{\iota}\}$ configuration of the lattice. The distribution function can be calculated if the parameters of the Hamiltonian $\mathcal{H}_L$ of the vibrational degrees of freedom and the constants $\{\widetilde{\mathcal{B}}^{\Gamma}_{\zeta\zeta'}\}$ in the Hamiltonian of the single-ion magnetoelastic interaction $\mathcal{H}_{me}$ are known[4,9,10]

$$\mathcal{H}_{me}=-\sum_{\Gamma}\sum_{\zeta\zeta'}\widetilde{\mathcal{B}}^{\Gamma}_{\zeta\zeta'}\sum_{\iota}\epsilon^{\Gamma\zeta}_{\iota}\hat{\mathcal{O}}^{\iota}_{\Gamma\zeta'}, \tag{5}$$

where $\epsilon^{\iota}_{\Gamma\zeta}(\hat{\mathcal{O}}^{\iota}_{\Gamma\zeta})$ are the distortion functions (spin functions) which form a basis of the n-dimensional $(\iota=1,2,\dots,n)$ representation Γ with the possible sets ζ. However, this calculation is made difficult by the fact that the parameters of the vibrational Hamiltonian $\mathcal{H}_L$ are unknown and also by the presence of anharmonicity (see Ref. 11 for $\mathrm{CeAl_3}$). For this reason, making use of the fact that the square modulus $|\psi(\{\epsilon_\iota^{\Gamma\zeta}\})|^2$ of the distribution function and the matrix element $\Xi_{\Gamma_i\Gamma_f}^{\alpha\beta}(\{\epsilon_\iota^{\Gamma\zeta}\})$ are even functions, one can use the theorem of the mean to calculate in the simplest approximation the maximum of the IMSN peak and to estimate $\langle\Xi_{\Gamma_i\Gamma_f}^{\alpha\beta}\rangle_{\mathrm{exp}}$ as the value of $\Xi_{\Gamma_i\Gamma_f}^{\alpha\beta}(\{\epsilon_\iota^{\Gamma\zeta}\})$ at the position of the average distortion $\langle\{|\epsilon_\iota^{\Gamma\zeta}|\}\rangle$: $\langle\Xi_{\Gamma_i\Gamma_f}^{\alpha\beta}\rangle_{\mathrm{exp}}\approx\Xi_{\Gamma_i\Gamma_f}^{\alpha\beta}(\langle\{|\epsilon_\iota^{\Gamma\zeta}|\}\rangle)$.

We note that (in accordance with the experimental situation[1] in $\mathrm{CeAl_3}$) on the basis of the proposed mechanism the linewidth should be greater than the observed effect of the renormalization, and the temperature dependence of the width of the inelastic peak should deviate strongly from the standard law.[12]

Since for weak distortions the renormalization of the coefficients of the wave functions is linear in the distortions, the change in the matrix element is $\Xi_{\Gamma_i\Gamma_f}^{\alpha\beta}(\langle\{|\epsilon|\}\rangle)\sim|\epsilon|$. The order of magnitude $|\epsilon|$ of the renormalization can be estimated from the measured[13] temperature dependence of the renormalization Δc of the elastic moduli in $\mathrm{CeAl_3}$: $|\epsilon|\sim[(\epsilon)^2]^{1/2}\sim(c)^{1/4}$. The estimates show that the standard magnetoelastic interaction[4,9,10] does not explain the sharp temperature dependence of the IMSN intensity in $\mathrm{CeAl_3}$, since in the experimental temperature interval $2<T<90$ K the renormalization $|\Delta c/c|\approx 0.1$ even with allowance for the background contribution of the lattice anharmonicity.[4] Moreover, the standard magnetoelastic interaction likewise does not make it possible to describe the elastic moduli correctly, since in Ref. 13 a splitting $\Delta_{3/2-5/2}=18$ K, which is much less than the actual value ≈ 70 K, had to be used in order to reproduce the observed sharp temperature dependence of $c(T)$.

5. However, since the highly anisotropic exchange interaction (3) specific to a Kondo system is more sensitive to symmetry-breaking lattice deformations than is the the distortion of the electrostatic field of the nearest-neighbor charges by the standard[4,9,10] magnetoelastic interaction (5), the exchange interaction should make the dominant contribution to the magnetoelastic effects in such systems. As a result of the temperature dependence of the exchange interaction itself, the magnetoelastic interaction with exchange differs in an important way from the interaction in the standard approaches (5): The temperature dependences of the computed physical quantities are sharper.

The symmetry of the exchange interaction in the mean field approximation is identical to that of the CF contribution. Therefore, since the $\langle\hat{\Upsilon}^{\lambda\rho}(T)\rangle$ are numbers, the form of the magnetoelastic interaction Hamiltonian with the exchange interaction can be written down on the basis of the same symmetry considerations[10] as the standard Hamiltonian: as a sum of terms which are each a scalar invariant formed from elastic functions and spin operators belonging to the same irreducible representation:

$$\mathcal{H}_{me}^{\mathrm{ex}}=-\sum_{\Gamma}\sum_{\zeta\zeta'}\widetilde{C}^{\,\Gamma}_{\zeta\zeta'}(T)\,\epsilon_\iota^{\Gamma\zeta}\hat{\mathcal{O}}^{\iota}_{\Gamma\zeta'}\,, \tag{6}$$

where the scalar constants $\widetilde{C}^{\Gamma}_{\zeta\zeta'}(T)$ are represented in the form of the contraction

$$\widetilde{C}^{\,\Gamma}_{\zeta\zeta'}(T)=\sum_{\lambda\rho}\widetilde{\mathcal{R}}^{\,\lambda\rho}_{\zeta\zeta'\Gamma}\langle\hat{\Upsilon}^{\lambda\rho}(T)\rangle \tag{7}$$

($\widetilde{\mathcal{R}}^{\lambda\rho}_{\zeta\zeta'\Gamma}$ are the magnetoelastic interaction parameters). The effective Hamiltonian (3) differs from the standard Hamiltonian by the temperature dependence of the factors $\widetilde{C}^{\Gamma}_{\zeta\zeta'}(T)$, which introduce an additional temperature dependence in all computed quantities. The exchange-enhancing factor $\widetilde{f}(T/T_K,|\mathbf{R}_j|)$ due to single-site Kondo scattering is manifested at temperatures close to T_K, and the thermodynamic averaging over the CF states gives rise to features at temperatures $T \lesssim \Delta_{\mathrm{CF}}$. The problem of calculating the microscopic parameters can be solved by a first-principles calculation using the methods of Ref. 14. However, in the case of a hexagonal lattice the main contributions can be analyzed on the basis of symmetry considerations.

6. The CF states in $\mathrm{CeAl_3}$ are doublets $|\pm 3/2\rangle$, $|\pm 1/2\rangle$, and $|\pm 5/2\rangle$. Therefore the ‘‘bare’’ nomenclature $\{\lambda\rho\varepsilon\sigma\tau\varsigma\}$ corresponds to the CF nomenclature $\{\Gamma'\nu'\}$ for the undistorted lattice, and the operator $\hat{L}_{\varepsilon\sigma}(\mathbf{j})$ is diagonal in both representations. For this reason, in calculating the mean value $\langle\hat{\Upsilon}^{\lambda\rho}(T)\rangle$ by perturbation theory (i.e., without performing the self-consistency procedure[7]) one must set $\Gamma'\nu'=\varepsilon=\sigma$:

$$\langle\hat{\Upsilon}^{\lambda\rho}(T)\rangle=\sum_{\mathbf{j}}\widetilde{f}(T/T_K,|\mathbf{R}_j|)\sum_{\Gamma'\nu'}\sum_{\tau\varsigma}I(\tau,\varsigma,|\mathbf{R}_j|)\mathcal{D}^{\lambda\rho}_{\Gamma'\nu',\Gamma'\nu'}(\tau,\varsigma,\theta_j,\varphi_j)P_{\Gamma'}(T). \tag{8}$$

Therefore the constants $\widetilde{C}^{\Gamma}_{\zeta\zeta'}(T)$ can be expressed in terms of the phenomenological parameters $\Lambda^{\Gamma}_{\Gamma'}(\zeta,\zeta')$:

$$\widetilde{C}^{\Gamma}_{\zeta\zeta'}(T)=\sum_{\Gamma'}P_{\Gamma'}(T)\Lambda^{\Gamma}_{\Gamma'}(\zeta,\zeta'), \tag{9}$$

$$\Lambda^{\Gamma}_{\Gamma'}(\zeta,\zeta')=\sum_{\mathbf{j}}\widetilde{f}(T/T_K,|\mathbf{R}_j|)\sum_{\nu'}\sum_{\tau\varsigma}I(\tau,\varsigma,|\mathbf{R}_j|)\mathcal{D}^{\lambda\rho}_{\Gamma'\nu',\Gamma'\nu'}(\tau,\varsigma,\theta_j,\varphi_j)\widetilde{\mathcal{R}}^{\lambda\rho}_{\zeta\zeta'\Gamma}. \tag{10}$$

To calculate the renormalizations of the CF splittings observed in the neutron scattering in $\mathrm{CeAl_3}$ and the IMSN anomalies we confine our attention to the magnetoelastic interaction with the modes $\{\epsilon^{\alpha,1},\epsilon^{\alpha,2},\epsilon^{\gamma}_1,\epsilon^{\gamma}_2\}$.[10] To decrease the number of phenomenological parameters, we assume that $\langle|\epsilon^{\alpha,1}|\rangle=\langle|\epsilon^{\alpha,2}|\rangle\equiv\langle|\epsilon^{\alpha}|\rangle$; $\langle|\epsilon^{\gamma}_1|\rangle=\langle|\epsilon^{\gamma}_2|\rangle\equiv\langle|\epsilon^{\gamma}|\rangle$; $\theta_1=\Lambda^{\alpha}_{1/2}/\Lambda^{\alpha}_{3/2}=\Lambda^{\gamma}_{1/2}/\Lambda^{\gamma}_{3/2}$; $\theta_2=\Lambda^{\alpha}_{5/2}/\Lambda^{\alpha}_{3/2}=\Lambda^{\gamma}_{5/2}/\Lambda^{\gamma}_{3/2}$. This gives the following Hamiltonian for calculating the renormalization of the position of the peak and the absolute IMSN intensity:

$$\mathcal{H}^{\mathrm{ex}}_{me}=[F_{\alpha}\hat{\mathcal{O}}^{\alpha}+F_{\gamma}\hat{\mathcal{O}}^{\gamma}](\ln(T/T_K))^{n}[P_{3/2}(T)+\vartheta_1P_{1/2}(T)+\vartheta_2P_{5/2}(T)], \tag{11}$$

$$\hat{\mathcal{O}}^{\alpha}=(\hat{J}^{z})^2-J(J+1)/3;\quad \hat{\mathcal{O}}^{\beta}=(\hat{J}^{x})^2-(\hat{J}^{y})^2+\hat{J}^{x}\hat{J}^{y}+\hat{J}^{y}\hat{J}^{x}, \tag{12}$$

$$F_{\alpha}=-\sqrt{3}\Lambda^{\alpha}_{3/2}\langle|\epsilon^{\alpha}|\rangle;\quad F_{\gamma}=\Lambda^{\gamma}_{3/2}\langle|\epsilon^{\gamma}|\rangle. \tag{13}$$

The ‘‘bare’’ values of the energies, which are eigenvalues of the CF Hamiltonian of the undistorted lattice, were used: $E_{|\pm 3/2\rangle}=0$ K, $E_{|\pm 1/2\rangle}=66$ K, and $E_{|\pm 3/2\rangle}=174$ K. It can be concluded from the computational results presented in Fig. 1 that if the Kondo exchange-enhancement factor is neglected, the temperature dependence of the CF split-

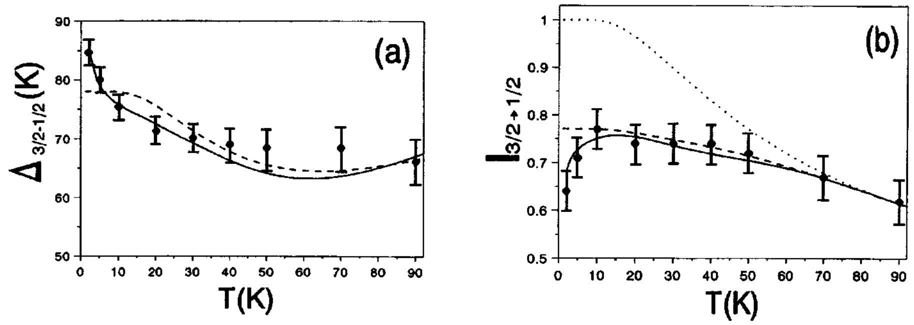

FIG. 1. Temperature dependence of the splitting $\Delta_{3/2-1/2}$ (a) and of the IMSN intensity $I_{3/2\rightarrow 1/2}$ (normalized to 1 at $T=0$) (b) in $\mathrm{CeAl_3}$: in the standard model — dotted line; in the model (11)–(13) without the Kondo enhancement factor ($F_\alpha=5.84$ K, $F_\gamma=4.67$ K, $\theta_1=-0.67$, $\theta_2=-5.0$) — dashed line, and with the Kondo enhancement factor $(\ln(T/T_K))^n$ ($F_\alpha=10.8$ K, $F_\gamma=6.5$ K, $\theta_1=-0.2$, $\theta_2=-7.0$, $T_K=0.8$ K, $n=0.27$) — solid line. The experimental points were taken from Ref. 1.

tings and the IMSN intensity, which is caracterized by a temperature scale $T\lesssim\Delta_{\mathrm{CF}}$, is in quantitative agreement with the experimental data at temperatures $T\gtrsim 10$ K $\gg T_K\sim 1$ K. The renormalization of the wave functions by the magnetoelastic interaction (11)–(13) decreases the IMSN intensity as a result of an increase in the intensity of the quasielastic component: Instead of the total scattering cross sections which are standard for hexagonal symmetry in the limit $T\rightarrow 0$ K, viz., $I_{qe}\equiv I_{3/2\rightarrow 3/2}=1.0$ barn/Ce, $I_{3/2\rightarrow 1/2}=1.78$ barn/Ce, $I_{3/2\rightarrow 5/2}=1.12$ barn/Ce, the absolute values with Eqs. (11)–(13) taken into account assume the values ≈ 1.70 barn/Ce, ≈ 1.42 barn/Ce, and ≈ 0.78 barn/Ce, respectively. Allowance for the Kondo exchange-enhancement factor $\tilde{f}(T/T_K,|\mathbf{R}_j|)\approx(\ln(T/T_K))^n$, which becomes substantial at $T\gtrsim T_K$, gives quantitative agreement with experimental data at lower temperatures as well (see Fig. 1). It should be noted that, strictly speaking, the expression obtained[8] for $\tilde{f}(T/T_K,|\mathbf{R}_j|)$ in the noncrossing approximation (NCA) diverges as $T\rightarrow T_K$ and is applicable only at temperatures which are quite high compared with T_K, i.e., in the localized-moment regime. At temperatures $T\approx T^*\gtrsim T_K$ Kondo scattering is suppressed by the formation of a strongly correlated state from the spins of the ground-state doublet of the CF,[8,15,16] and the problem of the magnetoelastic interaction at temperatures $T<T^*$ requires additional analysis.

7. The proposed mechanism of magnetoelastic renormalization can result in, besides spectroscopic effects, characteristic features in the temperature dependence of the elastic moduli and in the linear expansion and magnetostriction coefficients. This mechanism can also be observed in Kondo systems which are not in the localized-moment regime, provided that the strongly correlated low-lying states interact strongly with single-site excitations of the crystal field.[16] The magnetoelastic renormalization of the CF should lead to an unusual absorption line shape, which can be investigated experimentally by Raman scattering, for example, which has a much higher resolution than the inelastic neutron scattering technique.

I am deeply grateful to P. A. Alekseev, K. A. Kikoin, M. N. Kiselev, E. S. Klement’ev, and V. N. Lazukov for critical discussions. This work was supported by the

Russian Fund for Fundamental Research (Project No. 95-02-04250a), the International Association INTAS (Project No. 93-2834), and the Netherlands organization for the support of scientific research NWO (Project No. 07-30-002).

[1] P. A. Alekseev, W. Büher, V. N. Lazukov *et al.*, Physica B **217**, 241 (1996).
[2] V. N. Lazukov, P. A. Alekseev, E. S. Klement'ev *et al.*, submitted for publication.
[3] M. T. Hutchings, in *Solid State Physics*, edited by F. Seitz and D. Turnbull, Academic Press, New York, 1964, Vol. 16, pp. 227–273.
[4] P. Thalmeier and B. Lüthi, in *Handbook on the Physics and Chemistry of Rare Earths*, edited by K. A. Gschneider, Jr. and L. Eyring, North-Holland, Amsterdam, 1985, Vol. 14, p. 225.
[5] B. Cornut and B. Coqblin, Phys. Rev. B **5**, 4541 (1972).
[6] B. R. Cooper, R. Siemann, D. Yang *et al.*, in *Handbook on the Physics and Chemistry of the Actinides*, edited by A. J. Freeman and G. H. Lander, North-Holland, Amsterdam, 1985, Vol. 2, p. 435.
[7] N. Kioussis, B. R. Cooper, and A. Banerjea, Phys. Rev. B **38**, 9132 (1988).
[8] K. A. Kikoin, M. N. Kiselev, and A. S. Mishchenko, JETP Lett. **60**, 600 (1994); Zh. Éksp. Teor. Fiz. **112**, 729 (1997) [JETP **85**, 399 (1997)].
[9] E. R. Callen and H. B. Callen, Phys. Rev. **129**, 578 (1963).
[10] E. R. Callen and H. B. Callen, Phys. Rev. A **129**, 455 (1965).
[11] B. B. Voronov, A. I. Korobov, and V. V. Moshchalkov, JETP Lett. **47**, 413 (1988).
[12] K. W. Bekker, P. Fulde, and J. Keller, Z. Phys.: Condens. Matter B **28**, 9 (1974).
[13] M. Niksch, B. Lüthi, and K. Andres, Phys. Rev. B **22**, 5774 (1980).
[14] Q. G. Sheng and B. R. Cooper, Phys. Rev. B **50**, 965 (1994).
[15] K. A. Kikoin, M. N. Kiselev, and A. S. Mishchenko, Physica B **230–232**, 490 (1997).
[16] Yu. Kagan, K. A. Kikoin, and A. S. Mishchenko, Phys. Rev. B **55**, 12348 (1997).

Translated by M. E. Alferieff

Diffractional enhancement of the Kerr magnetooptic effect

V. Eremenko, V. Novosad, and V. Pishko
Physicotechnical Institute of Low Temperatures, 310164 Kharkov, Ukraine

O. Geoffroy and Y. Souche
Laboratoire de Magnétisme Louis Néel, CNRS/UJF 380164 Grenoble, BP166, France

B. Pannetier
CRTBT, CNRS/UJF, 38042 Grenoble, BP166, France

(Submitted 25 August 1997)
Pis'ma Zh. Éksp. Teor. Fiz. **66**, No. 7, 466–469 (10 October 1997)

The results of investigations of the transverse Kerr effect on an array of thin magnetic strips deposited on a silicon substrate are reported. The periodic structure of the sample gives rise to diffraction. It is observed that under certain experimental conditions the magnitude of the effect measured in diffracted beams is much greater than the maximum value for a sample with a uniform surface. © *1997 American Institute of Physics.* [S0021-3640(97)00419-2]

PACS numbers: 78.20.Ls, 78.20.Jq

We report the results of measurements of the transverse Kerr magnetooptic effect (TKMOE) for a periodic array of magnetic strips deposited on a nonmagnetic substrate. The investigation of the physical properties of such structures is unquestionably of interest from both the fundamental and applied standpoints.[1] When the sample is illuminated with a laser beam whose wavelength is several times shorter than the period of the array, besides the reflected beam, several diffracted beams are observed. Magnetooptic effects are observed not only in reflected but also in diffracted beams.[2] Such experiments have been previously performed in order to study magnetization reversal of microscopic magnetic particles at a submicron level.[3]

The quality of the experimental samples is especially important in studying magnetooptic effects on periodic structures in the optical range. The sample was fabricated by the following procedure. First, an array of parallel strips of an organic material was deposited on a flat surface of a single-crystal silicon wafer by means of optical lithography. Next a 0.07-μm-thick amorphous film of the ferromagnetic alloy Fe_3Si was deposited on top of that. A magnetron-type cathodic sputtering apparatus with the following deposition parameters was used: working gas (Ar) pressure 10 Pa, ion current 40 mA, and substrate temperature 78 K. Then the sample was placed for some time in a medium consisting of an organic solvent, so that ultimately only an array of magnetic strips with a period of 3.5 μm and strip width 0.5 μm remained on the 10×10 mm silicon substrate. The surface of the finished sample is shown in Fig. 1. The image was obtained with an atomic force microscope.

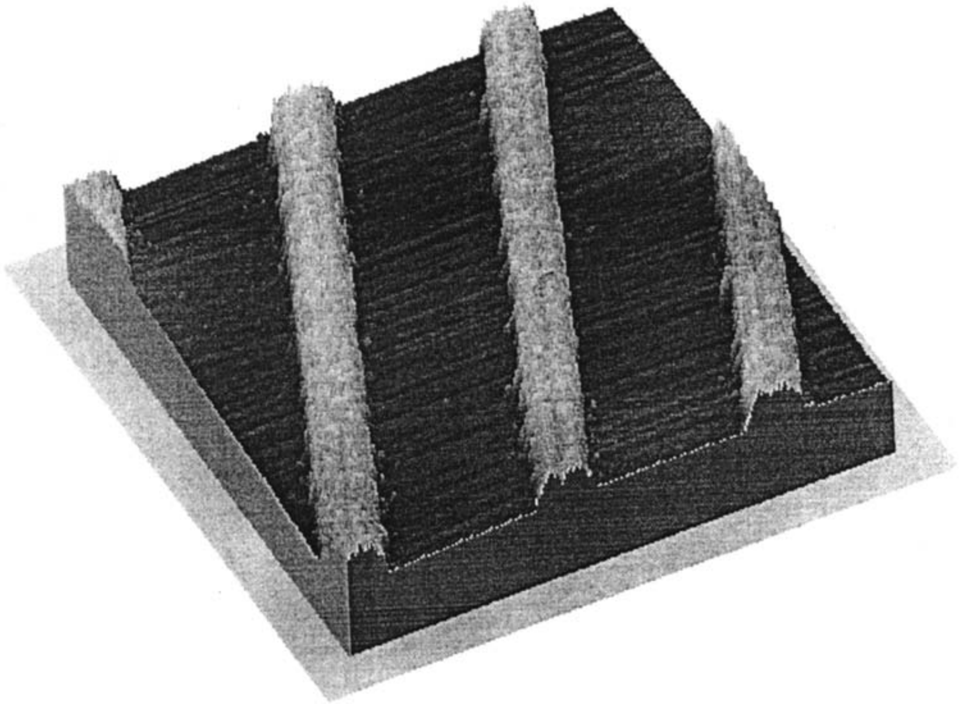

FIG. 1. Image of a portion of the surface of a sample of an array of magnetic strips deposited on a silicon substrate. The vertical scale is magnified by a factor of 10. The geometric dimensions are given in the text.

The transverse Kerr magnetooptic effect is observed in the case when the external magnetic field is perpendicular to the plane of incidence and reflection of the light. The effect is ordinarily characterized by the relative change $\Delta I/I$ in the intensity of the light reflected from the surface of the sample upon magnetization reversal of the sample. In the TKMOE measurements the diffraction grating was secured between the poles of an electromagnet, placed on the turntable of a goniometer in a manner so that the external magnetic field was parallel to the magnetic strips in the array and perpendicular to the plane containing the reflected and diffracted beams. A magnetic field of 0.025 T was sufficient for complete magnetization reversal of the magnetic strips. The goniometer made it possible to rotate the sample and to move the detector independently in order to perform measurements with different angles of incidence of the light. Infrared ($\lambda = 780$ nm) and red ($\lambda = 670$ nm) laser diodes as well as an argon laser operating in the green ($\lambda = 514.5$ nm) and blue ($\lambda = 488$ nm) regions were used as the light source. The light was polarized in the plane of diffraction. The diffracted light was detected with a photodiode and, after amplification, was analyzed with a personal computer. The measurement error in the magnitude of the Kerr effect did not exceed 5%. The results obtained for different wavelengths are essentially the same, so that we shall discuss the measurements performed using the most stable, red light source.

We measured experimentally the quantity $\Delta I_n/I_n$ in the nth-order diffracted beams

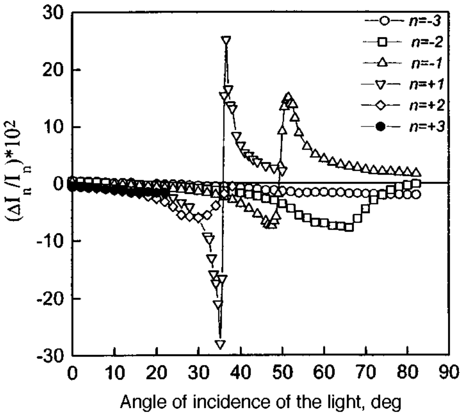

FIG. 2. Transverse Kerr magnetooptic effect measured in the diffracted beams ($n = \pm 1, \pm 2, \pm 3$) versus the angle of incidence.

as a function of the angle of incidence of the light. The half sum of the intensities of the diffracted light measured at the maximum values of the magnetization reversing field is denoted by I_n. Figure 2 displays the values of the TKMOE for $n = \pm 1$, ± 2, and ± 3 at angles of incidence ranging from 0 to 90°. The angular dependence of the effect differs strongly for different diffracted beams. For each beam there is a maximum at certain angles of incidence: For the $+1$st beam the effect reaches its maximum magnitude of 28% at an angle of incidence of 35°. For other beams the maximum effect is smaller but also significant: 14% for the -1st beam, 8% for the -2nd beam, and 6% for the $+2$nd beam. It should be noted that the maximum possible value of the TKMOE for a continuous Fe_3Si thin film equals only 1.8% with an angle of incidence of 69°. Previous measurements performed on a raised array with a continuous magnetic coating did not show a large enhancement of the TKMOE. The effect reached only 4% in the first diffracted beam.[4]

Figure 3 shows the angular dependence of the intensities I_n in the diffracted beams, normalized to the intensity of the incident light. Comparing Figs. 2 and 3, we can see that the effect increases in the range of angles of incidence, in which the intensity of the diffracted light is lowest. Furthermore, the TKMOE changes sign when the light intensity for the ± 1 diffracted beams has a local minimum. This phenomenon is also observed in the case of reflection from a uniform surface near the magnetic pseudo-Brewster angle.[5]

With rare exceptions, the Kerr magnetooptic effects are very weak. For this reason, a number of methods of enhancement have been proposed for applied purposes: coating the surface of a magnetic sample with a dielectric film,[6,7] depositing a magnetic film on a nonmagnetic, conducting substrate,[8] or using complicated multilayer structures.[9] In these methods the magnetooptic effects were enhanced by a decrease in the reflectivity of the samples. Interference cancellation of the reflected light was achieved by choosing optimal thicknesses of the films and materials employed. We assume that the enhancement of TKMOE by an array of magnetic strips is due to the cancellation between the light interacting with the surface of the magnetic strips and the light interacting with the

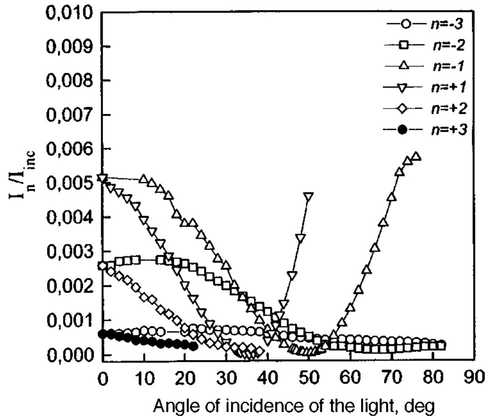

FIG. 3. Angular dependence of the normalized light intensity in different diffracted beams.

nonmagnetic substrate. For some angles of incidence, this results in a substantial decrease in I_n in the diffracted beams. The magnitude of the change ΔI_n in the intensity of the diffracted light in this case does not have local minima. Therefore the magnetooptic effect $\Delta I_n/I_n$ increases substantially. The factors influencing the enhancement of the Kerr effect are the ratios of the dimensions of the magnetic and nonmagnetic parts of the surface of the sample. Furthermore, optical diffraction makes it possible to observe the effect at angles which are inaccessible to standard reflection from a flat sample. Numerical modeling using a rigorous electromagnetic theory of diffraction can indicate optimal methods for enhancing Kerr magnetooptic effects on arrays of magnetic strips.[10]

We plan to investigate other Kerr effects on samples of this type.

[1] B. Barbara, J. Magn. Magn. Mater. **156**, 123 (1996).
[2] Y. Souche, M. Schlenker, and A. D. dos Santos, J. Magn. Magn. Mater. **140–144**, 2179 (1995).
[3] O. Geoffroy, D. Givord, Y. Otani *et al.*, J. Magn. Magn. Mater. **121**, 516 (1993).
[4] Y. Souche, O. Geoffroy, V. Novosad *et al.*, J. Magn. Soc. Jpn., Suppl. No. S1, **20**, 393 (1996).
[5] J. Futterman, Am. J. Phys. **63**, 471 (1995).
[6] A. V. Sokolov, *Optical Properties of Metals*, Blackie, London, 1967 [Russian original, Izd. Fiz.-Mat. Lit., Moscow, 1961].
[7] R. P. Hunt, J. Appl. Phys. **38**, 1215 (1967).
[8] T. Katayama, Y. Suzuki, H. Awano *et al.*, Phys. Rev. Lett. **60**, 1426 (1988).
[9] G. A. N. Connel, R. Allen, and M. Mansuripur, J. Magn. Magn. Mater. **35**, 337 (1983).
[10] G. Tayeb, R. Petit, and M. Cadilhac, Proc. SPIE **813**, 407 (1987).

Translated by M. E. Alferieff

Direct observation of ferromagnetic order in electrochemically oxygenated $La_2CuO_{4+\delta}$

E. L. Vavilova and N. N. Garif'yanov[a)]
Kazan Physicotechnical Institute, Kazan Science Center of the Russian Academy of Sciences, 420029 Kazan, Russia

(Submitted 26 August 1997)
Pis'ma Zh. Éksp. Teor. Fiz. **66**, No. 7, 470–474 (10 October 1997)

The magnetic properties of electrochemically oxygenated $La_2CuO_{4+\delta}$ are investigated for different values of δ. It is found that ferromagnetism appears after excess oxygen is introduced. It is shown that the ferromagnetic order vector is directed perpendicular to the Cu–O plane. The evolution of the magnetic-field dependence of the magnetization is investigated as the oxygen index is increased. The results are explained with allowance for the presence of phase separation in the oxygen-doped La_2CuO_4 and the possibility that a redistribution of the excess oxygen occurs as the degree of doping changes. © *1997 American Institute of Physics.* [S0021-3640(97)00519-7]

PACS numbers: 75.50.Cc, 82.45.+z

It is well known that the compound La_2CuO_4 is an antiferromagnet with latent ferromagnetism. Behavior of the ferromagnetic type is observed in this compound in high magnetic fields.[1] The existence of ferromagnetic correlations, starting with zero fields, is indicated in many works (see, for example, Ref. 2). However, thus far such ferromagnetic order has never been observed directly. It is conjectured that various disruptions of stoichiometry can promote the appearance of ferromagnetism. It is of interest to investigate how the magnetic properties are affected by the disruptions of stoichiometry that engender superconductivity. In the present work we investigated the magnetic properties of $La_2CuO_{4+\delta}$ with different amounts of excess oxygen.

A sample of powdered La_2CuO_4 was prepared by the standard method from a mixture of nitrates of the corresponding metals. Electrochemical oxygenation was conducted in a NaOH solution.[3] At the same time, a control sample of La_2CuO_4 was immersed in an electrolyte without being connected to a circuit. To change the excess oxygen content the sample was subjected after oxygenation to successive stepped anneals in air.[4] The magnetic properties were investigated with a SQUID magnetometer at successive stages of treatment of the sample (see Table I).

The temperature dependence of the magnetic susceptibility of the sample at different stages of heat treatment is displayed in Fig. 1. Superconductivity appears at 40 K immediately after oxygenation (state *2*). Figure 2 displays the results of measurements of the magnetic field dependence of the magnetization of the sample at different stages of treatment. In the initial state *1* of the sample the field dependence of the magnetization has the form typical for La_2CuO_4. After oxygenation the field dependence becomes

TABLE I. Approximate excess oxygen content as a function of the conditions of treatment of the sample.

	Sample No.				
	1	2	3	4	5
$T_{\rm treat}$, °C	–	–	300	400	500
δ	0	0.1	0.01	0.005	0

highly nonlinear. The magnetization is observed to increase with heat treatment. Finally, after a prolonged anneal, which decreases the oxygen index to 4, the form of the curve becomes similar to the initial state *1*.

After excess oxygen was introduced, investigation of the behavior of the magnetization as a function of the direction of the magnetic field revealed hysteresis. The hysteresis loop at stage *2* ($\delta \approx 0.1$) is shown in Fig. 3. We note that at stage *4* the coercive force is much weaker than at stages *2* and *3* (Fig. 4). Measurements of the temperature dependence of the remanent magnetization (in a zero magnetic field) at stage 2 are shown in Fig. 5.

To investigate the anisotropy of the observed ferromagnetic order, the powdered sample was subjected to a magnetic orientation procedure in accordance with Ref. 6. The x-ray crystallographic analysis of such an oriented sample showed that the *c* axes of a large number of crystallites are directed parallel to one another. Investigation of the magnetic properties of this sample showed that the remanent magnetization with the initial field oriented parallel to the *c* axis is two times higher than in the case of a perpendicular orientation of the field.

Investigation of a control sample which was also subjected to annealing showed that

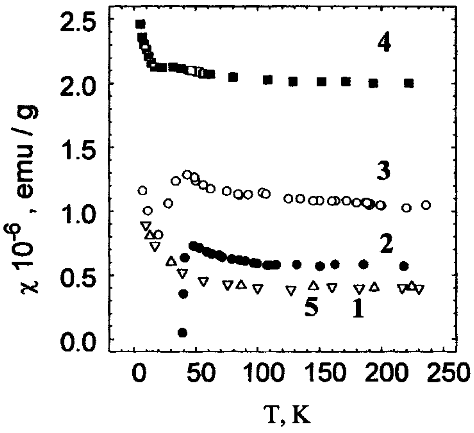

FIG. 1. Temperature dependence of the magnetic susceptibility in a 5 kOe field ($T = 50$ K): *1* — Initial state, *2* — after oxygenation, *3* — after heat treatment at 300 °C, *4* — after heat treatment at 400 °C, *5* — after heat treatment at 500 °C.

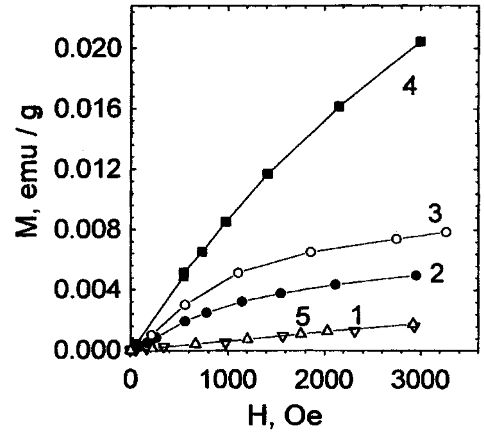

FIG. 2. Magnetization versus the magnetic field, with the magnetic field increasing from zero ($T=50$ K): *1* — Initial state, *2* — after oxygenation, *3* — after heat treatment at 300 °C, *4* — after heat treatment at 400 °C, *5* — after heat treatment at 500 °C.

at all stages of treatment it in no way differs from the initial state *1*.

The behavior of the magnetization as a function of the field, as shown in Fig. 3, is characteristic for ferromagnetic ordering. It is known[7] that phase separation into enriched and stoichiometric regions is observed in oxygen-supersaturated $La_2CuO_{4+\delta}$. As was shown in our previous work, the enriched regions also contain several phases with a different oxygen content.[4] In the present work, we studied the NQR spectra of ^{139}La nuclei and curves of the superconducting transitions of electrochemically oxygenated $La_2CuO_{4+\delta}$ samples. The total fraction of oxygen-enriched phases can be estimated from the NQR spectra as 80%. At the same time, it follows from magnetic susceptibility measurements of superconducting transitions that the fraction of the superconducting phases does not exceed 20%. Therefore not all phases containing additional oxygen are

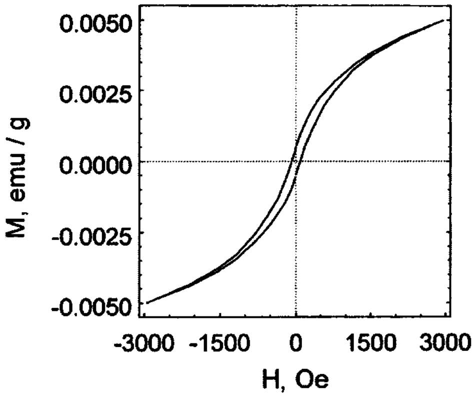

FIG. 3. Hysteresis loop for a post-oxygenation state of the sample (state *2*); $T=50$ K.

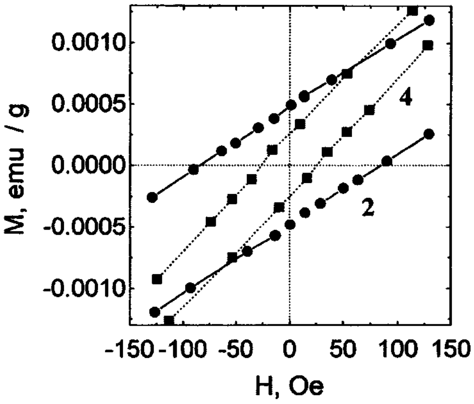

FIG. 4. Low-field part of the hysteresis loop for states *2* and *4*, $T=50$ K.

superconducting. Apparently it is those regions with not very high excess oxygen concentration (and, correspondingly, carrier density) that can be ferromagnetic.

The appearance of ferromagnetic order immediately after oxygenation indicates that the ferromagnetic ordering is produced by doping. In such a case, a change in the degree of doping should influence the characteristics of the ferromagnetic order which appears. Indeed, the behavior of the magnetization as a function of the field is different at different stages of heat treatment of the sample (Fig. 2). We note that the susceptibility increases with decreasing oxygen index (Fig. 1), while the magnetic susceptibility remains virtually temperature-independent for all δ. Therefore the increase in the magnetic moment as a result of heat treatment cannot be due to the appearance of a paramagnetic contribution. During heat treatment of a sample with large δ, excess oxygen escapes mainly from regions with the highest excess oxygen content. In the process, these regions pass into a phase with a low excess oxygen content.[4] Thus, when a sample passes from the state *2* ($\delta \approx 0.1$) into the state *3* ($\delta \approx 0.01$), the volume of the ferromagnetic regions increases.

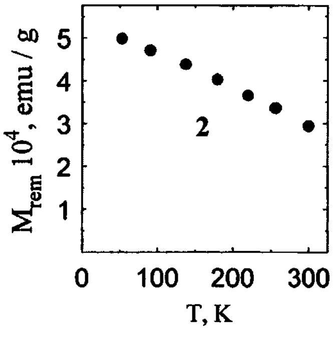

FIG. 5. Temperature dependence of the remanent magnetization of the sample after oxygenation (state *2*).

This should increase the magnetization loop (Fig. 2). A sample in stage 3 ($\delta \approx 0.01$) already contains only regions with a low excess oxygen content and stoichiometric regions. For this reason, further annealing (and, correspondingly, a decrease of δ) can only decrease volume of the oxygen-enriched phase.

The observed increase in the magnetic moment with further heat treatment was caused by a different mechanism. It is known that when excess oxygen is introduced, carriers appear in the copper–oxygen planes, which destroys magnetic order. In the course of heat treatment the number of carriers decreases, and, as a result of localization, this decrease is more rapid than that of the oxygen index.[4] The result is that the magnetic moment increases systematically at the transition from stage *3* to stage *4*. Furthermore, high-temperature heat treatment at stage *4* apparently results in partial annealing of various defects, which causes the coercive force to decrease (Fig. 3). We note that in Ref. 8 (where hysteresis in the magnetization of undoped La_2CuO_4 was observed in high fields) the width of the loop was also observed to decrease after heat treatment at a high temperature. Finally, as one can see from Figs. 1 and 2, prolonged annealing at 500 °C, which completely eliminates the excess oxygen, returns the sample into the state *5*, which is similar to the initial state *1*. Therefore there exists an optimal excess oxygen concentration for ferromagnetism.

The large difference in the values of the remanent magnetization with the magnetizing field parallel and perpendicular to the c axis allows us to conclude that ferromagnetic ordering occurs along the c axis of the crystal. It is known that the formation of such a ferromagnetically ordered phase in La_2CuO_4 in high fields is due to the fact that in the Néel state the copper spins do not lie precisely in the Cu–O plane but rather are tilted out of the plane by a small angle. Therefore each Cu–O plane possesses a ferromagnetic moment but the total moment with a zero external field equals zero, since the antiferromagnetic interplanar interaction forces the spins located in neighboring planes to tilt in opposite directions from one another. When the external field is higher than some critical value, these total moments in alternate planes become reoriented in a ferromagnetic manner.[1] The presence of excess oxygen in a position between the Cu–O planes leads to such ferromagnetic ordering, which starts already at zero field (the hysteresis loop is centered at zero field). In general, various disruptions of the stoichiometry apparently are capable of inducing ferromagnetic order. The character of the disruption can be different. For example, in Ref. 9 ferromagnetism was observed in $La_{2-x}Nd_xCuO_4$. In contrast to excess oxygen, which is intercalated in the interplanar space, the neodymium ions replace lanthanum. Furthermore, behavior of the ferromagnetic type is observed in La_2CuO_4 samples which are subjected to neutron irradiation,[10] which produces defects in the crystal lattice. Therefore despite the different character of the disruptions these changes in the initial structure apparently all result in a change in the magnetic interaction between the Cu–O planes.

We thank G. G. Khaliullin for a helpful discussion.

This work was supported by the Scientific Council on ''Superconductivity'' of the State Science and Technical Program ''Current topics in condensed-matter physics,'' Project No. 194045.

[a]e-mail: nadir@dionis.kfti.kcn.ru

---

[1] T. Thio, T. R. Thurston, and N. W. Preyer, Phys. Rev. B **38**, 905 (1988).
[2] A. A. Zakharov, A. A. Nikonov, and O. E. Parfenov, JETP Lett. **64**, 162 (1996).
[3] A. Wattiax, J. C. Park, J-C. Greiner *et al.*, Acad. Sci. Ser. B **310,** 1047 (1990).
[4] E. L. Vavilova, N. N. Garifyanov, E. F. Kukovitsky *et al.*, Physica C **264**, 74 (1996).
[5] D. C. Harris and T. R. Vanderah, Inorg. Chem. **28**, 1198 (1989).
[6] N. E. Alekseevskii, N. E. Mitin, A. V. Nihankovskii *et al.*, J. Low Temp. Phys. **77**, 87 (1989).
[7] J. D. Jorgensen, B. Dabrovskii, Shiyou Pei *et al.*, Phys. Rev. B **38**, 1137 (1988).
[8] A. N. Bazhan, V. N. Bevz, M. B. Kosmyna *et al.*,Sverkhprovod. (KIAE) **3,** 31 (1990) [Superconductivity **3**, 941 (1990)].
[9] M. Crawford, R. L. Harlow *et al.*, Phys. Rev. B **47**, 11623 (1993).
[10] M. Baran, H. Szymczak, and R. Szymczak, Europhys. Lett. **32**, 79 (1995).

Translated by M. E. Alferieff

Atomic structure and microtopography of interfaces between crystalline and amorphous phasees in tungsten

A. S. Bakaĭ, I. M. Mikhaĭlovskiĭ, E. V. Sadanov, O. A. Velikodnaya, and T. I. Mazilova
Kharkov Physicotechnical Institute National Science Center, 310108 Kharkov, Ukraine

(Submitted 1 September 1997)
Pis'ma Zh. Éksp. Teor. Fiz. **66**, No. 7, 475–480 (10 October 1997)

The morphology of the interface between crystalline and amorphous phases in tungsten is investigated at the atomic level. Interfacial incoherence and a high degree of localization of imperfections are found. It is found that in the region near the interface the close-packed crystallographic planes are in register with the paraplanes. © *1997 American Institute of Physics.* [S0021-3640(97)00619-1]

PACS numbers: 68.35.Ct, 61.16.Fk

The special physical properties of nanocrystalline and crystalline–amorphous materials are due to the presence of extended interfaces in them. Specifically, the processes occurring at an interface between the crystalline and amorphous phases determine to a large degree the crystallization of the amorphous phase (see, for example, Refs. 1 and 2). However, such interfaces remain virtually unstudied because of specific difficulties of investigating disordered systems by high-resolution diffraction methods. In the present work we obtained experimental information on an atomic scale about the atomic structure and microtopography of interfaces between amorphous and crystalline phases in a crystalline–amorphous material.

The experiments were performed in a two-chamber field ion microscope with the samples cooled to liquid-hydrogen temperature. Helium at pressures of 10^{-2}–10^{-3} Pa was used as the imaging gas. The pressure of the active residual gases in the working chamber of the microscope was equal to 10^{-5}–10^{-7} Pa. After the acicular tungsten samples were placed into the microscope, their surface was polished by low-temperature field evaporation[3] until an atomically smooth hemispherical tip with a radius of curvature in the range 15–50 nm was obtained. Amorphization of the microcrystals was performed directly in the microscope by ultrafast quenching from the liquid phase.[4] Voltage pulses with amplitudes of 5–30 kV were applied to the acicular samples for local fusing of the tips. The duration of the pulses at half amplitude was equal to 40–50 ns and the fall time of the voltage was equal to 10 ns. The amplitude of the voltage depended on the radius of curvature in a manner such that the electric field strength was 15–25% higher than the threshold strength for low-temperature (nonactivational) evaporation: 5.7×10^8 V/cm. The ponderomotive forces arising in the process were much stronger than the theoretical maximum strength of the material.[3] Observations in the field microscope–mass analyzer[5] showed that the destruction of the sample tips initiates explosive evaporation in the form of doubly to quadruply ionized atoms. At an ion current density of $(2-5)\times10^6$ A/cm^2 at the sample tips, vacuum breakdown occurs. As a result, the tip point fuses and the radius

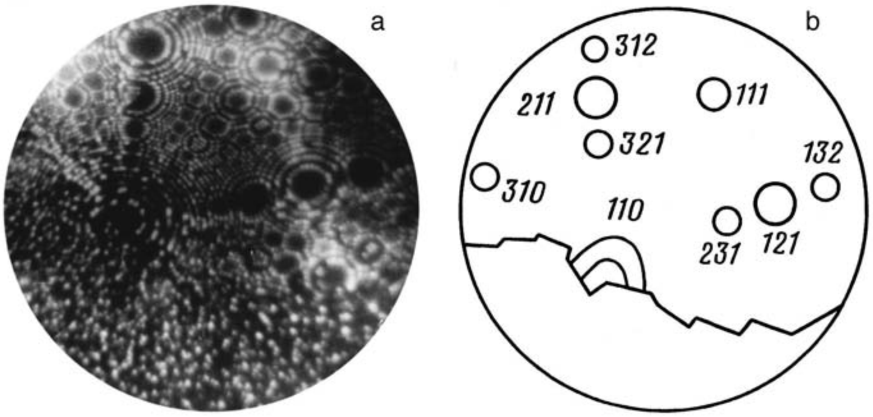

FIG. 1. Field ion microscope image (a) and stereo projection (b) of a crystalline–amorphous tungsten sample.

of the tip increases by an order of magnitude or more. Estimates of the cooling time for the point of a conical tip show that on account of the appearance of large temperature gradients, this time is not much greater than the fall time of the voltage pulse. Correspondingly, the cooling rate can reach values of 10^{10}–10^{11} deg/s, which is much higher than the quench rate during the stabilization of the amorphous state in macroscopic volumes.[6] Vacuum breakdown is accompanied by intense interelectrode mass transfer associated with the formation of cathodic and anodic flares.[7] This results in microalloying of the surface layers, which also promotes stabilization of the amorphous state.

Pulsed fusion and ultrafast quenching transferred some acicular samples into an amorphous or amorphous–crystalline state. A large fraction of the samples ($>90\%$) retained a crystalline structure. The possibility of observing crystalline and amorphous phases simultaneously permits determining to a high degree of accuracy (2–5%) the magnification in an image. This eliminates the difficulties, discussed in Ref. 8, in the interpretation of field emission images of amorphous metals.

Figure 1 displays an ion-microscope image of the surface of an acicular crystalline–amorphous sample produced by pulsed high-field treatment. The images of the amorphous phase are characterized by the nearly complete absence of regularity in the arrangement of the atoms in the surface layer. In addition, the density of surface atoms that contribute to the formation of the ion-microscope images of amorphous metal–nonmetalloid alloys is also observed to decrease.[8,9]

Analysis of the morphology of the interfaces on a series of micrographs obtained in the process of field evaporation to a depth of the order of 10^2 nm showed that the boundaries at the microscopic level are rough. Microprotrusions 1–5 nm high and 2–15 nm wide are observed (Fig. 1). In a number of samples atomically smooth planar sections surrounded, as a rule, by microscopically rough regions were observed on the interfaces. The area of the atomically smooth islands falls within comparatively wide limits: 10–10^2 nm^2.

The exceedingly small width of the interface is noteworthy. The regularity in the

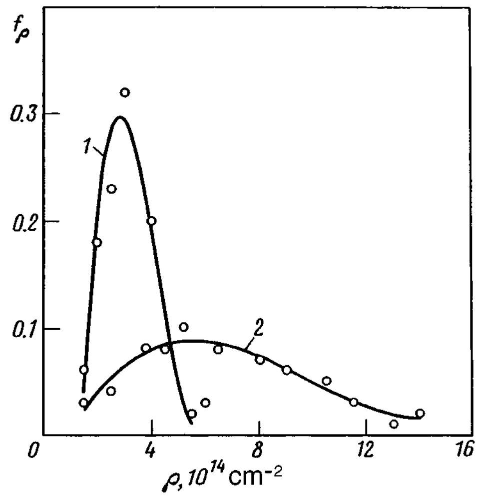

FIG. 2. Distribution of local concentrations of surface atoms in the amorphous (*1*) and crystalline (*2*) phases.

arrangement of the atoms in the crystalline phase remains right up to the interface. The configuration of the concentric atomic steps corresponds to the computer images obtained of ideal single crystals on the basis of a geometric model.[3] This attests to the incoherence of interface between the crystalline and amorphous phasees. In the case of coherent mating one would expect the existence of a transition layer and the presence of local distortions of the crystal lattice in the region near the interface. We note that distortions of atomic paraplanes in regions of coherent mating with an amorphous environment have been observed both by means of high-resolution electron microscopy[10] and a low-temperature field ion microscopy.[1,11]

The displacements of the atoms were determined according to the local deformation at the boundary of the concentric atomic steps on close-packed atomic faces by means of indirect magnification.[12] Inelastic displacements up to 5×10^{-2} nm in magnitude were observed only near the nucleus of an interface up to one lattice parameter wide. The arrangement of the near-interface poles and atomic steps of the close-packed faces which is characteristic for a bcc lattice remained unchanged.

A quantitative determination of the interfacial width can made by employing the change occurring in the thickness of the imaged surface layer (ion image) on amorphization. Figure 2 shows the local concentration distributions of the surface atoms in the amorphous (curve *1*) and crystalline (curve *2*) phases. The ratio of the half-widths of the distributions for the crystalline and amorphous phases equals 2.8. The average density of the imaged atoms in the crystalline state is 2.2 times higher than that in the amorphous state. This confirms the conclusion drawn in Ref. 8 that in the amorphous phase the surface atomic layer participating in the formation of the field emission image is comparatively thin. Figure 3 displays the average surface density of atoms as a function of the distance *d* to the interface. The negative values refer to the crystalline phase. A practically jumplike change in the surface density is observed on a section of width 0.3–0.4

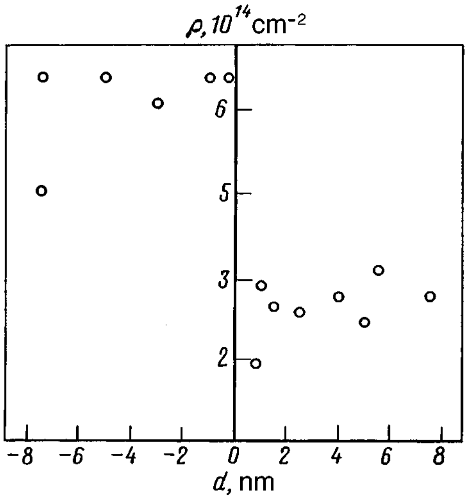

FIG. 3. Surface density of imaged atoms as a function of the distance d from the interface. Negative values of d correspond to the crystalline phase.

nm. Therefore the width of the interface between the crystalline and amorphous phases can be taken as equal to one lattice parameter, which is much smaller than the width of the intercrystallite boundaries.[13]

In the cases when crystallographic planes with low Miller indices intersected the interface at an angle close to 90°, microregions where atoms formed close-packed planar groups — paraplanes (Fig. 4) — were observed in the near-interface layer of the amor-

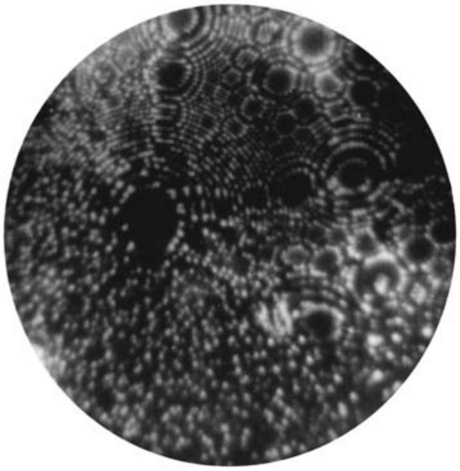

FIG. 4. A region of orientational matching between the crystallographic (110) plane and the corresponding paraplane in the amorphous phase.

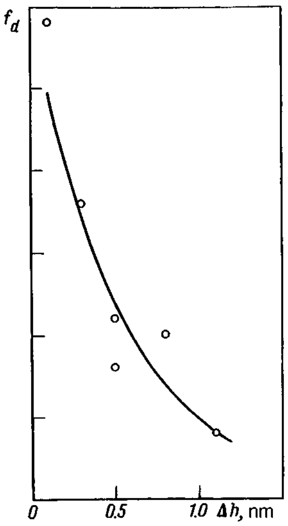

FIG. 5. Distribution of the subatomic displacements Δh in close-packed planes near an interface.

phous phase. Similar paraplanes have been observed before by electron[10] and field ion[11] microscopy in three-dimensional regions of metallic glasses. In contrast to the planes in the crystalline phase, the paraplanes were characterized by the presence of small atomic displacements. In accordance with the geometric model of the formation of field ion images,[3,14] the presence of an image of the atoms inside a semicircular step in the amorphous phase attests to a displacement of the atoms in a direction normal to the paraplane. The magnitude Δh of the displacement is proportional to the difference of the distances between the atom being analyzed and the pole of the paraplane and the radius r of the step: $\Delta h = r\Delta r/R$, where R is the radius of curvature of the surface of the sample. The results of calculations of the atomic displacements Δh performed on the basis of an analysis of a series of ion-microscope images are presented in Fig. 5. The displacements Δh can be regarded as a measure of the breakdown in the planarity of the arrangement of the atoms in the paraplanes in the near-interface regions of the amorphous phase.

Field evaporation of the samples usually revealed structural nonuniformities of the interface. Figure 4 displays the ion-microscope image of an interfacial section where a [110] pole has emerged. The semicircular atomic step on the (110) face of the crystal is in register with a paraplane in the amorphous phase at the interface. The fact that no kinks of the atomic steps at the interface were observed under the ion microscope indicates that the degree of orientational matching between the coherently mated crystallographic planes and paraplanes is high. Estimates made by the indirect magnification method show that the relative displacement of the planes and paraplanes does not exceed 2×10^{-2} nm. Alternation of the non-mated sections and regions of orientational matching of the close-packed planes and paraplanes (Fig. 4) ordinarily continued as the the sample was field evaporated to a depth of 10^2–10^4 nm.

In summary, in the present work it was established by means of the high-resolution methods of field ion microscopy that the interface between the amorphous and crystalline phases is incoherent and atomically sharp. It was found that the interfaces are structurally and microtopographically nonuniform. Non-mated sections of the interfaces alternate with regions where there is an orientational matching of the close-packed crystallographic planes and paraplanes in the amorphous phase.

This work was supported in part by the Ukrainian State Committee on Problems of Science and Technologies: Funds for Fundamental Research (Project 2.3/933) and State Scientific and Technical Programs (Projects 5.42.06/040 and 7.02.05/093).

[1] A. S. Bakai in *Glassy Metals III*, edited by H. Beck and H.-J. Guntherodt, Springer, Heidelberg, 1994.

[2] X. Y. Tong, B. Z. Ding, H. G. Giang *et al.*, J. Appl. Phys. **75**, 654 (1994).

[3] E. W. Müller and T. T. Tsong, *Field Ion Microscopy, Field Ionization and Field Evaporation*, Pergamon Press, 1978 [Russian translation, Nauka, Moscow, 1980].

[4] S. É. Zaĭtsev and A. L. Suvorov, Preprint No. 154, Institute of Theoretical and Experimental Physics, Central Scientific-Research Institute of Atomic Reference Data, Moscow, 1987.

[5] I. M. Mikhaĭlovskiĭ, V. A. Ksenofontov, E. V. Sadanov *et al.*, JETP Lett. **57**, 40 (1993).

[6] K. Suzuki, H. Fujimori, and K. Hasimoto, *Amorphous Metals* [Russian translation], Metallurgiya, Moscow, 1987.

[7] G. A. Mesyats and D. I. Proskurovskiĭ, *Pulsed Electric Charge in Vaccum* [in Russian], Nauka, Moscow, 1984.

[8] L. Nordentoft, Philos. Mag. B **52**, L21 (1985).

[9] A. S. Bakai, V. B. Kulko, I. M. Mikhailovskij *et al.*, J. Non-Cryst. Solids **182**, 315 (1995).

[10] Y. Hirotsu, M. Uehaza, and Ueno, J. Appl. Phys. **59**, 3081 (1986).

[11] I. M. Mikhaĭlovskiĭ, L. I. Fedorov, and P. Ya. Poltinin, Fiz. Met. Metalloved. **76**, 123 (1993).

[12] I. M. Mikhaĭlovskiĭ, Fiz. Tverd. Tela (Leningrad) **24**, 3210 (1982) [Sov. Phys. Solid State **24**, 1822 (1982)].

[13] A. N. Orlov, V. N. Perevezentsev, and V. V. Rybin, *Grain Boundaries in Metals* [in Russian], Metallurgiya, Moscow, 1980.

[14] M. K. Miller and G. D. W. Smith, *Atom Probe Microanalysis: Principles and Applications to Materials Problems*, Oak Ridge National Lab., 1987 [Russian translation, Mir, Moscow, 1993].

Translated by M. E. Alferieff

Size effects in the melting and crystallization temperatures of copper chloride nanocrystals in glass

P. M. Valov and V. I. Leĭman
State Technological University of Phytopolymers, 192095 St. Petersburg, Russia

(Submitted 14 July 1997; resubmitted 4 September 1997)
Pis'ma Zh. Éksp. Teor. Fiz. **66**, No. 7, 481–486 (10 October 1997)

The size dependence of the crystallization temperature T_c and melting temperature T_m of copper chloride nanocrystals in glasses is studied in the size range R_a from 1 to 30 nm. Jumps are found in the temperature dependence of T_c at $R_a = 13$ nm and $R_a = 1.8$ nm, a jump is found in the temperature dependence of T_m at $R_a = 2.2$ nm, and the supercooling of the melt is found to vanish in the case of crystallization at $R_a \leqslant 1.4$ nm. It is conjectured that the jump in T_c with large R_a occurs for a nanocrystal radius equal to that of a crystalline nucleus in the melt, and the jumps in T_c and T_m for smaller values of R_a are due to a change in the shape (faceting) of the nanocrystals. © *1997 American Institute of Physics.* [S0021-3640(97)00719-6]

PACS numbers: 64.70.Dv, 61.43.Fs

Supercooling of a crystallizing melt is observed in both macrosystems[1] and ultradisperse phases (UDPs).[2] In the case of UDPs, supercooling of the melt on crystallization, $\Delta T = T_m - T_c$, where T_m is the melting and T_c the crystallization temperature, almost always occurs.[2] The supercooling of the melt is due to the work of formation of a surface of the crystalline nucleus in the melt medium. According to Gibbs, the work of formation of a nucleus equals[3]

$$W = \frac{1}{3}\sigma_{cm} S, \tag{1}$$

where σ_{cm} is the interphase surface tension at the crystal–melt interface (specific surface energy) and S is the surface area of a crystalline nucleus formed in the melt. The smallest stable particle of a solid phase in the melt is called a critical nucleus. According to theory, σ approaches zero as $R \rightarrow 0$ (Refs. 3 and 4) and ΔT will decrease correspondingly. However, experimental data[2,5] show that ΔT approaches zero at some finite particle size.

At least two other effects that can destroy the monotonicity of the size dependence of T_c and T_m can also be expected. If the mass of the UDP is equal to or less than the required mass of a critical nucleus, then the crystal is created with a free surface which corresponds to a larger surface tension $\sigma_c > \sigma_{cm}$ and a larger work of formation of the crystal, which can result in a jump in the magnitude of the supercooling of the UDP melt. As a result of this, a jump can appear in the dependence $T_c = f(R)$ at $R_a = R_{cr}$, where R_{cr} is the radius of a critical nucleus in the UDP melt. Furthermore, the equilibrium structure of small particles (clusters) can change.[6] This can also give rise to characteristic features in the size dependences of T_c and T_m.

The present work is devoted to a study of the size dependences of the melting and crystallization temperatures of UDP particles for the example of CuCl nanocrystals distributed in a glass matrix. The properties of the copper chloride nanocrystals obtained in glass are quite stable, and the excitonic absorption of CuCl nanocrystals is reliably detected (for the $Z_{1,2}$ exciton) right up to the melting temperature. It is important that at some energy E_0 in the region of the long-wavelength dropoff of the excitonic band the light absorption coefficient $K(E_0,T)$ is temperature-independent.[7] On the basis of the Urbach relation[8] and Toyozawa's work,[9] the energy E_0 can be interpreted as the ground state of a $Z_{1,2}$ exciton, and the absorption at E_0 can be interpreted as a direct optical transition into this state (without phonon participation). The energy E_0 and the exciton–phonon absorption bands $Z_{1,2}$ and Z_3 shift to higher energies as the CuCl nanocrystals decrease in size.[7] When the nanocrystals melt, the absorption $K(E_0,T)$ is observed to drop off as a result of the vanishing of the crystalline structure and, correspondingly, the vanishing of the excitonic states. When the UDP melt is cooled, at some temperature $K(E_0,T)$ is observed to increase up to the previous value as a result of crystallization of the UDP. The melting and crystallization temperature of CuCl nanocrystals were determined from the change in the curves $K(E_0,T)$ near the corresponding phase transitions.[5]

Glass samples in the form of plates with a continuous distribution of the average radius of CuCl nanocrystals were obtained by the method of Ref. 5. The third stage of growth of the UDP[10,11] occurs under these conditions, and in accordance with Ref. 12 the average radius in the ensemble of UDP particles is determined by the treatment time t and temperature T_a:

$$R_a^3=\frac{4}{9}\alpha t D_0 \exp(-U/kT_a), \tag{2}$$

where α is the UDP–glass surface tension, D_0 and U are, respectively, the diffusion coefficient and activation energy of formation of the new phase, and k is Boltzmann's constant. The UDP forms in the glass in the liquid state, and when the sample is cooled the UDP crystallizes and copper chloride nanocrystals precipitate. The absorption spectra and the functions $K(E_0,T)$ were measured with a computer-controlled spectroscopic system. The finished samples were plates $14\times 0.6\times$ mm in cross section and 60 mm long. Measurements on each section of the glass were performed with an energy-tunable light probe with a width of 0.1 mm and a height of 2 mm. The energy E_0 for each section of the sample (with the corresponding size R_a of the CuCl crystals) was determined by the method of Refs. 5 and 7.

The typical curves of $K(E_0,T)$ near melting–crystallization phase transitions are presented in Fig. 1 (curves *1*,*2*). Absorption actually does not change when the sample is heated from room temperature up to 300 °C (curve *1*), while from 325 °C up to the point *A* the absorption falls off as a result of melting of CuCl nanocrystals and the entire UDP. When the UDP melt is cooled from the point *A*, the absorption of the melt decreases somewhat, and near 200 °C, at the point *B*, absorption starts to grow rapidly as a result of crystallization of UDP and precipitation of CuCl crystals. Absorption does not return to its previous level (the segment *C*–*D*) because of the large number of ''frozen'' defects

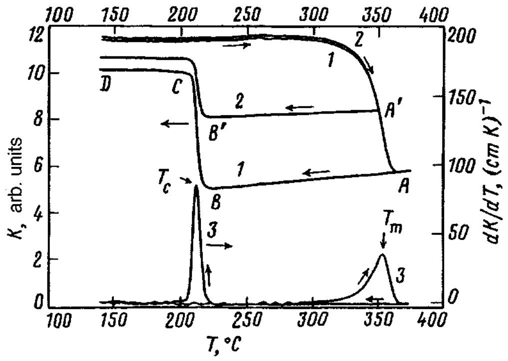

FIG. 1. Absorption coefficient $K(E_0,T)$ of CuCl nanocrystals (curves *1,2* — partial melting) and its first derivative dK/dT (curve *3*) as a function of temperature. $R_a=10.6$ nm, $E_0=3.242$ eV; T_m and T_c are the melting and crystallization temperatures of CuCl particles with $R=R_a$.

at the time that the CuCl crystallizes. When the sample is held in a temperature range somewhat below melting onset (for example, near 275 °C) absorption is restored to the initial level and the experiment is fully repeatable (curve *2*). Stopping the temperature at the moment of melting (point A' on curve *2*) or at the moment of crystallization stops the phase transition. The reverse course of the $K(E_0,T)$ curve in this case already follows a different level (curve *2*, segment $A'-B'$). Hence it follows that the course of the $K(E_0,T)$ curve at the moment of the phase transition is determined mainly by the variance of the melting and crystallization temperatures in an ensemble of CuCl particles with a size distribution.[a)]

The first derivative of $K(E_0,T)$ is displayed in Fig. 1 (curve *3*). The peaks near 350 and 250 °C show the phase-transition intensity dK/dT on melting and crystallization, respectively. The width of the corresponding peak reflects the variance of $T_c=f(R)$ or $T_m=f(R)$ in an ensemble of CuCl particles, and the maximum of the peak determines the temperature T_m and T_c at the maximum of the distribution with $R=R_a$.

Figure 2a displays the size dependences of the melting temperature T_m (curve *1*, points) and the crystallization temperature T_c (curves *2* and *3*, points), found in this manner, for CuCl nanocrystals in glass as a function of the average size R_a. Figure 2b shows the size dependence of the position of the maximum of the excitonic absorption band $Z_{1,2}=f(R_a)$ of CuCl nanocrystals at 300 K (curve *1*) and the position of the excitonic ground state $E_0=f(R_a)$ (curve *2*) corresponding to the photon energy in the measurement of the $K(E_0,T)$ curve. The values of R_a for each measured region of the sample were calculated according to Eq. (2) taking account of the treatment time and temperature T_a ($t=3$ h, $T_a=500-720$ °C).[b)]

The absolute size scale for nanocrystals with $R_a>2$ nm was referenced by the SAXRS method, whose error does not exceed 1%. The accuracy in determining the CuCl particle radii less than 2 nm by the SAXRS method decreases sharply on account of an increase in the contribution of nonuniformities of the glass matrix to the scattering of the

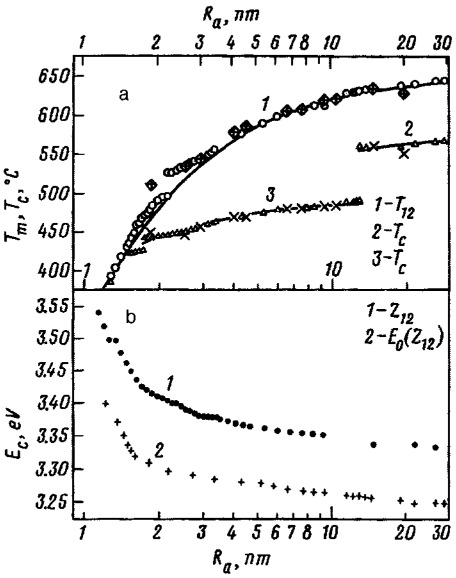

FIG. 2. Melting temperature $T_m(R_a)$ and crystallization temperature $T_c(R_a)$ (a) and ground state E_0 and position of the absorption band of a $Z_{1,2}$ exciton (b) versus the average radius of a CuCl particle in glass. a) Melting temperature T_m (curve *1*, points — experiment) and crystallization temperature T_c (curves *2*,*3*, points — experiment) of CuCl nanocrystals; large symbols — control samples with known R_a: ◇ — T_m, × — T_c; the theoretical curves for T_m (solid curve *1*) and T_c (solid curves *2*,*3*) were taken from Ref. 5; b) Position of the absorption band at 300 K (curve *1*) and the ground state E_0 (curve *2*) for the $Z_{1,2}$ exciton; R_a was determined from T_a for each section of the sample using Eq. (2) at $t=1.08\times10^4$ s, $A\cdot D_0=1.39\times10^{15}$ nm^3/s, and $U=47\times10^{-20}$ J.

x-rays. For this reason, the sizes obtained for CuCl nanocrystals with R_a less than 2 nm must be treated as rough estimates.

The general trends in the behavior of T_m and T_c were successfully described[5] on the basis of the theoretical dependence for T_m and the empirical dependence for σ. These dependences are displayed in Fig. 2a (solid curves *1*–*3*).

The half-width of the particle size distribution was determined according to the experimental size dependence $T_a(R)$ (Fig. 2, curve *3*) and the curves dK/dT (Fig. 1, curve *3*) for nanocrystals with $R_a=10.6$ nm. It equals 7.5 nm. The experimental width is 1.6 times greater than the theoretical width calculated according to the Livshitz–Slezov theory.[12] For ensembles of smaller nanocrystals, for example, for $R_a=2.7$ nm, the experimental half-width of the distribution equals 0.8 nm and the theoretical value equals 1 nm.

A discontinuity is present in the experimental curve $T_m(R_a)$ at $R_a=2.2$ nm (see curve *1*, points). Two more discontinuities are seen in the experimental curve $T_c(R_a)$ at $R_a=13$ nm and $R_a=1.8$ nm. For small sizes, $R_a\leqslant1.4$ nm, the curves $T_c(R_a)$ and $T_m(R_a)$ merge. This is due to the vanishing of the supercooling of the UDP melt on crystallization.

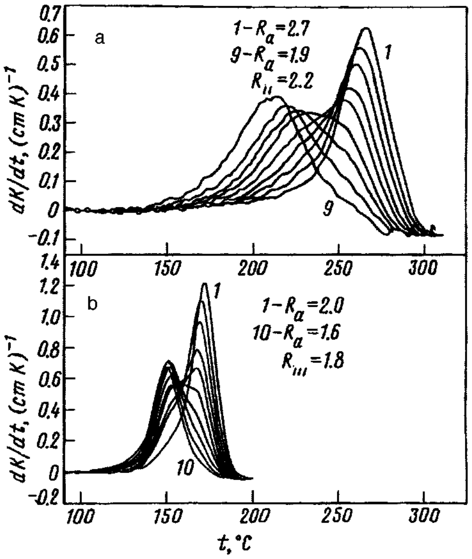

FIG. 3. Curves of the phase-transition intensity $dK(E_0,T)/dT$ for CuCl nanocrystals in glass on melting (a) and crystallization (b) near the corresponding jumps in T_m and T_c. The nanocrystals decreased in size: a) from 2.7 nm (*1*) to 1.9 nm (*9*) and b) from 2.0 nm (*1*) to 1.6 nm (*10*). At $R_{II}=2.2$ nm — jump in the parameter T_m; at $R_{III}=1.8$ nm — jump in the parameter T_c.

Calibration experiments showed that the form of the curves $T_m(R_a)$ and $T_c(R_a)$ and the location of the jumps noted in Fig. 2a are not related with any features of the temperature properties of the glass matrix.[c)] For this reason, the curves presented in Fig. 2 most likely are explained by the size of the CuCl particles.

The jump I (by 55 K in T_c at a 13 nm size — the discontinuity between curves *2* and *3* in Fig. 2a) is, we believe, related to the size of the critical nucleus R_{cr} of the CuCl crystal formed in the UDP melt.[5] The supercooling ΔT of the melt and, accordingly, T_c depend on whether or not the UDP mass is greater or less than that required for a critical CuCl nucleus. Correspondingly, the initial crystal is created inside the melt or with a free surface, and then the work of formation of the surface is different, and therefore ΔT is different.

The presence of the jump II (in the size dependence $T_m(R_a)$ at $R_{II}=2.2$ nm, Fig. 2a, curve *1*) is clearly seen in the size variations of the curves of the melting intensity dK/dT (Fig. 3a). As R_a decreases from 2.7 nm (curve *1*) to 1.9 nm (curve *9*), the number of particles gradually becomes redistributed from the size range $R>R_{II}=2.2$ nm, where the melting point is not lower than 253 °C, into the size range $R<R_{II}$, where the melting temperature is 25 K lower. The temperatures T_m — the maximum of the phase transition intensity for nanocrystals with sizes somewhat greater than R_{II} and, correspondingly, less than R_{II} — were found by decomposing the curves *4–9*. These data are presented in Fig. 2a near the jump in T_m.

For the jump III (in T_c, Fig. 2a, curve *3* at $R_{III}=1.8$ nm) the analogous redistribution of the curves dK/dT with a discontinuity of the average crystallization temperature T_c is shown in Fig. 3b for average sizes R_a ranging from 2.0 nm (curve *1*) to 1.6 nm (curve *10*). The average size equals $R_{\mathrm{III}} = 1.8$ nm (curve *6*), for which half of the particle ensemble has a crystallization temperature T_c no lower than 170 °C and the other half has a crystallization temperature no higher than 155 °C.

The last jumps could both be due to the change in the equilibrium crystal shape. In accordance with the theory,[3,4] the specific surface energy σ of a particle decreases with the particle size. However, Rusanov's calculations[4] show that for some small sizes σ can start to increase on account of an increase of the relative contribution of edges to the surface energy. In this connection, it is energetically more advantageous for the faceting of a crystal to change so that the free energy of the crystal does not increase on account of an increase in the surface energy. As experiments show, in the case of CuCl nanocrystals the crystal shape changes without a substantial change in the crystalline structure of the crystal, since in this size range there is no jump in the size dependence of the position of the $Z_{1,2}$ exciton (Fig. 2b, curves *1*,*2*).

The small shift to smaller sizes ($R_{\mathrm{III}} = 1.8$ nm) of the jump in T_c relative to the jump in T_m ($R_{\mathrm{II}} = 2.2$ nm) could possibly be explained by the lower crystallization temperature, as a result of which a change in the equilibrium faceting becomes advantageous at smaller sizes.

One other important size effect should be noted in Fig. 2 — merging of the curves *1* and *3* (Fig. 2a) at CuCl nanocrystal sizes less than $R_\delta = 1.4$ nm. The crystallization temperature $T_c(R)$ follows the curve $T_m(R)$ and therefore the supercooling of the melt vanishes $\Delta T = 0$. Such an effect was predicted in Ref. 1. This effect is explained in Ref. 5 by the vanishing of the surface energy for particles whose size is close to the thickness of the surface layer of the crystal. The clear manifestation of excitonic absorption and the presence of the melting–crystallization phase transition attest to the crystalline structure of such particles. For these particles the size shift of the energy states of the $Z_{1,2}$ exciton increases sharply (Fig. 2b, curves *1* and *2*).

In summary, Gibbs' remark about the possibility of having physical heterogeneity (UDP) with zero surface energy [Ref. 3, p. 255] has been completely confirmed. As we have seen, such a heterogeneity is a special type of crystal whose main property is the absence of surface energy. This could be due to a rapid exchange between the electronic subsystems of the atoms in the bulk and at the surface. If this is an activational exchange, it is possible that it can be frozen at low temperatures. In this case, investigation of such crystalline formations at low temperatures is very promising. These crystals can be rightfully called quantum dots or superatoms,[10] since in them there is no difference between the surface atoms and atoms of the bulk.

We are especially grateful to V. V. Golubkov for measuring R_a of the control samples by the SAXRS method. This work was sponsored by the Russian Fund for Fundamental Research (Grant No. 96-02-16966).

---

[a] The stopping of the phase transition is explained by the nonmelting or noncrystallization, respectively, of that part of the ensemble of CuCl particles for which the temperature is higher (on melting) or lower (on crystallization) than the stopping temperature.

[b] The computational parameters were chosen empirically on the basis of the data of Ref. 11. Control samples,

on which the size of the nanocrystals was determined by small-angle x-ray scattering (SAXRS) method and the parameters T_m and T_c were measured (large squares and crosses on the corresponding curves *1–3*), were prepared at certain randomly selected treatment temperatures. The results confirmed the correctness of the calculation of R_a from Eq. (2). In the size range 1–3 nm Eq. (2) most likely somewhat overestimates the sizes because the UDP growth mechanism passes into the second stage.[12]

[c)] When the heat treatment time of the control sample increased or decreased by a factor of 10, the dependences $T_m(R_a)$ and $T_c(R_a)$ and the region of the jumps shifted to lower or higher treatment temperatures, respectively, by more than 15 °C.

---

[1] V. P. Skripov and V. P. Kaverda, *Spontaneous Crystallization of Supercooled Melts* [in Russian], Nauka, Moscow, 1984.

[2] G. L. Zhdanov, Izv. Akad. Nauk SSSR, Ser. Fiz. **41**, 1004 (1977).

[3] *The Collected Works of J. Willard Gibbs*, Ph. D., LL. D., Longmans, Green and Co., New York, 1928, Vol. 1, p. 434 [Russian translation, Goskhimizdat, Moscow, 1950].

[4] I. A. Rusanov, *Phase Equilibria and Surface Phenomena* [in Russian], Khimiya, Leningrad, 1967.

[5] P. M. Valov, L. V. Gracheva, and V. I. Leĭman, Fiz. Khim. Stekla **23**, 187 (1997).

[6] Yu. I. Petrov, *Clusters and Small Particles* [in Russian], Nauka, Moscow, 1986.

[7] P. M. Valov, L. V. Gracheva, V. I. Leĭman, and T. A. Negovorova, Fiz. Tverd. Tela (St. Petersburg) **36**, 1743 (1994) [Phys. Solid State **36**, 954 (1994)].

[8] M. V. Kurik, Phys. Status Solidi A **8**, 9 (1971).

[9] M. Schreiber and Y. Toyozawa, J. Phys. Soc. Jpn. **51**, 1528 (1982).

[10] S. V. Gaponenko, Fiz. Tekh. Poluprovodn. **30**, 577 (1996) [Semiconductors **30**, 315 (1996)].

[11] V. V. Golubkov, A. I. Ekimov, A. A. Onushchenko, and V. A. Tsekhomskiĭ, Fiz. Khim. Stekla **7**, 397 (1981).

[12] I. M. Livshitz and V. V. Slezov, Zh. Éksp. Teor. Fiz. **35**, 479 (1958) [Sov. Phys. JETP **8**, 331 (1959)].

Translated by M. E. Alferieff

Co/Pd and Co/Pd/CoNi multilayer films: Determination of the sign and magnitude of the exchange interaction of ferromagnetic layers separated by palladium layers

R. S. Iskhakov,[a)] Zh. M. Moroz, L. A. Chekanova, and N. A. Shepeta
L. V. Kirenskiĭ Institute of Physics, Siberian Branch of the Russian Academy, of Sciences, 660036 Krasnoyarsk, Russia

E. E. Shalygina
M. V. Lomonosov Moscow State University, 119899 Moscow, Russia

(Submitted 16 July 1997; resubmitted 4 September 1997)
Pis'ma Zh. Éksp. Teor. Fiz. **66**, No. 7, 487–491 (10 October 1997)

It is found that the exchange interaction of Co (5 nm) ferromagnetic layers via Pd in Co/Pd multilayer films and of Co (5 nm) and CoNi (5 nm) layers via the same nonmagnetic metal in Co/Pd/CoNi films can be both ferro- and antiferromagnetic. The period of the AF–F–AF oscillations is of the order of 0.8 nm, and the amplitude of the oscillations decays as a power-law function $\sim d_{\mathrm{Pd}}^{-2}$. © *1997 American Institute of Physics.* [S0021-3640(97)00819-0]

PACS numbers: 75.30.Et, 75.70.Cn

The oscillatory exchange interaction between ferromagnetic layers via a conducting nonmagnetic-metal interlayer is one of the few quantum effects established experimentally in the last few years. There is a large body of theoretical works, but in many cases the mechanisms studied in them do not give a satisfactory explanation of the observed effects. This means that more multilayer objects in which ferromagnetic and antiferromagnetic ordering of the individual layers are realized must be studied. Such objects include Co/Cu, Co/Ru, and Co/Au multilayer films.[1–3] At present there are no experimental data on the oscillations of the exchange interaction between the Co layers for Co/Pd and Co/Pt multilayer films.[4] We shall show that the Co/Pd multilayer system should be added to this list.

Our objective in the present work is to determine the sign and magnitude of the exchange interaction of Co layers via the Pd layer in Co/Pd multilayer films and the dependence of this characteristic on the thickness of the nonmagnetic interlayer.

The Co/Pd multilayer films were obtained by chemical deposition of salts of these metals from an aqueous solution onto a glass substrate. The samples consisted of three pairs of Co/Pd layers with lattice constant $d_{\mathrm{Co}}=5$ nm and Pd layer thickness ranging from 0.5 to 4 nm. Both metals possessed a fcc structure (a detailed description of the samples is given in Ref. 5).

It is well known that the most reliable way to detect antiferromagnetic ordering is to observe orientational transitions of the spin-flop and spin-flip type. The measured field strength of a spin-flip transition makes it possible to determine experimentally the mag-

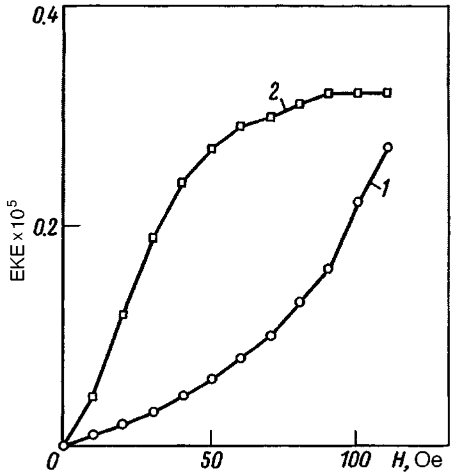

FIG. 1. Typical magnetization curves $\delta(H)\sim M(H)$ of Co(5 nm)/Pd multilayer films: $d_{\mathrm{Pd}}=1.8$ nm (curve *1*) and $d_{\mathrm{Pd}}=1.4$ nm (curve *2*).

nitude of the antiferromagnetic exchange interaction. For this reason, measurements of the magnetization curves for Co/Pd multilayer films were performed on a magnetooptic magnetometer by means of the equatorial Kerr effect. An 80-Hz external ac magnetic field H was applied perpendicular to the plane of incidence of the light and parallel to the surface of the sample. The magnetooptic signal was detected in reflection from a microsection of diameter $D=30$ μm on the surface. The measurements of the local magnetization curves $\delta(H)\sim M(H)$ were performed with a step $D/2$ for a fixed energy of the incident photons.[b)]

The following results were obtained. It was established that the form of the magnetization curves $\delta(H)\sim M(H)$ of Co/Pd films depends only on the thickness of the Pd layer (Fig. 1). Specifically, in-plane magnetization curves which are characteristic for magnetically soft ferromagnetic materials with a saturation field less than 50 Oe were observed for some values of d_{Pd}, while for other values of d_{Pd} the magnetization of the Co/Pd multilayer films was observed in the same geometry to increase linearly with the external magnetic field all the way up to saturation fields above 100 Oe (see Fig. 1). Thus, the magnetization curves $\delta(H)\sim M(H)$ were characterized by saturation fields $H_s>100$ Oe for $d_{\mathrm{Pd}}=0.7$, 1.8, 2.3, 3.6, and 4 nm and by $H_s<50$ Oe for $d_{\mathrm{Pd}}=1.4$, 2.1, 2.7, and 3 nm.

These results point to ferromagnetic and antiferromagnetic ordering of the Co layers in Co/Pd multilayer films and an oscillatory behavior of the exchange interaction of the Co layers via Pd as a function of the Pd thickness. The period of the AF–F–AF oscillations was established from the characteristic change in the form of the magnetization curve (from a magnetically soft to a magnetically hard ferromagnet). For Co/Pd it was found to be equal to 0.8 nm. Assuming the saturation field of the magnetically hard magnetization curve to be equal to the magnitude of the spin-flip transition field and using the expression $J_E=M_{\mathrm{Co}}d_{\mathrm{Co}}H_s/4$, we obtained for the antiferromagnetic exchange

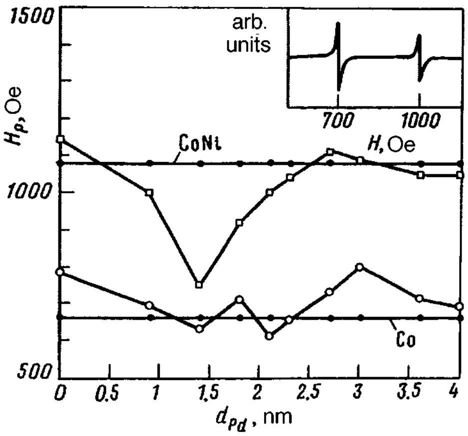

FIG. 2. Resonance fields of the high- and low-field peaks versus the Pd layer thickness for Co/Pd/CoNi multilayer films. The solid lines show the magnitudes of the resonance fields of the Co and CoNi reference films. Inset: Typical form of the ferromagnetic resonance spectrum (at frequency 9.2 GHz) with the [Co(5 nm)/Pd(0.9 nm)/CoNi(5 nm)]·7 film oriented parallel to the external field.

interaction $J_E = 0.6$ Oe/cm^2 in the antiferromagnetic ordered Co layers in Co/Pd multilayer films.

However, in order to compare with the theoretical dependences, it is necessary to have measurements of the experimental dependences $J_E(d_{\mathrm{Pd}})$ in the entire range of thicknesses of the nonmagnetic metal layer. The ferromagnetic exchange interaction $J_E(d_{\mathrm{Pd}})$ cannot be determined from the magnetization curves, so that we used a different experimental procedure, employing the ferromagnetic resonance (FMR). The FMR method was used to measure Co/Pd/CoNi multilayer films with Ni content ~ 20 at.% in an individual layer. The films were also obtained by the method of chemical deposition on glass substrates. The individual fcc Co and fcc CoNi layers possessed a constant thickness of 5 nm; the thickness of the Pd layer varied from 0 to 4 nm. The total thickness of the [Co(5 nm)/Pd(x)/CoNi(5 nm)]·7 films varied from 70 to 130 nm, which made it possible to observe two resonance peaks in the FMR spectrum (at a frequency of 9.2 GHz) with the films oriented parallel to the external field (the typical form of the FMR spectra is displayed in the inset in Fig. 2). Reference samples whose FMR spectra (with parallel orientation) consisted of one resonance peak were prepared; they consisted of single-layer fcc-Co and fcc-CoNi films 200 nm thick. Comparing the FMR spectra of a Co/Pd/CoNi multilayer film with the FMR spectra of the reference samples made it possible to identify the origin of the low-field (due to the Co layers) and high-field (due to the CoNi layers) peaks as well as to record the magnitudes of the resonance fields as a function of the thickness of the Pd layer. Figure 2 displays the resonance fields of the individual ferromagnetic layers versus the thickness of the interlayer in these films. It was assumed that the displacement of the resonance peaks of the CoNi and Co layers in the Co/Pd/CoNi multilayer films from the values of H_r for the reference films is due to the exchange modification of the internal field strength in individual layers.

Expressions for this exchange modification were obtained using a model of a coupled bilayer film system. Since we have used these expressions to determine the magnitudes of the exchange interaction of the Co and CoNi ferromagnetic layers separated by a Pd layer, we shall describe in greater detail the model proposed in Ref. 6. In Ref. 6 a typical system consisting of two ferromagnetic layers interacting with each other via an intermediate nonmagnetic layer was studied. The interaction energy E_{AB} per unit area was written in the form $E_{AB}=-J\mathbf{M}_A\cdot\mathbf{M}_B$, where J is the magnitude of the interaction and the vectors $\mathbf{M}_A$ and $\mathbf{M}_B$ denote the magnetizations in the layers A and B, respectively. The magnetic layers of thickness d_A and d_B are separated by a nonmagnetic layer of thickness d_c. The $x-y$ plane was also the plane of the film. The external magnetic field H, located in the $y-z$ plane, makes an angle α with the normal to the film. The microwave field $h\sim\exp(i\omega t)$ is directed along the x axis. The angles $\theta_{A,B}$ determine the orientation of the magnetization in a Cartesian coordinate system. In the case $d_A=d_B=d_c=d$ and $\alpha=\pi/2$ (H is directed along the y axis), $H_{\mathrm{Keff}\,A}=H_{\mathrm{Keff}\,B}=0$, $\gamma_A=\gamma_B=\gamma$, the total energy for the two-layer interacting system is given by

$$E=[-\mathbf{H}\cdot\mathbf{M}_A+2\pi\mathbf{M}_A^2\cos^2\theta_A]d+[-\mathbf{H}\cdot\mathbf{M}_B+2\pi\mathbf{M}_B^2\cos^2\theta_B]d-J\mathbf{M}_A\cdot\mathbf{M}_B. \quad (1)$$

The dispersion relation determined for this system by solving the Landau–Lifshitz equation in the approximation $H\ll 4\pi M$ can be written in the form

$$(\omega/\gamma)^4-(\omega/\gamma)^2[4\mathbf{H}\cdot(\mathbf{M}_A+\mathbf{M}_B)+8\pi J_E\mathbf{M}_A\cdot\mathbf{M}_B+J_E^2(\mathbf{M}_A+\mathbf{M}_B)^2]+16\pi^2H^2\mathbf{M}_A\cdot\mathbf{M}_B$$
$$+16\pi^2J_E(\mathbf{H}\cdot\mathbf{M}_A)[\mathbf{M}_B\cdot(\mathbf{M}_A+\mathbf{M}_B)]+4\pi J_E^2\mathbf{H}\cdot(\mathbf{M}_A+\mathbf{M}_B)(\mathbf{M}_A^2+\mathbf{M}_B^2)=0, \quad (2)$$

where an effective interaction strength parameter J_E, divided by the thickness of the ferromagnetic layer, is used. For large values of $|J_E|$ the roots of this equation correspond to acoustical and optical oscillations of the magnetization vectors of the ferromagnetic layers A and B, and for $|J_E|\to 0$ this equation has two roots:

$$(\omega^2/\gamma^2)_1=4\pi\mathbf{H}\cdot\mathbf{M}_A+J_E\mathbf{M}_B\cdot\mathbf{M}_A; \quad (\omega^2/\gamma^2)_2=4\pi\mathbf{H}\cdot\mathbf{M}_B+J_E\mathbf{M}_A\cdot\mathbf{M}_B. \quad (3)$$

These equations describe two resonance curves for regions with different magnetizations ($\mathbf{M}_A$ and $\mathbf{M}_B$) and with the corrected internal fields.

We assume that the experimental data presented in Fig. 2 are described by Eqs. (3). This interpretation was chosen as a result of investigations of the resonance fields H_i as a function of the orientation angle α of the external field relative to the normal to the film.

Using the known values of the magnetization of the Co and CoNi layers enabled us to construct theoretical curves of the resonance fields as a function of the magnitude and sign of the exchange interaction. Since similar curves in (H_i,J_E) coordinates were already given in Ref. 6, we do not present them here. Plotting the experimental values of the resonance fields of two modes, obtained from the FMR spectra for Co/Pd/CoNi multilayer films (see Fig. 2), along with the theoretical curves made it possible to determine the function $J_E(d_{\mathrm{Pd}})$. The function $J_E(d_{\mathrm{Pd}})$ computed in this manner is displayed in Fig. 3. One can see that the function $J_E(d_{\mathrm{Pd}})$ is described by the product of an oscillatory function by some function $f(d_{\mathrm{Pd}})$ that decreases with increasing d_{Pd}.

Therefore the Pd-mediated exchange interaction of the ferromagnetic Co and CoNi layers can be both ferro- and antiferromagnetic, and the period of the AF–F–AF oscil-

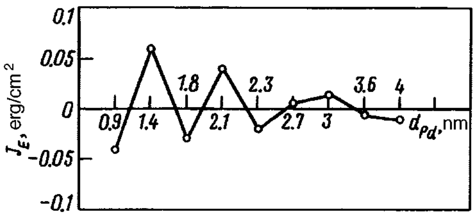

FIG. 3. Computed interlayer exchange interaction constant in Co/Pd/CoNi multilayer films as a function of the Pd layer thickness.

lations agrees with the period determined from the characteristic change in the form of the magnetization curves of the Co/Pd multilayer films (Fig. 1). Moreover, the function $J_E(d_{\mathrm{Pd}})$ calculated from experiment makes it possible to determine (by plotting the experimental quantities in double-logarithmic coordinates) the law of decay of the amplitude of the oscillations with increasing thickness of the Pd layer: It was found that $|J| \sim (d_{\mathrm{Pd}})^{-2}$.

Let us now summarize. It was established that the exchange interaction of the Co layers through the Pd layer in Co/Pd multilayer films is of an oscillatory character and that the amplitude of the oscillations decays as a power-law function $(d_{\mathrm{Pd}})^{-2}$. The small magnitude of this interaction as compared with Co/Cu multilayer films is noteworthy.

[a] e-mail: riuf@iph.krasnoyarsk.su

[b] Kerr effects linear in the magnetization are determined by the expression $\delta_{ki}^{s}=\alpha_{ki}(\omega)M_s$, where the corresponding constants depend only on the wavelength (frequency) of the incident light. Therefore $\delta(H)/\delta_s = M(H)/M_s$, i.e., $\delta(H)\sim M(H)$.

---

[1] A. J. Jin, J. Appl. Phys. **77**, 3971 (1995).
[2] Z. Zhang, L. Z. Hon, P. Wigen, and K. Dunadjela, Phys. Rev. B **50**, 6094 (1994).
[3] J. J. de Vries and W. M. de Jonge, J. Appl. Phys. **75**, 6440 (1994).
[4] A. Murayama and M. Miyamura, J. Appl. Phys. **69**, 5661 (1991).
[5] R. S. Iskhakov, Zh. M. Moroz, I. S. Édel'man, and L. A. Chekanova, JETP Lett. **63**, 770 (1996).
[6] A. Lauade, J. Magn. Magn. Mater. **92**, 143 (1990).

Translated by M. E. Alferieff

On edge states in superconductors with time inversion symmetry breaking

G. E. Volovik

Low Temperature Laboratory, Helsinki University of Technology, 02150 Espoo, Finland; L. D. Landau Institute of Theoretical Physics Russian Academy of Sciences, 117940 Moscow, Russia

(Submitted 8 September 1997)
Pis'ma Zh. Éksp. Teor. Fiz. **66**, No. 7, 492–496 (10 October 1997)

Superconducting states with different internal topology are discussed for the layered high-T_c materials. If the time inversion symmetry is broken, the superconductivity is determined not only by the symmetry of the superconducting state but also by the topology of the ground state. The latter is determined by the integer-valued momentum-space topological invariant N. The current carrying boundary between domains with different N ($N_2 \neq N_1$) is considered. The current is produced by fermion zero modes, the number of which per layer is $2(N_2 - N_1)$. © *1997 American Institute of Physics.*
[S0021-3640(97)00919-5]

PACS numbers: 74.20.Fg

1. INTRODUCTION

Recently a new phase transition in high-temperature superconductors was found[1] in Ni-doped $Bi_2Sr_2CaCu_2O_8$. It occurs at low temperature, $T \sim 200$ mK, and seems to correspond to the opening of the gap in the superconductor, which is gapless (contains lines of nodes) above the transition. Since a gap usually appears in a superconductor with lines of nodes if the time inversion ($\mathcal{T}$) symmetry is violated, this suggests that the spontaneous breaking of the $\mathcal{T}$ symmetry occurs in the new transition. Such a transition can be caused by interaction with magnetic impurities.

Some evidence of the additional symmetry breaking with opening of the gap in pure $Bi_2Sr_2CaCu_2O_8$ in the presence of a magnetic field was reported in Ref. 2. The complex order parameter $d_{x^2-y^2} + id_{xy}$ was proposed in Ref. 3 for describing this experiment. The possibility of broken $\mathcal{T}$ symmetry within the grain boundaries and twin boundaries has also been discussed.[4,5]

Since broken $\mathcal{T}$ symmetry is now becoming popular for the high-temperature superconductors, we discuss some consequences of the broken $\mathcal{T}$ symmetry in the $D=2$ spatial dimensions relevant for layered superconductors. These consequences are similar to those in thin films of superfluid ^{3}He-A and other 2D systems where $\mathcal{T}$ symmetry is broken. They are described in terms of the integer-valued topological invariant of the ground state,[6–10] which gives rise to chiral edge states on the boundary of superconductor and in some cases to quantization of Hall conductivity. We discuss here this topological invariant for the layered superconductors.

2. INTERNATIONAL TOPOLOGICAL INVARIANT

In the BCS model of the high-T_c superconductor, the quasiparticle spectrum is obtained from the Bogoliubov–Nambu Hamiltonian

$$\mathcal{H}=\tau_3\epsilon(\mathbf{k})+\tau_1\Delta_1(\mathbf{k})+\tau_2\Delta_2(\mathbf{k})\equiv\vec{\tau}\cdot\mathbf{m}(\mathbf{k}), \tag{2.1}$$

where τ_i are the 2×2 Pauli matrices in particle–hole space; $\mathbf{k}$ is the 2D vector of the in-plane linear momentum. In the simplest model

$$\epsilon(\mathbf{k})=\frac{\mathbf{k}^2-k_F^2}{2m},\quad \Delta_1(\mathbf{k})=d_1(n_x^2-n_y^2)+s_1,\quad \Delta_2(\mathbf{k})=2d_2n_xn_y+s_2, \tag{2.2}$$

where $\hat{n}=(n_x,n_y)=\mathbf{k}/|\mathbf{k}|$. The gap function $\Delta_1(\mathbf{k})$ describes the original $d_{x^2-y^2}+s$ state of the high-T_c superconductor, where the admixture of the s state comes from the orthorhombic deviation of the crystal symmetry from the tetragonal. It is believed that s_1 is less than d_1, so the gap nodes do not disappear in the mixture, but are shifted from their symmetric positions in the tetragonal crystal.

The function $\Delta_2(\mathbf{k})$ appears in the state with broken $\mathcal{T}$ symmetry. The $\mathcal{T}$ symmetry can be broken in two ways: with conservation of the symmetry $\mathcal{I}$ with respect to reflection in $\langle 100\rangle$ crystal axis (cf. Ref. 11), or with conservation of the combined symmetry $\mathcal{IT}$. In the $\mathcal{I}$-symmetric state one has $d_2=0$, while in the $\mathcal{IT}$-symmetric state $s_2=0$. However, we consider here the more general case, when both $\mathcal{I}$ and $\mathcal{IT}$ are broken and one has a mixture of is and id components. Our goal is to show that the properties of the system at $T=0$ are determined by the ground state topology rather than by symmetry.

In the energy spectrum of the broken-$\mathcal{T}$-symmetry state, there should appear a gap

$$\Delta=\min|E(\mathbf{k})|\neq0,\quad E^2(\mathbf{k})=m^2(\mathbf{k})=\epsilon^2(\mathbf{k})+\Delta_1^2(\mathbf{k})+\Delta_2^2(\mathbf{k}). \tag{2.3}$$

There are exceptions from this rule: at certain values of the parameters satisfying the condition

$$(s_1/d_1)^2+(s_2/d_2)^2=1 \tag{2.4}$$

the gap Δ becomes zero at some points $\mathbf{k}$. This equation thus determines the surfaces in the phase space of the parameters $s_1,\ d_1,\ s_2,\ d_2$, which separate the regions of the gapped superconducting states. On these surfaces the superconductivity is gapless.

The gapped superconducting states on different sides of the surface of gapless superconductivity have the same symmetry. But these states are different in terms of the internal topology, determined by the topological invariant of the ground state:[10]

$$N=\frac{1}{4\pi}\int d^2k\ \hat{m}\cdot\left(\frac{\partial\hat{m}}{\partial k_x}\times\frac{\partial\hat{m}}{\partial k_y}\right),\quad \hat{m}=\mathbf{m}/|\mathbf{m}|. \tag{2.5}$$

In our simple model this invariant is

$$N=0,\quad \text{if}\ \left(\frac{s_2}{d_2}\right)^2+\left(\frac{s_1}{d_1}\right)^2>1 \tag{2.6}$$

and

$$N=2\ \mathrm{sign}(d_1 d_2), \quad \text{if } \left(\frac{s_2}{d_2}\right)^2+\left(\frac{s_1}{d_1}\right)^2<1. \tag{2.7}$$

The sign of N is determined by the relative sign of real and imaginary components of the d-wave order parameter. The transition between states with different integer-valued invariant N occurs via the gapless intermediate state (see similar phenomena in the thin films of ^{3}He-A, where the $\mathcal{T}$ symmetry is also broken[10]).

In general the order parameter is more complicated; moreover, the system of interacting fermions cannot be described by an effective Hamiltonian of the type (2.1). The topological invariant of the ground state nevertheless exists, but it is expressed in terms of the Green's functions.[6,10]

3. CHIRAL EDGE STATES IN DOMAIN WALLS

Because of the 2-fold degeneracy of the $\mathcal{T}$-symmetry-broken states, there can be domain walls: surfaces in real space separating domains with opposite parity. If $N\neq 0$, the degenerate superconducting states have opposite values of N. Because of the jump of N across the domain wall, the wall must contain fermion zero modes. These are the gapless branches $E(k_\parallel)$, where $k_\parallel$ is the linear momentum along the wall; they cross zero energy as $k_\parallel$ varies. These fermion zero modes correspond to the chiral gapless edge states in the quantum hall effect (see Ref. 9 for the p-wave pairing in ^{3}He-A film and Ref. 3 for the pure d-wave case with $s_1=s_2=0$). Close to zero energy the spectrum of the ath mode is linear:

$$E_a(k_\parallel)=c_a(k_\parallel-k_a). \tag{3.1}$$

There is an index theorem which determines the algebraic number ν of the fermion zero modes, i.e., the number of modes crossing zero with positive slope, minus the number of modes with negative slope,

$$\nu=\sum_a \mathrm{sign}\ c_a\,. \tag{3.2}$$

According to the index theorem the number ν per CuO$_2$ layer for a wall separating the superconducting states with $N=N_1$ and $N=N_2$ is

$$\nu=2(N_2-N_1). \tag{3.3}$$

If one considers the boundary between superconductor and insulator, the invariant N on the insulating side should be put to zero.

The fermion zero modes in the domain wall have the same origin as the fermion zero modes in spectrum of the Caroli–de Gennes–Matricon bound states in the vortex core, where the $\mathcal{T}$ symmetry is also broken.[12] In the latter case the chiral fermions are orbiting around the vortex axis, which corresponds to the motion along the closed domain boundary.[13] For a circular domain wall of radius R the edge state have an angular momentum $Q=k_\parallel R$, and from Eq. (3.1) one obtains the spectrum of the low-energy bound states in terms of the angular momentum Q:

$$E_a(Q)=\omega_a(Q-Q_a). \tag{3.4}$$

Here $\omega_a = c_a/R$ is the angular velocity of the rotation along the closed trajectory. This equation represents the general spectrum of fermions bound to the vortex core Refs. 14–16. The number of fermion zero modes in the vortex core which have branches $E_a(Q)$ that cross zero energy as functions of Q is also determined by the index theorem:[17]

$$\nu = \sum_a \text{sign } \omega_a = 2N, \tag{3.5}$$

but now N is the winding number of the vortex.

4. CURRENT CARRYING BY EDGE STATES

The breaking of the $\mathcal{T}$ symmetry leads to a ground-state current carried by the occupied negative energy states in the domain wall. The topological characteristics of the fermionic charge (current) accumulated by the general texture in ^{3}He-A, where $\mathcal{T}$ symmetry is broken, was discussed in Ref. 18. In our case the current is concentrated within the domain wall, and this current along the closed wall gives rise to an angular momentum of the domain. The magnitude of the angular momentum can vary because of the fermionic charge accumulated by the superconducting state. This accumulation occurs due to spectral flow in the fermion zero modes (see Ref. 15).

If the superconducting state is axisymmetric and has no additional breaking of spatial parity, the angular momentum of superconductor per electron is quantized at $T=0$: $L_z = \frac{1}{2}\hbar N$. This angular momentum does not depend on details of the gap structure and is determined only by the topological invariant N. In our simple model the axisymmetric state with nonzero $N=2$ occurs if $s_1 = s_2 = 0$ and $d_1 = d_2$. However, when one deforms the superconducting state from the axisymmetric to the relevant one, the momentum L_z will be substantially modified by the deformation if a spectral flow takes place during such a deformation.[15] But typically L_z remains of the same order.

One can estimate the change of the edge current under the deformation of the superconducting state from the most symmetric one. The mass current along the domain wall changes in the following way:

$$\Delta J_M = \frac{e}{8\pi\hbar} \sum_a k_a^2 \text{ sign } c_a . \tag{4.1}$$

This gives the following change of the electric current

$$\Delta J_e = \frac{e}{8\pi\hbar} \sum_a \frac{k_a^2}{m} \text{ sign } c_a . \tag{4.2}$$

The Eq. (4.1) is obtained from the following consideration. The change in the current is caused by the spectral flow which takes place during the change of the system parameters (s_1, s_2, d_1, d_2). If δn_a is the number of levels on the ath branch which cross zero energy under the deformation of the state, the variation of the current is

$$\delta J_M = \sum_a k_a \delta n_a , \tag{4.3}$$

since each level, when it crosses zero, carries a momentum k_a with it. On the other hand the variation of the number of levels is the variation of the momentum divided by the phase space volume $2\pi\hbar$:

$$\delta n_a = \frac{\delta k_a}{2\pi\hbar} \operatorname{sign} c_a . \tag{4.4}$$

This gives

$$\delta J_M = \frac{1}{8\pi\hbar} \sum_a \delta(k_a^2) \operatorname{sign} c_a . \tag{4.5}$$

An extra 1/2 is introduced to compensate for the duplication of degrees of freedom when both particle and hole states are considered in the Bogoliubov description in Eq. (2.1). Equation (4.5) leads to Eq. (4.1).

In some special cases one has $k_a = 0$ and the change in the edge current becomes zero. This may happen if the spatial parity $\mathcal{P}$ is not violated and for special orientations of the domain wall. In general case the momentum for which the energy is zero has a finite value, which is typically of the order of k_F. There are can be special orientations of the wall for which $k_a = \pm k_F$. In this case one obtains the quantized response of the current to the chemical potential μ: $\delta J_e = e\nu\delta\mu/4\pi\hbar$ (Ref. 9). However, this is not a general result. In general $\Delta J_e \sim e\nu k_F^2/4\pi\hbar m$ if $\nu = \Sigma_a \operatorname{sign} c_a \neq 0$.

We have described different classes of superconductivity in CuO_2 planes with broken time inversion symmetry. The superconducting states may have the same symmetry but differ in their topological properties. The superconducting states are described by the integer-valued momentum-space topological invariant N. The boundary separating domains with different N $(N_2 \neq N_1)$ contains fermion zero modes, the number of which is determined by $N_2 - N_1$. These fermions are current-carrying and produce nonzero current along the domain wall in the ground states if $N_2 \neq N_1$.

The magnitude of the edge current is usually of the order of $ek_F^2/4\pi\hbar m$. It is large compared to the magnitude obtained by Laughlin (see Eq. (21) of Ref. 3), who considered the pure d-wave case, which has $N = 2$. Laughlin's result can be obtained if one takes $k_a^2/2m = \Delta$ in Eq. (4.2), where Δ is the gap in the spectrum in Eq. (2.3). However, there are no grounds for making such an identification.

The domain-wall fermions are also important in particle physics. For example the chiral fermions in our $3+1$ dimensions can be reproduced by zero modes bound to a domain wall in $4+1$ dimensions.[19]

This work was supported by the Russian Fund for Fundamental Research, Grant 96-02-16072.

[1] R. Movshovich, M. A. Hubbard, M. B. Salamon *et al.*, http://xxx.lanl.gov/abs/cond-mat/9709061.
[2] K. Krishana, N. P. Ong, Q. Li *et al.*, Science **277**, 83 (1997).
[3] R. B. Laughlin, http://xxx.lanl.gov/abs/cond-mat/9709004.
[4] M. Sigrist, K. Kuboki, P. A. Lee *et al.*, Phys. Rev. B **43**, 2835 (1996).
[5] M. E. Zhitomirsky and M. B. Walker, Phys. Rev. Lett. **79**, 1734 (1997).
[6] G. E. Volovik and V. M. Yakovenko, J. Phys.: Condens. Matter **1**, 5263 (1989).

[7] V. M. Yakovenko, Phys. Rev. Lett. **65**, 251 (1990); Fizika (Zagreb) **21**, Suppl. 3, 231 (1989); http://xxx.lanl.gov/abs/cond-mat/9703195.
[8] V. M. Yakovenko, Phys. Rev. B **43**, 11353 (1991).
[9] G. E. Volovik, JETP Lett. **55**, 368 (1992).
[10] G. E. Volovik, *Exotic Properties of Superfluid* ^{3}He, Singapore: World Scientific, 1992.
[11] J. F. Annett, N. Goldenfeld, and A. J. Leggett, in *Physical Properties of High Temperature Superconductors*, edited by D. M. Ginsberg, Singapore: World Scientific, 1996, Vol. 5, p. 375.
[12] C. Caroli, P. G. de Gennes, and J. Matricon, Phys. Lett. **9**, 307 (1964).
[13] G. E. Volovik, http://xxx.lanl.gov/abs/cond-mat/9709159.
[14] N. B. Kopnin, Physica B **210**, 267 (1995).
[15] G. E. Volovik, JETP Lett. **61**, 958 (1995).
[16] N. B. Kopnin and G. E. Volovik, Rotating vortex core: An instrument for detecting the core excitations, http://xxx.lanl.gov/abs/cond-mat/9706082, submitted to Phys. Rev. B.
[17] G. E. Volovik, JETP Lett. **57**, 244 (1993).
[18] M. Stone and F. Gaitan, Ann. Phys. **178**, 89 (1987).
[19] D. B. Kaplan and M. Schmaltz, Phys. Lett. B **368**, 44 (1996).

Published in English in the original Russian journal. Edited by Steve Torstveit.

Near field scanning optical spectroscopy of InP single quantum dots

G. Guttroff,[a] M. Bayer, and A. Forchel
Technische Physik, Universität Würzburg Am Hubland, D-97074 Würzburg, Germany

D. V. Kazantsev
Institute of Theoretical and Experimental Physics, Russian Academy of Sciences, 117333 Moscow, Russia

M. K. Zundel and K. Eberl
Max-Planck-Institut für Festkörperforschung, 70054 Stuttgart, Germany

(Submitted 8 September 1997)
Pis'ma Zh. Éksp. Teor. Fiz. **66**, No. 7, 497–501 (10 October 1997)

We study InP quantum dots which are prepared by strain induced self-assembly on GaAs substrates with a GaInP buffer layer using a near field scanning optical microscope operating at near liquid He bath temperatures in the collection mode. Single quantum dots are identified spatially and spectrally due to their photoluminescence spectrum. Series of luminescence lines due to single dots of different sizes are discussed in terms of dot height and width fluctuations. © *1997 American Institute of Physics.* [S0021-3640(97)01019-0]

PACS numbers: 73.61.Ey, 73.20.Dx, 07.79.Fc, 61.16.Ch

In recent years near-field scanning optical microscopy (NSOM) has proven to be a very useful tool for the investigation of quantum-sized semiconductor structures because it provides optical spectroscopy with a spatial resolution on the order of the size of the quantum structures themselves.[1–4] The main factors limiting the spatial and spectral resolution are, e.g., the penetration depth of light in semiconductors and the carrier diffusion, which are on a scale of hundreds of nanometers. The last effect is especially critical for the investigation of quantum structures in the case of nonresonant excitation of the barrier material. Both problems are especially troublesome for NSOMs operating in the illumination mode. We show that it is possible to overcome these problems using a NSOM which is operated in the collection mode.

The scanning head, as illustrated in Fig. 1, was placed inside a standard variable temperature helium cryostat and cooled by a helium gas flow. Experiments can be performed at sample temperatures near liquid-helium temperature. The fiber tip used for this experiment was fabricated with a fiber pulling setup and was coated with a 100 nm aluminum layer. Tip apertures below 100 nm in diameter have been realized. The scanning process is done with a piezo scanning head and controlled with a shear force feedback via laser 1, which is guided through the cryostat windows and crosses the fiber tip. Both the laser diode and the photodiode are installed outside of the cryostat. For excitation of the carriers, an Ar^+-laser operating at 514 nm is focused by a lens system through one cryostat window at the position of the fiber tip on the sample. The excitation

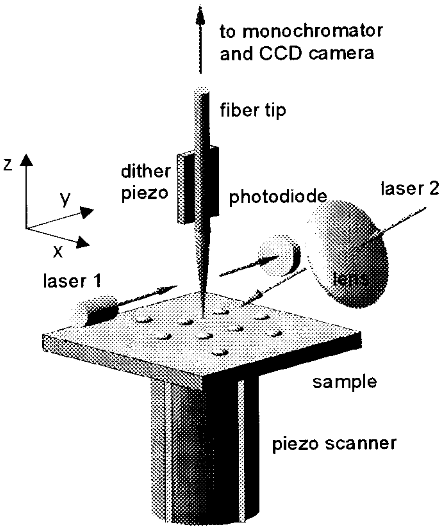

FIG. 1. Experimental setup of the collection-mode near-field optical microscope inside a He cryostat.

power can be varied up to 100 W/cm^2. The photoluminescence (PL) spectrum $I(x,y,\lambda)$ collected with the fiber tip at position $[x,y]$ is dispersed with a 0.3 m monochromator and detected by a liquid-nitrogen-cooled Si-CCD camera.

By detecting the PL with this collection mode setup only photons from carriers recombining below the tip are collected, and so the spatial and spectral resolution of the PL signal depends primarily on the quality of the tip. Toda *et al.*[3] and Flack *et al.*[4] have demonstrated investigations of quantum dot structures with a NSOM in the illumination mode. However, for this mode the diffusion of optically excited carriers limits the spatial resolution.[3–10] In the present setup using a collection mode, diffusion effects are involved in the population of the dot by electron–hole pairs. The spatial resolution, however, is determined entirely by the collection of the luminescence in the near field mode.

The samples were grown on semi-insulating (100) GaAs substrates in a conventional MBE system using GaP as the P_2 source. For further details about the P_2 source see Ref. 11. After removal of the oxide, a 400 nm thick GaAs buffer is grown under a beam equivalent pressure of 4×10^{-6} Torr at a substrate temperature of 580°C. Then the deposition is interrupted to change from As-rich to P-rich growth conditions. The deposition sequence includes 200 nm of $Ga_{0.46}In_{0.54}P$, followed by 3.0 monolayers (ML) of InP. The InP islands are finally overgrown by a 50 nm thick $Ga_{0.46}In_{0.54}P$ layer. This layer sequence is grown at 470°C substrate temperature and under a P_2 beam equivalent pressure of 6×10^{-6} Torr. The surface of the $Ga_{0.46}In_{0.54}P$ layer shows a 2×1 reconstruction in reflection high-energy electron diffraction (RHEED). We use a growth rate of 1 ML/s for $Ga_{0.46}In_{0.54}P$ and 0.5 ML/s for InP. The composition of the $Ga_{0.46}In_{0.54}P$ layers is determined by double-crystal x-ray diffraction (DCXR). The InP quantum dots grown with this procedure have approximately a diameter of 18 nm and a height of 2.4 nm, as indicated by TEM studies.[12]

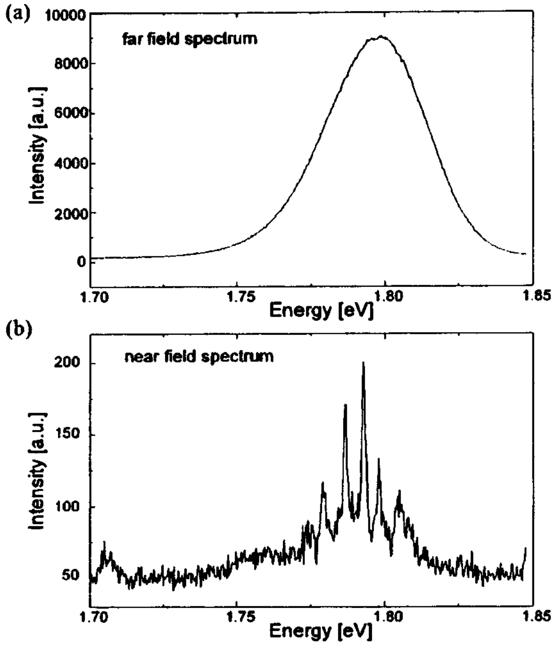

FIG. 2. a—Photoluminescence spectrum detected with the fiber tip at a fixed position on the sample in the far field ($z \gg \lambda$). b—PL spectrum in the near-field regime ($z < \lambda$), $T = 10$ K.

To test the spectral resolution of the system, PL spectra were recorded at fixed sample positions. For the far-field case, which means that the tip-to-sample distance z is significantly larger than the wavelength λ of the light, the PL of a relatively large number of QDs is observed. Since the size of these QDs varies statistically around a mean value, a Gaussian shaped PL signal is seen in the spectrum (Fig. 2a). When the tip is placed in the near field regime ($z < \lambda$) sharp emission lines of single QDs with intensities well above the noise level are observed, as shown in Fig. 2b. The minimum spectral linewidths of the luminescence spikes are around 1 meV, which is approximately the spectral resolution. The energy of these emission lines depends on the position $[x,y]$ at which the spectra are recorded.

Because the sample was overgrown with a 50 nm thick $Ga_{0.46}In_{0.54}P$ layer, no spatial variations can be seen with AFM and STM techniques. The overgrowth layer also limits the spatial resolution for detection of the spectra to the scale of the layer thickness, since photons from carriers recombining inside the quantum dots are emitted isotropically 50 nm beneath the surface.

A typical data set is displayed in Fig. 3. The plot consists of 76 spectra, each of which was taken with an integration time of 30 s, and for every spectrum the sample was moved about 26 nm along the x direction. The intensity is scaled such that bright areas in the energy-versus-x-position image in Fig. 3 correspond to a large number of photon counts in the PL spectrum. Spectra at fixed sample positions $x = x_1, x_2, x_3$ are displayed in Fig. 4b.

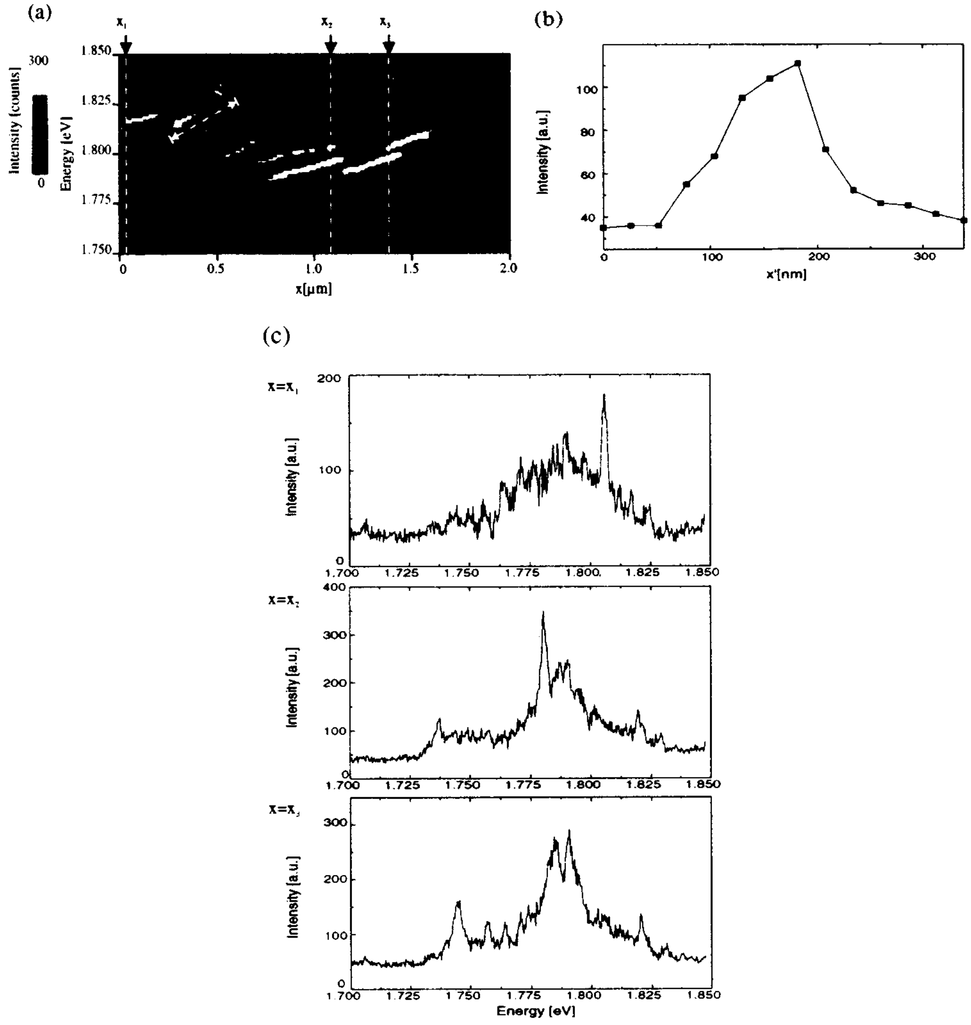

FIG. 3. PL recorded in the near field regime during a linescan in the x direction at $T=10$ K.

One observes that single emission lines far above the noise level appear and disappear as the tip is scanned along the x direction. These lines, which arise from single quantum dots, exist over distances in the range of 100 to 300 nm. The linescan in Fig. 3 is accompanied by a blue shift of the single dot emission lines of about 10 meV. If the scanning direction is reversed, we see an exactly corresponding red shift. Measurements of the temperature dependence and excitation-intensity dependence of the PL were made at single positions on this sample, and according to these results we attribute this energy shift to local heating effects of the sample by the fiber tip, which is placed in the laser beam focus in close proximity to the sample. However other effects like the deformation of the quantum dot band structure by the strong electric field due to the close proximity

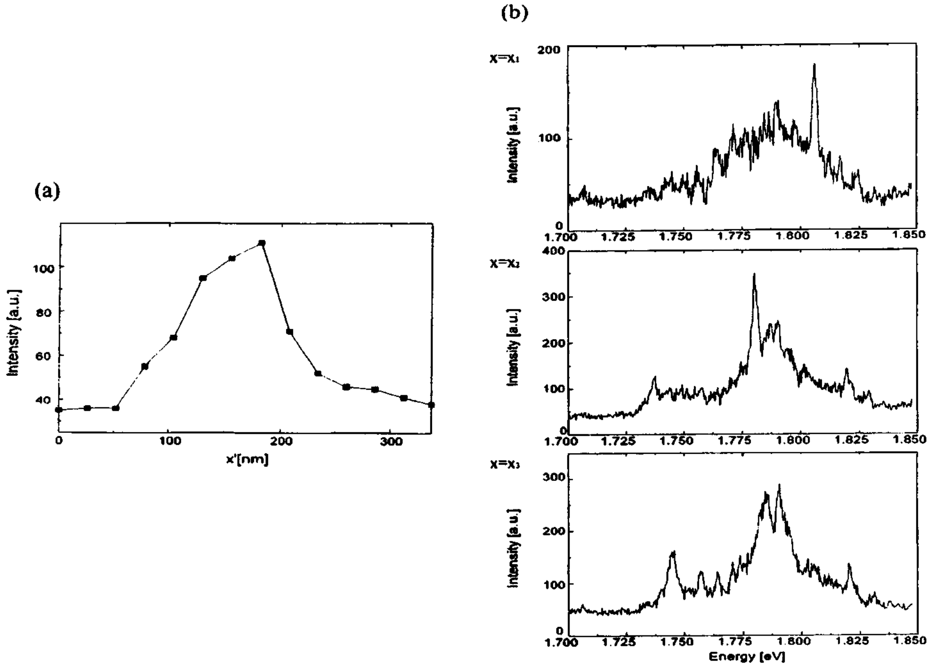

FIG. 4. a—Linecut across an observed dot along x' as indicated in Fig. 3. b—Several linecuts of Fig. 3, shown at different positions x_1, x_2, x_3.

of the fiber tip to the quantum dot in the laser focus could also play an important role.

A linecut along a typical emission line is shown in Fig. 4a. The FWHM along the x-direction of this plot indicates a spatial resolution of about 100 nm. The density of the quantum dots can be determined by the average number of peaks in the PL spectra recorded in the near field. We observe at the average about 5 peaks, therefore the dot density is $500/\mu m^2$ for a spatial resolution of 100 nm as determined in the linescan. This value agrees very well with previous measurements done with cross sectional TEM and AFM.[12]

As shown in Fig. 4b, the near-field emission lines of a dot are characterized by two different energy separations. First, a typical spacing between single dot transition peaks on the order of 5 meV occurs frequently in the spectra. In addition, we observe also a much larger spacing of about 50 meV in many spectra (e.g., bottom and center traces in Fig. 4b). We attribute the luminescence lines with smaller energy separation to dots with slightly different diameters, whereas the larger spacing between the luminescence lines may be due to height variations of the approximately disk-shaped dots. By using a quantum dot model based on electron and hole effective masses of $m_e/m_0=0.079$ and $m_{hh}/m_0=0.150$ for the strained InP and with conduction and valence band discontinuities of 676 meV and 70 meV, respectively, we obtain for a one-monolayer height fluctuation a shift of the emission peak of about 50 meV. Within this model the smaller energy spacing corresponds to changes of the dot diameter of about 10 percent. Both values are consistent with TEM and AFM studies[12] of size fluctuations in self-assembled dots prior to overgrowth. In addition, some of the observed single-dot transition lines might be due to ground and excited state recombination in a given dot. This is also indicated by the similar spatial extent and blue shift of some of the transition streaks in the linescan (Fig. 3). Due to the small dot size the calculated energy spacing between allowed transitions in the ground state and the first excited states of 40 meV is larger than the observed separation of most of the peaks. This may indicate contributions of forbidden transitions in the quantum dots, which could be promoted, e.g., by shape anisotropies of the dots or local electric fields.

In summary, we have studied single InP dot emission lines with a NSOM operating in the collection mode. Carrier diffusion and light penetration effects, which limit the resolution of spatially resolved spectroscopy in illumination mode setups, can be largely eliminated by operating the NSOM in the collection mode. By using the combined spatial and spectral resolution of our system we are able to distinguish dots with varying height from dots with variations of the lateral diameter.

[a)] e-mail: guttroff@physik.uni-wuerzburg.de

---

[1] E. Betzig, J. K. Trautman, T. D. Harris *et al.*, Science **251**, 1468 (1991); E. Betzig, P. L. Finn, and J. S. Weiner, Appl. Phys. Lett. **60**, 2482 (1992).
[2] H. F. Hess, E. Betzig, T. D. Harris *et al.*, Science **264**, 1740 (1994).
[3] Y. Toda, M. Kourogi, M. Ohtsu *et al.*, Appl. Phys. Lett. **69**, 827 (1996).
[4] F. Flack, N. Samarth, V. Nikitin *et al.*, Phys. Rev. B **54**, 17312 (1996).
[5] G. Guttroff, J. W. Keto, C. K. Shih *et al.*, Appl. Phys. Lett. **68**, 3620 (1996).
[6] A. Zrenner, L. V. Butov, M. Hagn *et al.*, Phys. Rev. Lett. **72**, 3382 (1994).
[7] K. Brunner, G. Abstreiter, G. Böhm *et al.*, Phys. Rev. Lett. **73**, 1138 (1994).
[8] J.-Y. Marzin, J.-M. Gérard, A. Izraël *et al.*, Phys. Rev. Lett. **73**, 716 (1994).
[9] D. Hessman, P. Castrillo, M.-E. Pistol *et al.*, Appl. Phys. Lett. **69**, 749 (1996).
[10] A. Kurtenbach *et al.*, in *Low Dimensional Structures Prepared by Epitaxial Growth or Regrowth on Patterned Substrates*, edited by K. Eberl, P. M. Petroff, and P. Demeester, NATO ASI Series E **298**, 59 (1995).
[11] T. Shitara and K. Eberl, Appl. Phys. Lett. **65**, 356 (1994).
[12] K. Eberl, A. Kurtenbach, K. Häusler *et al.*, Mater. Res. Soc. Symp. Proc. **379**, 185 (1995).

Anomalous behavior of the structural parameters of $YBa_2Cu_4O_8$ single crystals at the transition to the superconducting state

V. N. Molchanov[a] and V. I. Simonov
Institute of Crystallography, Russian Academy of Sciences, 117333 Moscow, Russia

M. K. Blomberg and M. Yu. Merisalo
Department of Physics, Helsinki University, FIN-00014, Helsinki

(Submitted 9 September 1997)
Pis'ma Zh. Éksp. Teor. Fiz. **66**, No. 7, 502–506 (10 October 1997)

High-precision x-ray crystallographic studies of $YBa_2Cu_4O_8$ single crystals ($T_c = 70$ K) are performed at eight temperatures in the interval 20–295 K. It is found that a number of structural parameters exhibit anomalous behavior near the superconducting transition of the crystal. A characteristic effect near the phase transition is the displacement of the O1 bridge atom that joins the Cu1 atom of the cuprate chain to the Cu2 atom of the cuprate plane. The shift of this oxygen toward the Cu2 atom is indicative of a change in the Cu2–O1 chemical bond and of charge transfer to the cuprate plane in the process of the transition of the crystal to the superconducting state. © *1997 American Institute of Physics.* [S0021-3640(97)01119-5]

PACS numbers: 61.50.Ks, 74.72.Bk

Because isomorphic substitutions, disordering, and twinning do not occur in high-quality $YBa_2Cu_4O_8$ single crystals (Y phase 124), such crystals are very attractive for performing high-precision structural investigations at temperatures below and above the superconducting transition. The behavior of the structural parameters near the phase transition is of special interest. Much of the structural work on 124 compounds has been done on powder samples,[1,2] and there are only a few publications on single crystals.[3,4] Anomalies in the behavior of the structural parameters near the phase transition, as a rule, are not observed in the neutron diffraction and x-ray investigations performed on powders, though there are indications of the presence of such anomalies.[3,5] We have performed complete x-ray crystallographic investigations of a $YBa_2Cu_4O_8$ single crystal ($T_c = 70$ K) with the dimensions $0.213\times 0.153\times 0.032$ mm at temperatures of 20, 53, 59, 65, 77, 89, 95, and 295 K. The crystal is orthorhombic, its symmetry space group is $Ammm$, $Z=2$, the unit cell parameters at room temperature are $a=3.8400(7)$, $b=3.8704(7)$, and $c=27.225(3)$ Å. The structural parameters were refined at all temperatures by a full-matrix version of the least-squares method using 613 independent structural amplitudes. In the process, 36 parameters were refined. The final discrepancy factors between the experimental structural amplitudes and the amplitudes calculated using re-

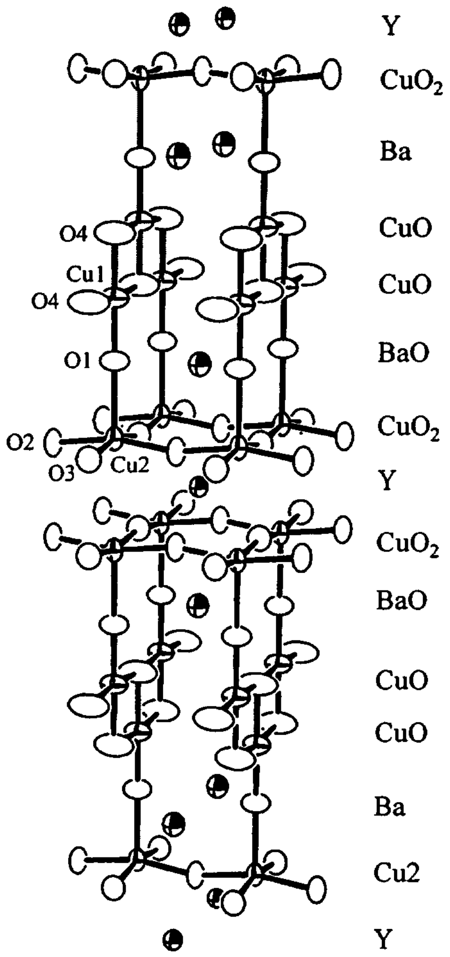

FIG. 1. Model of the atomic structure of the high-T_c superconductor $YBa_2Cu_4O_8$.

fined models were in the range 1.1–1.5% at all temperatures; this attests to the reliability of the results obtained. A model of the atomic structure of the compound 124 is reproduced in Fig. 1.

Figure 2 shows the temperature dependence of the unit cell parameters of a $YBa_2Cu_4O_8$ single crystal. Of course, the behavior of the cell volume does not exhibit any anomalies near the phase-transition temperature. The ''stiffness'' of the parameter b is due to the fact that double cuprate chains extend along this direction in the structure. The behavior of the c axis reflects the decrease in the temperature derivative of the interlayer distances at the superconducting transition of the crystal. The anomaly in the behavior of the a axis near T_c is due to the change occurring in the interatomic spacing as a result of strengthening of the chemical bond between the Cu2 and O2 atoms in the cuprate plane. Comparing the behavior of the parameters a and b, we can see that the

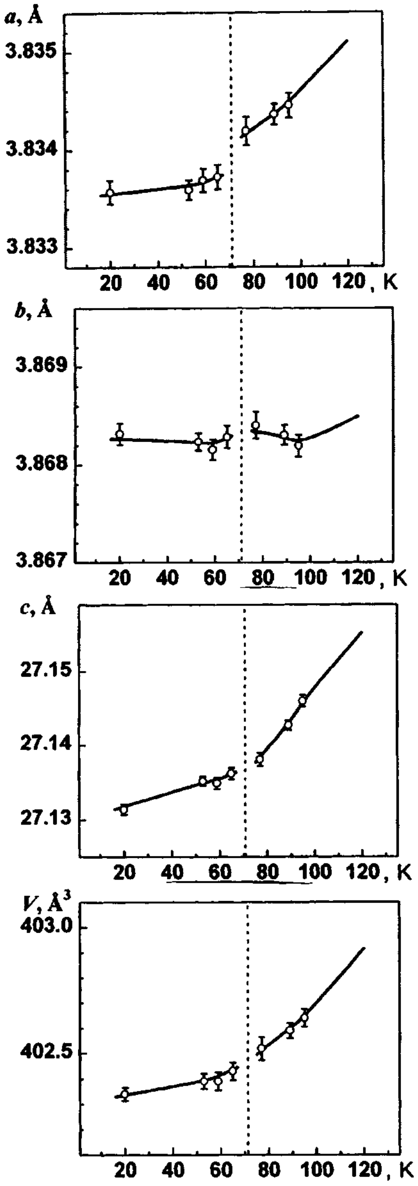

FIG. 2. Unit cell parameters a, b, c, and V of a $YBa_2Cu_4O_8$ single crystal, $T_c = 70$ K, as a function of temperature.

degree of orthorhombic distortion of the structure increases at the superconducting transition of the crystal.

A detailed analysis of the behavior of the structural parameters at the superconducting transition of the crystal will be published later in a lengthier paper. Here, in Fig. 3, we

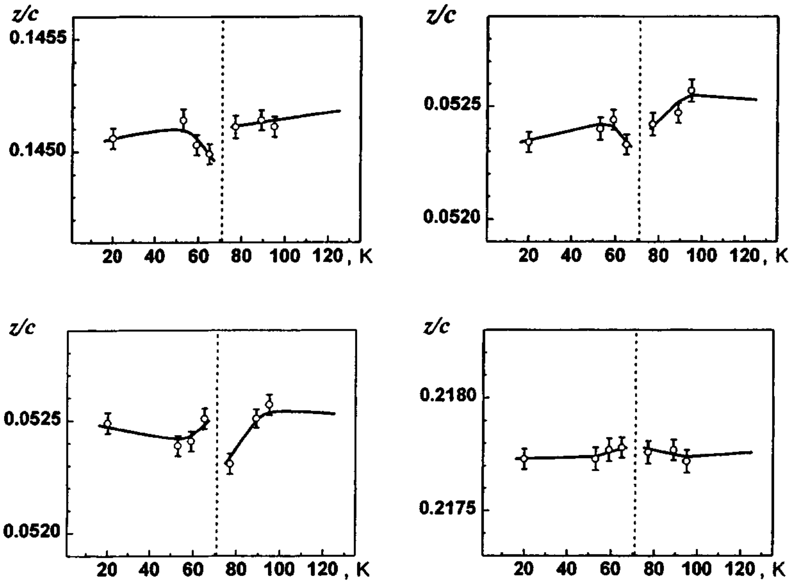

FIG. 3. Positions of the basal oxygen atoms O1, O2, O3, and O4 as a function of temperature in $YBa_2Cu_4O_8$ crystals along the *c* axis perpendicular to the structural layers.

present as an example the temperature dependences of the *z* coordinates of the basal oxygen atoms. The behavior of these coordinates in relative units characterizes the displacement of the oxygen atoms in a direction perpendicular to the layers of the structure. One can see from the dependences presented that in the process of the phase transition the O1 bridge oxygen shifts toward the Cu2 atom of the cuprate plane. This shift is a measure of the change in the electronic structure of the compound and of the charge transfer through the bridge O1 atom to the cuprate plane. The O2 and O3 atoms of the cuprate plane behave in a different manner. The result of this behavior is that in the superconducting state these oxygen atoms form a more regular square environment around a Cu2 atom. The *z* coordinate of the O4 atom of the cuprate chain remains practically unchanged in the entire temperature interval 20–295 K. The displacements of the cations in the experimental temperature range are appreciable but much smaller than those of the oxygens.

Turning now to an analysis of the interatomic distances, which are determined by the chemical bonds between the atoms in the structure, the pyramidal CuO_5 groups, whose bases form the cuprate plane, undergo the largest changes near a superconducting phase transition of the crystal. Figure 4 displays the structure of a CuO_5 group and its coupling via the O1 bridge oxygen to the CuO_4 squares from the double cuprate chains. The plots in this figure indicate the behavior of the interatomic distances Cu1–O1, O1–O2, and O1–O3 near a phase transition. Along the curve of the variation of the Cu2–O1 distance constructed from our data we show two points which were published in Ref. 3. These points were obtained from neutron powder diffraction data. They fall near our curve, which was constructed from the x-ray diffraction data for a single crystal. The

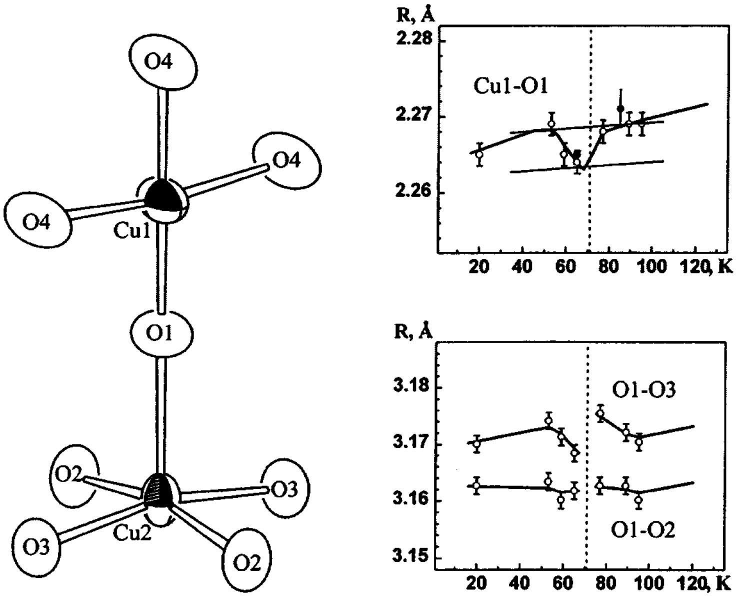

FIG. 4. Diagram illustrating the joining of the Cu2 atom of the cuprate plane to the Cu1 atom of the double chains in the $YBa_2Cu_4O_8$ structure via the O1 bridge oxygen, and plots of the temperature dependence of the Cu2–O1 (● — two points from Ref. 3, ○ — our data), O1–O2, and O1–O3 distances.

decrease in the distance between the Cu2 and O1 atoms near the phase transition occurs by a shift of both atoms towards each other. The copper and oxygen displacements are in the ratio 1:3. The interatomic distance Cu2–O1 is characterized by a sharp minimum near the phase transition. As was mentioned in the analysis of the z coordinates of the O2 and O3 atoms of the cuprate plane, their displacements immediately after the phase transition are directed in opposite directions. Whereas, to a first approximation, the O2 atom shifts synchronously with the O1 atom, so that the O1–O2 distance is virtually independent of the temperature, the O3 atom moves toward the O1 atom after the phase transition. The plots of the temperature dependence of the O1–O2 and O1–O3 distances demonstrate this difference in the behavior of the O2 and O3 atoms.

The presence of a minimum on the curve of the temperature dependence of the Cu2–O1 distance near a phase transition was also detected previously. Similar minima in the distance between the copper and the apical oxygen atom (in our case O1) were noted in Ref. 6 (1994) for the $Tl_2Ba_2CaCu_2O_8$ structure, $T_c = 110$ K, and in Ref. 7 (1996) for the compound $Tl_2Ba_2Ca_2Cu_3O_{10}$, $T_c = 118$ K. The corresponding curves are reproduced in Fig. 5 according to the data from the works cited. The fact that near the superconducting transition in the crystal the behavior of the bond between the copper atom of the cuprate plane with the apical oxygen is identical in three different high-T_c superconductors — the Y phase 124 and the Tl phases 2212 and 2223 — shows that this effect is of a general nature. It is natural to attribute the shortening of the Cu–O bond in the process of the superconducting phase transition of the crystal to charge transfer from the reservoir layers of the structure into the superconducting cuprate layers via the bridge oxygen

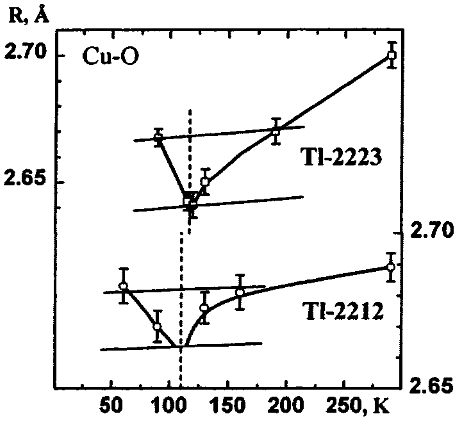

FIG. 5. Temperature dependences of the Cu–O interatomic distances from copper in the cuprate plane to the apical oxygen in the Tl phases $Tl_2Ba_2CaCu_2O_8$ (Ref. 6) and $Tl_2Ba_2Ca_2Cu_3O_{10}$ (Ref. 7).

atoms. The structures of the three superconductors listed above are characterized by the fact that they contain CuO_5 groups with shorter Cu–O distances in the cuprate plane and a longer Cu–O distance to the apical oxygen (Jahn–Teller effect).

We thank Professor E. Kaldis (Zurich, Switzerland) for providing excellent quality $YBa_2Cu_4O_8$ single crystals for the structural investigations and M. A. Gosalves (Helsinki, Finland) for assisting in the work on the x-ray diffractometer at liquid-helium temperatures. This work was made possible by its inclusion in the plans for joint studies between the Russian and Finnish Academies of Science and by financial support from the Russian Fund for Fundamental Research (Grant No. 96-02-17361).

[a]e-mail: vladimol@rsa.crystal.msk.su

---

[1] E. Kaldis, P. Fischer, A. W. Hewat *et al.*, Physica C **159**, 668 (1989).
[2] V. A. Trunov, T. Yu. Kaganovich, P. Fischer *et al.*, Physica C **227**, 285 (1994).
[3] P. Bordet, J. L. Hodeau, R. Argoud *et al.*, Physica C **162–164**, 524 (1989).
[4] B. Dabrovski, K. Zhang, J. J. Pluth *et al.*, Physica C **202**, 271 (1992).
[5] F. Izumi, Physica C **190**, 35 (1991).
[6] V. N. Molchanov, R. A. Tamazyan, V. I. Simonov *et al.*, Physica C **229**, 331 (1994).
[7] M. Hasegawa, Y. Matsushita, and H. Takei, Physica C **269**, 31 (1996).

Translated by M. E. Alferieff

Single-electron transistor effect in a two-terminal structure

S. V. Vyshenski[a)]
Nuclear Physics Institute, Moscow State University, 119899 Moscow, Russia;
Research Center for Quantum Effect Electronics, Tokyo Institute of Technology, 2-12-1,
Tokyo 152, Japan

(Submitted 2 September 1997)
Pis'ma Zh. Éksp. Teor. Fiz. **66**, No. 7, 507–511 (10 October 1997)

A peculiarity of the single-electron transistor effect makes it possible to observe this effect even in structures lacking a gate electrode altogether. The proposed method can be useful for experimental study of charging effects in structures with an extremely small central island confined between tunnel barriers (like an $\simeq 1$ nm quantum dot or a macromolecule probed with a tunneling microscope), where it is impossible to provide a gate electrode for control of the tunnel current. © *1997 American Institute of Physics.* [S0021-3640(97)01219-X]

PACS numbers: 85.30.Pq, 07.79.Cz

By definition, a device called a ''transistor'' should have three terminals. One of them (the gate) is meant to control the current flowing between the other two. The same can be said for the case of a single-electron transistor (SET). The main objective of this paper is to prove that just two terminals are sufficient for studying the SET effect in experiment, provided that the voltages applied to these two are held in a special way. Thus in the particular case of the SET, the transistor effect (TE) can be studied in systems which are not transistor devices. Although this simplification may be of no immediate use for the electronics industry, it is of importance for basic physical experiment. Here interesting and physically rich mesoscopic systems can be prepared artificially[1] or grown naturally.[2] But the nanometer size of these systems makes fabrication of the gate another challenging problem (if it is feasible at all).

We illustrate the main idea using as an example the semi-classical ''orthodox'' approximation[3] for the description of the SET dynamics of systems with a purely tunnel conductivity between metallic electrodes. In the closing section we argue that the same two-terminal method is much more generally applicable.

Consider the charge-quantized double-barrier structure in Fig. 1, which is called a SET. The total charge ne confined on the central island is a good macroscopically observable quantum number provided that $e^2/C \gg k_BT$ and $R_{1,2} \gg \hbar/e^2 \simeq 4.1$ kΩ, where $C = C_0 + C_1 + C_2 + C_g$. Traditionally a gate with a capacitive coupling C_g is present and allows for modulation of the current flowing between terminals V_1 and V_2. The modulation is due to the change in charge induced on the central island by a change in the gate voltage V_g. This is the conventional TE.

The gate may be absent from a particular structure. In Fig. 1 this case is indicated by

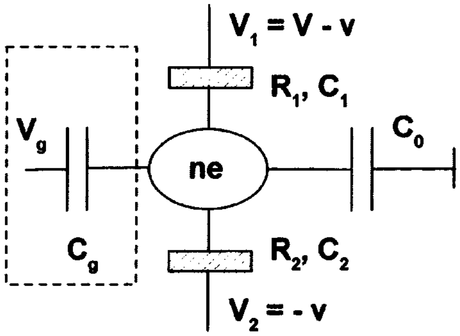

FIG. 1. Charge-quantized double-barrier structure. Junctions with tunnel resistances $R_{1,2}$ and capacitances $C_{1,2}$ are shown as boxes. The self-capacitance C_0 of the central island is shown as a capacitor connected to a point with zero potential. The gate with capacitive coupling C_g may be absent from the system.

the dashed lines around the gate. Here we can get the same modulation effect by making use of a ''hidden'' gate, which is the self-capacitance C_0 of the central island. For this we introduce a common background $-v$ added to both voltages V_1 and V_2 simultaneously. We will see that by changing the voltage v it is possible to observe the same TE, and for structures on the nanometer scale the efficiency of this v control is approximately the same as would be expected for the best possible conventional gate.

Thus we are going to exploit an unusual feature of the SET. When it has a gate (and looks like a 3-terminal structure) it in fact has 4 terminals. The effective fourth terminal is an infinitely remote point traditionally viewed as having zero potential. When a SET does not have a regular gate (and looks like a 2-terminal structure), it is effectively a 3-terminal device, and it is still possible to observe the TE, this time with a special voltage setup.

EFFECTIVE ADDITIONAL GATE

The total charge ne confined on the central island (see Fig. 1) determines its electrostatic potential $\varphi(n)$:

$$en+q_b=C\varphi(n)-C_1V_1-C_2V_2-C_gV_g\,. \tag{1}$$

Here q_b is a background charge: q_b/C is the contribution to the potential φ of the central island from charged contaminants present in the vicinity of the island.

Equation (1) implicitly uses a ''fourth terminal.'' The infinitely remote point used in the definition of the self-capacitance[4] is assumed to be at zero potential. The natural choice (employed in Eq. (1)) is to have zero potential on an isolated uncharged body. This choice fixes the gauge. The zero point of the potential is no longer arbitrary, and the value of the potential (and not just of the potential difference) acquires absolute meaning.

In other words, the self-interaction of the central island (measured by the self-capacitance parameter) is equivalent to interaction with a dedicated point of fixed potential. The most natural choice for such a point is at infinity (and the natural choice for the fixed potential value is zero). So the existence of this self-interaction is equivalent to the fact that our system has a very special point with fixed potential. This special point can be regarded as a ‘‘hidden’’ voltage terminal in our system. We will see that the voltage parameter $-v$ applied to both current terminals is measured relative to precisely this hidden terminal. This can be alternatively regarded as applying a voltage $+v$ to the hidden terminal, which will imitate one additional v voltage-driven gate.

ORTHODOX APPROXIMATION

The free-energy costs of increasing $(+)$ or decreasing $(-)$ the initial number n of electrons on the central island due to a single-electron tunneling event $(n\rightarrow n\pm 1)$ in junction 1 or 2 are:

$$F_{1,2}^{\pm}(n)=F_f-F_i=\pm e[\varphi(n\pm 1/2)]\mp eV_{1,2}=\pm(e/C)(q_b\pm e/2$$
$$+en+C_gV_g+C_1V_1+C_2V_2-CV_{1,2}). \tag{2}$$

where $F_{1,2}^{\pm}<0$ (>0) corresponds to an energetically favorable (unfavorable) event. The dissipation of this energy is part of the tunneling event and distinguishes macroscopic tunneling (considered here) from textbook quantum mechanical tunneling. For a given n, the tunneling rates in each junction are expressed[3] by

$$\Gamma_{1,2}^{\pm}(n)=\frac{-F_{1,2}^{\pm}}{e^2R_{1,2}}\,\frac{1}{1-\exp[F_{1,2}^{\pm}/(k_BT)]}. \tag{3}$$

A statistical distribution $p(n)$ of charge states n is established when the external voltages are constant. The current I_i through tunnel i in the direction from V_1 to V_2 equals

$$I_{1,2}=\pm e\sum_n p(n)[\Gamma_{1,2}^{+}(n)-\Gamma_{1,2}^{-}(n)], \tag{4}$$

where sum goes over all n for which $p(n)>0$. Kirchhoff’s law, $I_1=I_2$, holds in the steady state and demands that the distribution $p(n)$ should not change in time. More precisely, simultaneous detailed-balance equations[5] should hold for all n:

$$p(n)\Gamma^{+}(n)=p(n+1)\Gamma^{-}(n+1), \tag{5}$$

with $\Gamma^{\pm}(n)=\Gamma_1^{\pm}(n)+\Gamma_2^{\pm}(n)$. For any fixed combination of parameters C_0, C_g, C_1, C_2, R_1, R_2, V_1, V_2, V_g, q_b, and T, using Eq. (2) and (3), we can solve Eqs. (5) for the statistical distribution $p(n)$. We can then calculate the current I from Eq. (4) as a function of these parameters.

PERIODIC MODULATION OF THE CURRENT

Consider the one-to-one mapping $\{V_1, V_2\} \leftrightarrow \{v, V\}$:

$$V_1=V-v, \quad V_2=-v, \tag{6}$$

so that $V_1-V_2=V$ always. In experiment this means that the voltages V_1 and V_2 are generated (according to Eq. (6)) by an operational amplifier or computer starting from

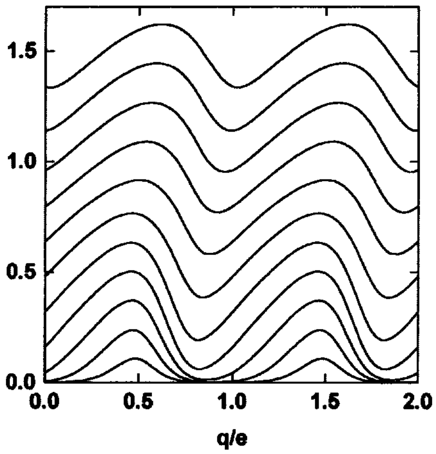

FIG. 2. Single-electron transistor effect. Current I, defined by Eq. (4), versus the partial polarization q, defined by Eq. (8), at different transport voltages VC/e in increments of 0.2, starting from 0.2 at the bottom. $k_BT = 0.05\, e/C$, $C_1 = 0.7\, C$, $C_2 = 0.1\, C$, $R_2/R_1 = 10$, $R = R_1 + R_2$.

two independently controlled parameters: V and v. By changing v independently of V and other parameters of the system, we hope to reproduce the TE when the gate is absent completely $(C_g = 0)$.

After applying transformation (6) to Eq. (2), we get:

$$F^{\pm}_{1,2}(n) = \pm(e/C)(\pm e/2 + K_{1,2}V + en + q), \tag{7}$$

with $K_1 = -(C_0 + C_g + C_2)$, $K_2 = C_1$, and partial polarization

$$q = q_b + C_gV_g + (C_0 + C_g)v, \tag{8}$$

recall that the four expressions $F^{\pm}_{1,2}(n)$ determine the probabilities $p(n)$, current I, and all other measurable values.

An essential feature of Eq. (7) is that both q and n enter all four forms $F^{\pm}_{1,2}(n)$ in exactly the same combination $en + q$. As long as all other parameters of the system are kept constant, the simultaneous substitutions

$$\{q \to q + e, \;\; n \to n - 1\} \tag{9}$$

leave the combination $en + q$ invariant. So the whole set of $[F^{\pm}_{1,2}(n)$, $\Gamma^{\pm}_{1,2}(n)$, and $p(n)]$ for all n is covariant with the shift (9). From Eq. (4) we see that the current I remains invariant under the change (9). And this just means that the current is periodic (Fig. 2) in q with a period

$$q_{\text{period}} = e. \tag{10}$$

Note that K_1 and K_2 in Eq. (7) are always different. They even have different sign. Therefore, there can be no periodicity in V.

In traditional (3-terminal) experiments a monotonic change of q is achieved through a change of the gate voltage V_g. The resulting current modulation with a period

$$V_{g\ \mathrm{period}} = e/C_g \tag{11}$$

is known as the single-electron TE.

Alternatively, the same effect can be obtained if the parameter v is changed with all the other parameters held constant. From Eqs. (8) and (10) we see that in this case current is modulated with a period

$$v_{\mathrm{period}} = e/(C_0 + C_g). \tag{12}$$

If both parameters V_g and v are changed simultaneously, the current is modulated with the period (10).

TWO-TERMINAL DEVICE

From Eqs. (7) and (8) it is clear that the pairs $\{C_g, V_g\}$ and $\{C_0 + C_g, v\}$ play similar roles in SET dynamics. This means that if the system under study lacks a gate C_g completely $(C_g = 0)$, one can still study the TE experimentally, but now with the parameter C_0 as the effective gate, the parameter v as the effective gate voltage, and the modulation period v_{period} given by Eq. (12).

It can often happen that an interesting two-terminal double-barrier structure[1] is fabricated in a way which precludes placing a nearby gate with a sufficiently large C_g. Indeed, in demonstrating periodic modulation of the tunnel current one usually needs to restrict the voltages to the range $V_g < 1$ V, just to preserve the mechanical and electrical stability of the systems under study. Larger voltages may cause redistribution of the surrounding charged contaminants (changing the background charge q_b) and trigger processes such as electromigration. To have $V_{g\ \mathrm{period}} < 1$ V, we need $C_g > 0.1$ aF. This is hard to achieve for a central island of small dimensions. If a central island has a radius $r \simeq 1$ nm, as in Refs. 1 and 2, and a gate is separated from it by a distance d, then the gate capacitance can be estimated as $C_g \simeq \varepsilon_{\mathrm{eff}} \varepsilon_0 \pi r^2 / d$. To get $C_g < 0.1$ aF, the separation should be $d > 2$ nm (with $\varepsilon_{\mathrm{eff}} = 10$). It is very hard to make or find that narrow a separation which is not short-circuited and is not a tunnel junction. Recall that the typical thickness of a tunnel barrier is about 1 nm.

This challenging goal was achieved in Ref. 2 by a complicated and unpredictable method of gate fabrication. The authors began with lithographic deposition of a gold gate having a highly branched form. The gate was isolated from the conducting substrate. Then they covered the structure with a Langmuir film, containing conducting cluster molecules with radius $r \simeq 1$ nm. Some (very few) of the clusters happened to lie on the substrate within a distance $d > 2$ nm from the gate. Such clusters were sought out with a scanning tunneling microscope and were then used as the central island of a SET (substrate–cluster–microscope tip). This SET was successfully modulated by the gate at room temperature. An estimate according to Eq. (11) gave $C_g = 0.2$ aF.

The self-capacitance of a central island with radius $r = 1$ nm can be estimated as $C_0 \simeq \varepsilon_{\mathrm{eff}} \varepsilon_0 r \simeq 0.1$ aF. And Eq. (12) gives $v_{\mathrm{period}} \simeq 1$ V. In real systems the current leads can screen off some of the environment from the central island, thus reducing C_0 and increasing v_{period}. However, estimates made for known practical setups always gave a reduction of C_0 by a factor of less than 10. Thus from Eq. (12) we can expect a value $v_{\mathrm{period}} \simeq 0.3$ V for the same structure. This means that the authors of Ref. 2 might have demonstrated v modulation with a period (12) at the same room temperature, even without fabricating a complicated gate or searching for a cluster molecule which had accidentally stuck at an appropriate position.

Consider a SET with a quantum dot as the central island.[1] Due to spatial quantization of the wave function of an electron confined on the central island, the total capacitance C is no longer constant but depends on the charge ne, voltages, temperature, and the bulk and surface properties of the environment.[6] But even with variable C, the energy cost of tunneling depends on the polarization of the central island, and this polarization can be achieved by changing the voltage v in a two-terminal device. Thus charge quantization in a quantum-dot SET can be controlled by this effective gate.

Other mechanisms of electron transport (like co-tunneling[7] or thermal activation above the trapping barrier[8]) may contribute to the current. In either case the current is periodically modulated with respect to the polarization of the central island, which in turn can be achieved by changing either V_g or v.

A similar method can be used to control current through charge-quantized chains of tunnel junctions, in particular, through self-selecting chains of granules in disordered systems.[9]

Helpful discussions with F. Ahlers, Y. Nakamura, S. Oda, E. Soldatov, and A. Zorin are gratefully acknowledged. This work was supported in part by the Russian Fund for Fundamental Research and the Russian Program for Future Nanoelectronic Devices.

[a]e-mail: svysh@rsfq.npi.msu.su

---

[1] C. T. Black, D. C. Ralph, and M. Tinkham, Phys. Rev. Lett. **76**, 688 (1996).
[2] E. S. Soldatov, V. V. Khanin, A. S. Trifonov *et al.*, JETP Lett. **64**, 557 (1996).
[3] D. V. Averin and K. K. Likharev, in *Mesoscopic Phenomena in Solids*, Eds. B. L. Altshuler, P. A. Lee, and R. A. Webb, Amsterdam: Elsevier, 1991.
[4] L. D. Landau and E. M. Lifshitz, *Electrodynamics of Continuous Media*, Oxford: Pergamon Press, 1960.
[5] G.-L. Ingold and Yu. V. Nazarov, in *Single Charge Tunneling*, Eds. H. Grabert and M. Devoret, New York: Plenum, 1992 (NATO ASI Series B, Vol. 294).
[6] K. Natori, J. Appl. Phys. **78**, 4543 (1996).
[7] D. V. Averin and Yu. V. Nazarov, *op cit.* 5.
[8] S. V. Vyshenski, JETP Lett. **64**, 592 (1996).
[9] S. V. Vyshenski, JETP Lett. **61**, 111 (1995).

Published in English in the original Russian journal. Edited by Steve Torstveit.

ERRATA

Erratum: Semiclassical theory of the Coulomb anomaly [JETP Lett. 66, No. 3, 214–221 (10 August 1997)]

S. Levitov and A. V. Shytov

Massachusetts Institute of Technology, Cambridge, MA 02139, USA; L. D. Landau Institute of Theoretical Physics Russian Academy of Sciences, 117334 Moscow, Russia

[S0021-3640(97)01319-4]

PACS numbers: 73.23.Hk, 73.40.Gk, 72.15.Qm, 99.10.+g

The first author's name should be as follows: ''L. S. Levitov.''